Design and Assembly Considerations in the Engineering of Vascular Tissue

(Article begins on next page)

HARVARD UNIVERSITY
Graduate School of Arts and Sciences

DISSERTATION ACCEPTANCE CERTIFICATE

The undersigned, appointed by the

School of Engineering and Applied Sciences

have examined a dissertation entitled:

"Design and Assembly Considerations in the Engineering of Vascular Tissue"

presented by : Jin Cheng Ye

candidate for the degree of Doctor of Philosophy and here by certify that it is worthy of acceptance.

Signature _____

Typed name: Prof. K. Parker

Signature _____

Typed name: Prof. D. Mooney

Signature _____

Typed name: Prof. D. Needleman

Date: December 17, 2013

Page intentionally left blank.

Design and Assembly Considerations in the Engineering of Vascular Tissue

A dissertation presented

by

Jin Cheng Ye

to

The School of Engineering and Applied Sciences

in partial fulfillment of the requirements
for the degree of

Doctor of Philosophy

in the subject of

Engineering Sciences

Harvard University
Cambridge, Massachusetts

December, 2013

Dissertation Advisor: Professor Kevin Kit Parker   Author: Jin Cheng Ye

Design and Assembly Considerations in the Engineering of Vascular Tissue

Abstract

Native vascular tissue functions are highly dependent on structural organization at the super-cellular, cellular, and sub-cellular spatial scales. We hypothesized that the structure-function relationship of vascular tissues *in vivo* can be leveraged to engineer vascular tissues *in vitro* by prescribing the shape of constituent cells and their assembly into organized three-dimensional structures. To this end, we first asked if vascular smooth muscle cell shape influences cellular contractility. We engineered human vascular smooth muscle cells to assume similar shapes to those in elastic and muscular arteries and then measured their contraction while stimulating with endothelin-1. We found that vascular smooth muscle cells with elongated shapes exhibited lower contractile strength but a greater percentage increase in contraction after endothelin-1 stimulation, suggesting that elongated vascular smooth muscle cell shape endows the muscular artery with greater dynamic contractile range. Next, we sought to assemble cells into tissues by employing a three-dimensional cellular patterning strategy based on the folding of porous, thin polymer films. We assembled different three-dimensional endothelial and vascular smooth muscle organizations by patterning two-dimensional poly(lactic-co-glycolic) acid and collagen thin films with cell suspensions at prescribed locations. The films were subsequently folded following Miura-ori geometry guidelines and the matrices were embedded subcutaneously in immunodeficient mice in order to assess the vascularization of the implanted constructs. We found that spatial organization

that allowed endothelial and vascular smooth muscle cells to interact adjacent to each other laterally in the same folding plane created the densest vascularized network, suggesting that three-dimensional structural organization of vascular cells can influence the formation of vascularized networks. Taken together, our result shows that functional vascular tissues *in vitro* can be engineered by encoding structure cues in their design and assembly.

Table of Contents

Table of Figures

Acknowledgments

I would like to thank my advisor, Prof. Kevin Kit Parker for his guidance, patience, inspiration and support throughout one of the most stressful periods during my PhD career. Although I only had the opportunity to closely interact with him for little over a year after joining the Disease Biophysics Group in September 2012, his rigorous, innovative and collaborative approach for scientific research had led to a very meaningful and productive final year of my graduate study at Harvard University. Not only have I learned how to become an independent and mature scientist under his mentorship, but also I gained a profound understanding in what it means to be a leader, in scientific research and life in general. I am certain that this will benefit me for the many years to come in my personal and professional development and I am deeply grateful for his teachings.

I am also grateful to my dissertation committee for their help, advice and time. Their subject expertise made their constructive comments and feedback in every meeting exceptionally helpful at times when I needed them the most. I would like to thank Prof. David Mooney for his valuable time and insightful advice throughout my PhD. I also would like to thank Prof. Daniel Needleman for his helpful discussion and comments at critical points of the project. I also greatly appreciate for their understanding, empathy and support for me during the final period of my PhD, for I would not have succeeded without them.

I would also like to thank all members of the Disease Biophysics Group for they have not only taught me much about scientific research, but also supported me emotionally as friends through the ups and downs I experienced during my PhD. In

particular, I would like to express my most sincere gratitude to Dr. Yvonne Aratyn-Schaus, Mr. Alexander P. Nesmith, and Dr. Megan McCain for teaching me and helping me troubleshooting the traction force microscopy assays. I also would like to thank Mr. Borna Dabiri and Dr. Leila Deravi for their helpful feedback on my presentations and writings. Their encouragement and support are essential for the completion of my PhD and I am touched by their kindness.

I also would like to thank my beloved parents for believing in me and supporting me for my pursuit of higher education in the United States. I owe much of my accomplishments today to their sacrifices in immigrating to Canada, where they hoped that it may provide a brighter future for me. Their unconditional love for me served as one of the greatest strengths in me and it is never enough to express my gratitude to them.

I thank all the faculty members, staff and my fellow graduate students and colleagues for their help and friendship during my journey here at Harvard University. I like to thank Dean Cherry Murray for her kindness and support during the difficult lab transition period. I thank Prof. Debra Auguste for her mentoring during the first four years of my PhD career. I also really appreciate all the administrative help I received from Mr. David Boyle, Ms. Katie Parodi, and Ms. Jessa Piaia. I thank all my former lab mates from the Auguste lab including Dr. Marjan Rafat, Prof. Jin-Oh You, Ms.Dariela Almeda, Ms. Renita Horton, Mr. Kyle Satterstrom, and Dr. Rico Gunawan. Their positive attitude have inspired and motivated me to become a better person.

Lastly, I am grateful for the financial support from the School of Engineering and Applied Sciences, Natural Sciences and Engineering Research Council of Canada and the Wyss Institute for Biologically Inspired Engineering at Harvard University.

1   Introduction

Engineering functional vascular smooth muscles *in vitro* remains challenging because of the complexity of recapitulating structural organization across multiple spatial scales. Early efforts primarily focused on controlling vascular smooth muscle functions by biochemical signaling; however, accumulating evidence suggests that mechanotransduction, the process by which cells convert mechanical stimuli in the cellular microenvironment into biochemical cues, holds promise as a novel approach to engineering this tissue. Here, we discuss an engineering strategy that recapitulates mechanotransduction to build functional vascular smooth muscles *in vitro*. By harnessing mechanical cues in the cellular microenvironment, functional vascular smooth muscles can be engineered with cytoskeletal architecture. A number of vascular smooth muscle functions that depend on the cytoskeletal architecture could then be evaluated through performance metrics to assess if desired functional outcome is achieved. Engineering functional vascular smooth muscle *in vitro* may yield new insight on the development of vascular grafts and accelerate drug discovery research for treating cardiovascular diseases.

1.1   Mechanotransduction as a Strategy for Engineering Functional Vascular Smooth Muscle

Engineering functional vascular tissue *in vitro* is not a trivial pursuit due to the dependency of vascular functions on the three-dimensional structural hierarchy that spans several orders of spatial magnitude ranging from centimeter length scale of the arteries to the nanometer length scale of cytoskeletal proteins (Figure 1-1). For example in a healthy arterial tissue, endothelial cells (ECs) line the inner most layer of the blood vessel to

1

protect the vascular smooth muscles (VSM) from blood shearing force. In turn, the VSM

provides structural support to the ECs by wrapping around the ECs in helices to

Engineering functional vascular smooth muscles (VSMs) *in vitro* remains challenging

because VSM structure and function interact over several orders of spatial magnitude,

ranging from the centimeter-length scale of arteries to the nanometer-length scale of

cytoskeletal proteins (Figure 1). VSM structure and function are maintained *in vivo* in

several ways, one of which is the regulation of mechanical forces at the tissue, cellular,

and sub-cellular spatial scales through a process called mechanotransduction, in which

cells translate mechanical stimuli into biochemical reactions. In the native environment,

cyclic cardiac cycles expose VSM to mechanical stimuli from a number of sources, such

as transmural pressure, vascular strain induced by pulsatile pressure, and circumferential

and axial wall tension [1]. VSM, in turn, responds by inducing changes in cytoskeletal

organization [2-4], membrane ionic conductance [5-7], and signaling activation [8-11],

that lead to functional changes in VSM contraction, secretion, growth, and migration. A

well-studied example of this process is the myogenic response, where small arteries

contract to counteract increased intraluminal pressure, protecting the blood vessel from

potential hypertensive injury [12]. Thus, mechanotransduction enables VSM to respond

to mechanical stimuli encoded in the local microenvironment and remodel its function to

serve the needs of the blood vessel.
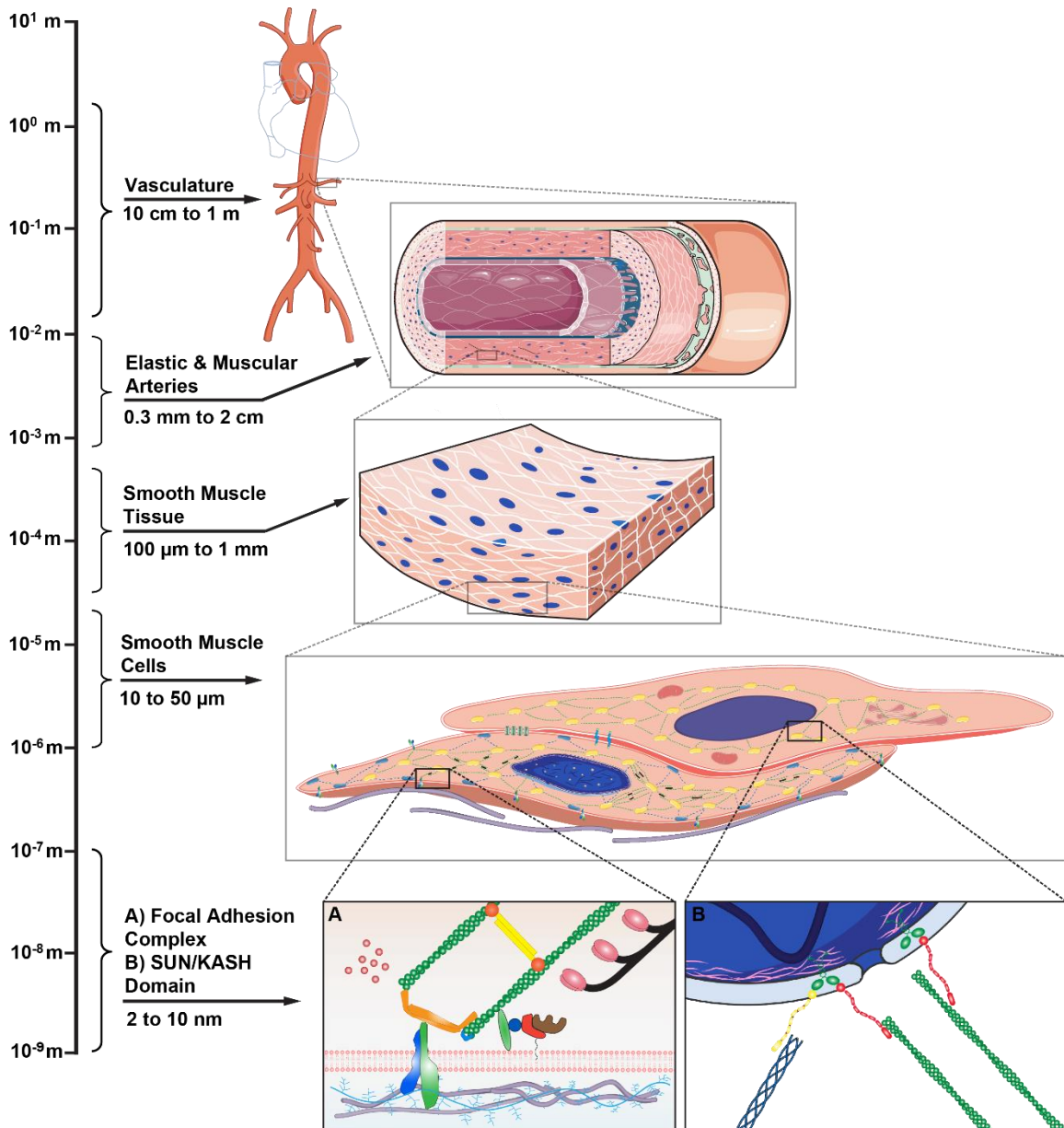
Figure 1-1: Hierarchical organization of vascular tissue spans multiple spatial scales from nanometers to meters. Vascular smooth muscle cells assemble into muscle tissue that forms the media layer of the elastic and muscular arteries. The spindle shaped cells contains nanometer scaled protein complexes that allow it to respond to mechanical cues in the cellular microenvironment. Adapter in part from Servier Medical Art.

Differentiated, healthy VSM typically operate in sustained constriction, or tone, to regulate peripheral resistance, thereby maintaining systemic blood pressure and controlling organ blood flow. Disruption of tone can produce vascular disorders such as hypertension [13] and vasospasm [14], where VSM contraction deviates from its homeostatic equilibrium. Such conditions are commonly treated by pharmacological manipulation of VSM contractile signaling to modulate its tone. Traditional drugs that target the VSM contractile pathway include alpha- and beta-adrenergic receptor antagonists, calcium channel blockers, angiotensin converting enzyme (ACE) inhibitors, and angiotensin II receptor antagonists [15]. Drug development efforts now seek to identify compounds that either activate or inhibit VSM cell (VSMC) large conductance Ca^{2+} activated K^+ (BK_{Ca}) channels to regulate the membrane potential of VSM and, in turn, control the vascular tone [16]. The efficacy of these drugs on VSM tone can only be validated *in vitro* if a VSM model functionally recapitulates its *in vivo* counterpart.

In this review, we discuss how an engineering algorithm based on recapitulating the native mechanotransduction processes can be applied to design, build, and test a functional VSM *in vitro* model. We first demonstrate that cytoskeletal proteins in the extracellular, intercellular, and intracellular domains are mechanotransductive components responsible for regulating VSMC architecture and functions. We then describe the mechanical cues that can be used to design the assembly of these cytoskeletal proteins into VSM with engineered cellular architecture. Finally, we present a performance evaluation metric comprising functions that could be influenced by the engineered cellular architecture.

4

1.2   Cytoskeleton Components in Vascular Smooth Muscle Cell

Mechanotransduction

VSMCs sense a wide array of mechanical stimuli through a network of cytoskeletal proteins embedded in the extracellular, intercellular, and intracellular domains. These dynamic proteins continuously sense changes in the cellular microenvironment and remodel their organization to drive the force balance towards equilibrium (Figure 1-2). For example, integrin proteins are directly connected to actin filaments, allowing forces to be transmitted from outside to inside the cells [17]. Cadherin junctions directly couple adjacent VSMCs together and propagate mechanical signals from one cell to the next [18]. Actin, intermediate filaments, and microtubules propagate mechanical signals through common hubs at dense plaques throughout the VSMC cytoplasm [19]. Thus, the cytoskeletal proteins provide design parameters that we can engineer to recapitulate the mechanotransduction processes in VSMC.
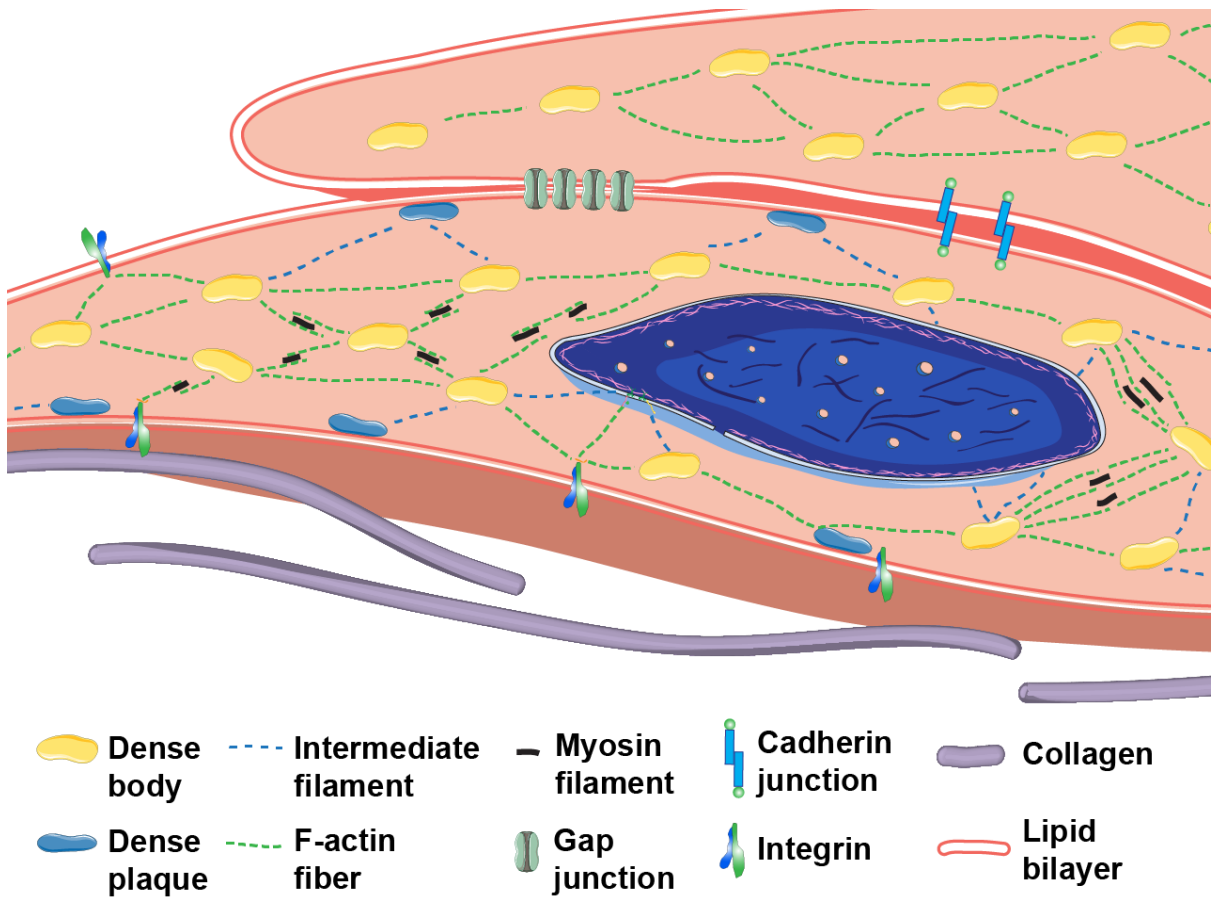
Figure 1-2: Mechanotransductive cytoskeletal proteins in vascular smooth muscle cells. Integrin links the ECM protein such as collagen to actin fibers, allowing extracellular mechanical signals to be directly transmitted into the cell. Actin responds to mechanical input to the cells by rapid by changing the F- to G-actin ratios and acts as an intracellular sensor. Cadherin junctions provide mechanical links between adjacent cells, allowing forces to be transmitted between cells.

1.2.1 Mechanical Signaling through Integrin-ECM Interface

Integrin proteins are transmembrane, heterodimeric receptors comprising α- and β-subunits. They connect the extracellular matrix (ECM) to the internal cytoskeletons at the site of focal adhesion complex *via* the short cytoplasmic tail of the β-subunit (Figure 1-3). Furthermore, integrins transduce both "outside-in" and "inside-out" mechanical signals in many different cell types. Twenty-four integrins have been described and among them, $\alpha_1\beta_1$, $\alpha_2\beta_1$, $\alpha_3\beta_1$, $\alpha_4\beta_1$, $\alpha_5\beta_1$, $\alpha_6\beta_1$, $\alpha_7\beta_1$, $\alpha_8\beta_1$, $\alpha_9\beta_1$, $\alpha_v\beta_1$, $\alpha_v\beta_3$, $\alpha_v\beta_5$, and $\alpha_6\beta_v$ are found in VSMCs [20, 21].
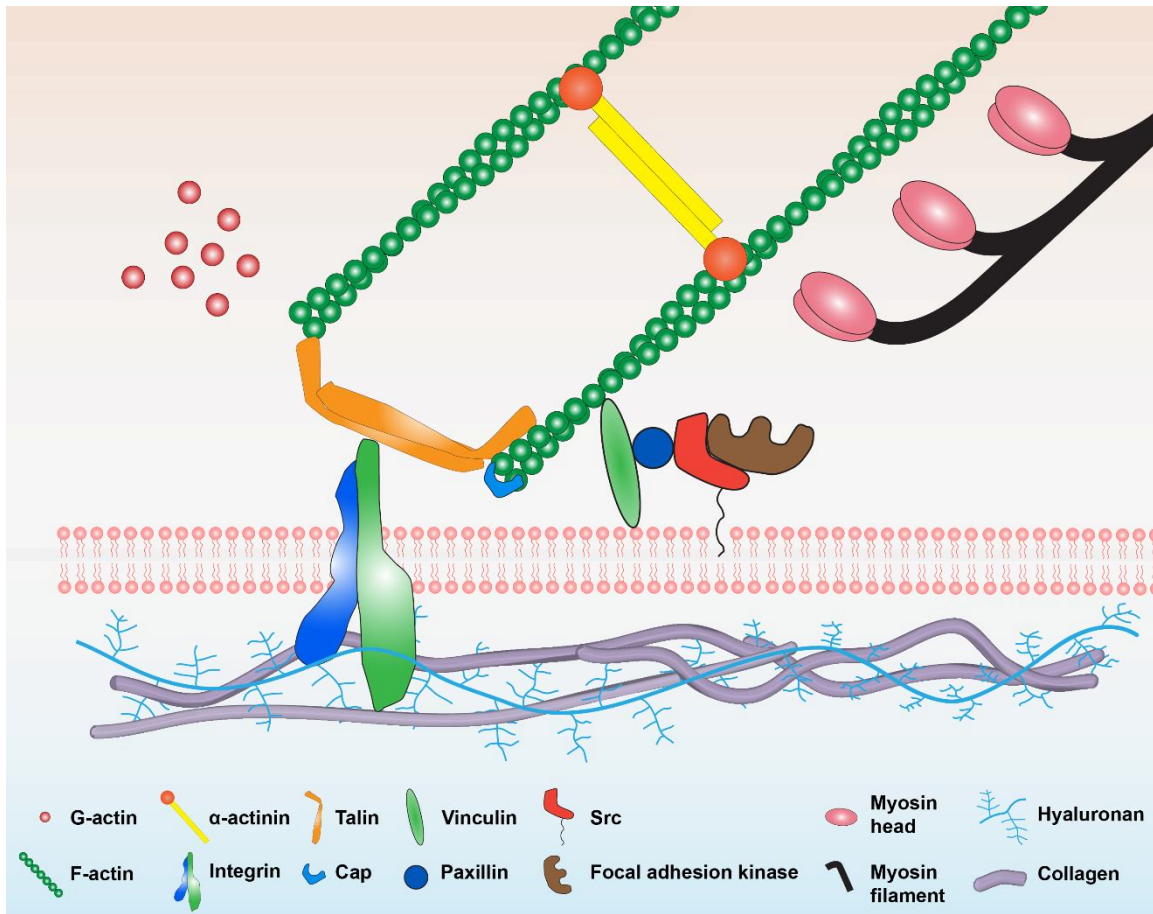
Figure 1-3: Mechanotransductive proteins in the focal adhesion complex.

Transmembrane protein integrin physically links extracellular matrix protein such as collagen in the extracellular domain to intracellular structure protein such as F-actin. This allows mechanical inputs to be transmitted in both ways, allowing "outside-in" and "inside-out" signaling. Cellular components are not to scale.

In vitro studies using isolated arterioles and VSMCs have provided strong evidence that some integrins are crucial mechanotransductive elements for VSMCs. Wilson and colleagues demonstrated that soluble fibronectin, integrin binding peptide GRGDTP, and antibodies to β_3 or $\alpha_v\beta_5$ all independently block the mitogenic response of newborn rat VSMCs to mechanical strain [22]. Other studies subsequently showed that

an integrin-recognizing synthetic RGD peptide can cause sustained vasodilation [23] and decreased intracellular Ca^{2+} level in rat VSMCs [24]. These early studies demonstrated that integrins play an important role in transducing mechanical cues to intracellular signals that produce functional adaptive responses. More recently, studies on isolated rat arteriole tissue and VSMCs showed that antibody blocking of $\alpha_5\beta_1$ and $\alpha_v\beta_3$ integrins significantly inhibits myogenic constriction [25, 26]. However, pulling on fibronectin and β_1-integrin antibody-coated magnetic beads on isolated renal VSMCs elicits an increased cell force and sustained traction, autologous to pressure-induced myogenic response [27]. The integrin mechanotransduction mechanism has also been linked to BK_{Ca} ion channel activities and *Src*-dependent pathways [28, 29]. Collectively, these studies demonstrated that integrins are critical to mechanotransduction and adaptive remodeling in VSM tissue and cells.

1.2.2   Mechanical Signaling through Intercellular Junctions

In addition to cell-ECM connections, VSMCs in the vascular wall contain a variety of cell-cell adherent junctions, including cadherin and gap junctions [30]. The cadherin family of calcium-dependent transmembrane receptors is mechanically important: they bind together adjacent VSMCs and link them intracellularly to actin filaments *via* catenins, allowing direct force transmission between neighboring cells [31-33].

VSMCs express multiple cadherins, including N-cadherin, T-cadherin, R-cadherin, cadherin-6b, and E-cadherin (in the case of atherosclerotic lesions) [21]. The predominant cadherin, N-cadherin, is expressed at a higher level in human venous

smooth muscle cells (SMCs) than in arterial SMCs [34]. While N-cadherin has been

investigated in the context of VSMC migration [35], proliferation [36], and survival [37],

Jackson et al. showed that selective blockage of N-cadherin or a cadherin inhibitory

peptide in rat cremaster arterioles inhibits myogenic response to pressure changes

independent of $[Ca^{2+}]_i$ [38], implicating N-cadherin in mechanical load sensing and

arteriolar contraction regulation. T-cadherin was originally identified in a membrane

fraction of aortic SMCs [39]. Unlike classical cadherin family members, T-cadherin does

not have transmembrane and cytosolic domains but instead is anchored to membranes by

means of glycosylphosphatidylinositol (GPI). An analysis of Triton-X fractionized

human and rat VSMCs revealed that T-cadherin co-localizes with mechanotransducing

signaling molecules such as Gαs protein and *Src*-family kinases in caveolin-rich

membrane domains [18], suggesting that T-cadherin may function as a local signal-

transducing protein as well as an adhesion molecule. Additional studies on the exact

mechanism of cadherin-based mechanosensing are needed to understand its role in the

regulation of VSMC cytoskeletal structure and contractile responses.

1.2.3   Intracellular Signaling Mechanics

Actin is the most abundant cytoskeletal protein in contractile VSMCs,

contributing ~20% of total protein content [40]. Four of the six vertebrate isoforms of

actin are found in VSMCs: α-smooth muscle actin (SMA), β-non-muscle actin, γ-SMA,

and γ-cytoplasmic actin. Large arteries typically contain about 60% α-SMA, 20% β-non-

muscle actin, and about 20% combined γ smooth muscle and γ non-muscle actin [41].

Both α- and γ-SMA are commonly referred to as contractile actin because of their

association with myosin filaments in generating tension and cell shortening. The two remaining actin isoforms are referred to as cytoplasmic actin and are localized to the cell cortex [42].

Although the precise role of cytoplasmic actin in arteriolar myogenic behavior remains uncertain, growing evidence supports the hypothesis that this subpopulation of actin contributes to VSMC mechanotransduction [2]. Earlier studies using pharmacological agents demonstrated that a short exposure period to actin depolymerizing agent profoundly suppresses VSM tension development [43-46], while exposure to actin stabilizer enhances myogenic tone [47], highlighting the critical role of actin polymerization in VSMC contraction and tension development. Independent studies using different techniques have demonstrated that actin polymerization is attributed to a small portion of G- to F-actin transition [47-50] that is associated with a redistribution of actin from the cell periphery (cortical region) to the cell interior [49]. More recently, Kim and colleagues, using labeled G-actin monomers, directly observed actin incorporation into cortical filaments upon agonist treatment [51] and that the non-muscle cytoplasmic actin is primarily responsible for the agonist-induced actin polymerization [40]. Given the known link between F-actin and putative mechanotransductive components such as integrins [52], cadherins [53], and ion channels [54], these results suggest that the cortical non-muscle actin isoforms compose a dynamic subpopulation of actin that allows it to function as an intracellular sensor that actively remodels its polymerization state in response to the level of mechanical force applied to the cells.

Intermediate filaments form bundles and associate with dense bodies to provide three-dimensional integrity to VSMCs [55]. Two intermediate proteins are found in

11

VSMCs, vimentin and desmin [55]. Vimentin production is high in VSMCs of large arteries. In human arteries, vimentin localization decreases gradually from proximal to distal, while desmin localization gradually increases [56-58]. Vimentin- [59] and desmin-deficient mice [60] with normal myogenic responses display alterations in vasomotor properties such as agonist sensitivity and impaired flow-dependent dilation, suggesting that vimentin and desmin may be required for sensing mechanical cues in the local microenvironment. A similar dependence on vimentin occurs in airway SMCs. Wang and colleagues reported that down-regulation of vimentin in canine airway smooth muscle attenuates force generation [61], while Tang et al. showed that airway smooth muscle stimulated with contractile agent 5-HT undergoes spatial rearrangement [62, 63]. Collectively, these results suggest that intermediate filaments of vascular and airway SMCs are important for adaptive remodeling to mechanical cues.

Microtubules provide resistive forces in many cell types and are considered the compression bearing elements [64]. Since the ability to adequately stain and detect polymerized microtubules in dense contractile tissue depends on the tissue type and staining method [65], contradicting findings on the role of microtubules in mechanotransduction have been reported for VSMCs. For example, one study showed that depolymerization of microtubules causes an elevated level of myogenic constriction in rat skeletal muscle arterioles when pressurized intravascularly. Furthermore, this response involves Rho-A dependent Ca^{2+} sensitization without an overt increase in $[Ca^{2+}_i]$ [66], suggesting that regulation of microtubule dynamics may be directly linked with VSMC contraction and reactivity. However, a higher level of isometric force is associated with an increased level of intracellular calcium in porcine coronary VSMCs

when treated with microtubule depolymerizing agent [67], suggesting that microtubules may not directly contribute to VSMC mechanical characteristics but rely on modulation of Ca^{2+} signal transduction. While the difference may be caused by the origin and species of the VSMCs, further studies are needed to determine the role of microtubules in VSMC mechanotransduction.

1.2.4   Zyxin and Nucleus as Mechanosensors

Focal adhesion associated protein and the nucleus also participate in VSMC mechanotransduction. For example, zyxin, a zinc-finger protein predominated located in the focal adhesions and stress fibers, dissociates from focal adhesions, translocates into the nucleus, and mediates expression of mechanosensitive genes within minutes of cyclic stretching in rat aortic SMCs [10]. Although the mechanistic interactions between zyxin and mechanosensitive genes remain to be elucidated, these results suggest that zyxin functions as a mechanosensor. The nucleus was recently found to interact directly with the cytoskeleton *via* nuclear membrane proteins such as the SUN/KASH domain proteins [68-70] (Figure 1-4). This physical linkage allows mechanical forces exerted on the surface adhesion receptors to be transmitted along the cytoskeletons to the protein complexes in the cytoplasm and nucleus [71]. By studying the contractile filament organization in airway SMCs using electron microscopy, Kuo et al. revealed that contractile filaments for airway SMCs are arranged parallel to the longitudinal axis and centrally attached to the nuclear envelope, effectively making the nucleus a force-transmitting structure [72]. Similar findings were observed by Nagayama and colleagues in aortic SMCs: stress fiber stabilizes the position of intranuclear chromatin through

mechanical connection with the nucleus [73], which modulates gene and protein expression in VSMCs and alters functional behavior. Taken together, these studies provide strong evidence that zyxin and the nucleus also play a role in VSMC mechanotransduction.
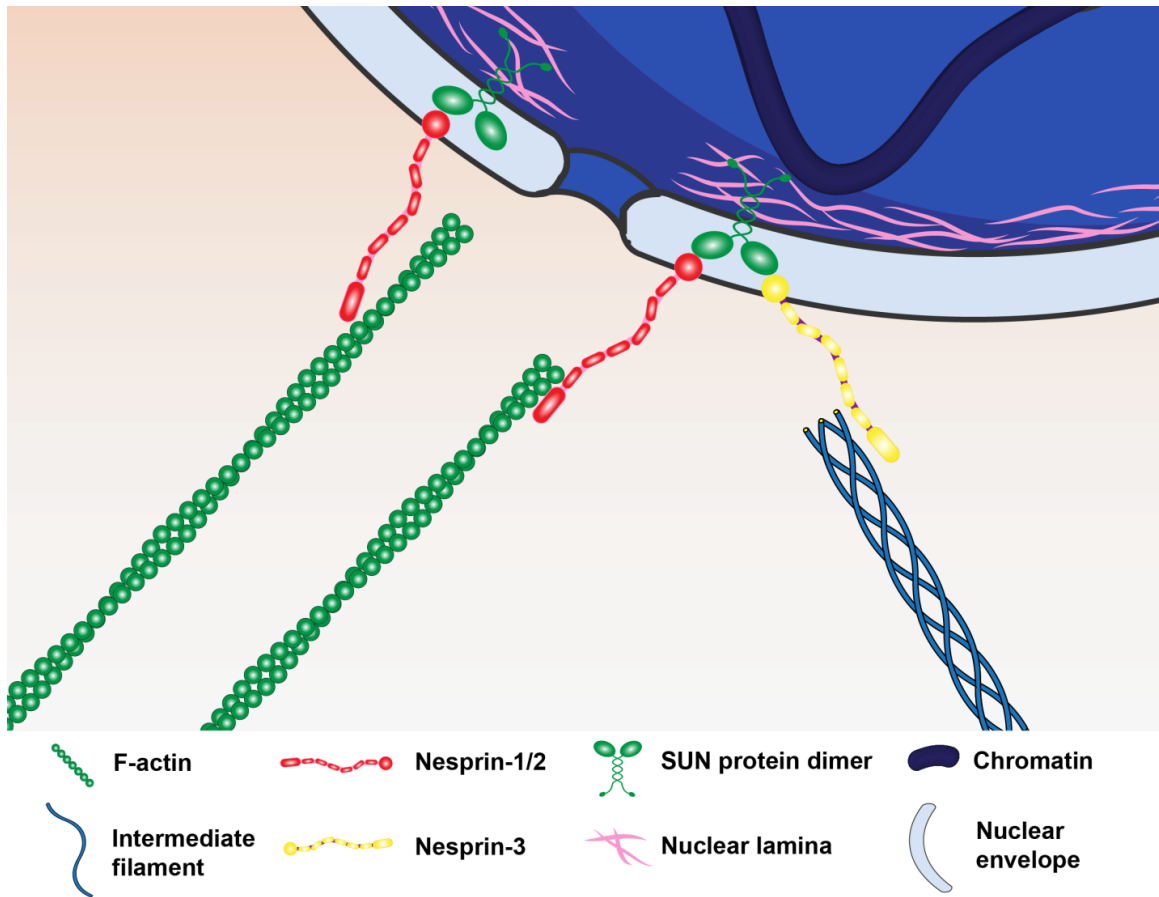
Figure 1-4: Force transmissions via cytoskeleton to the nucleus. F-actin stress fibers and intermediate filaments are connected to the SUN protein dimers via the Nesprin-1/2 and Nesprin-3 protein complexes. The SUN proteins bind to nuclear lamina and other nuclear envelope proteins, which are connected to DNA and chromatin inside the nucleus. These proteins together couple the cytoskeleton mechanically to the nucleus, allowing mechanical signal to directly influence chromatin remodeling.

In summary, the extracellular, intercellular, and intracellular components of the VSMC cytoskeleton are embedded with proteins and filaments that are able to detect mechanical stimuli from the ECM, adjacent cells, or within the cytoplasm. Sensing these stimuli allows the cell to activate signaling pathways that promote structural remodeling of its cytoskeleton to offset or adapt to mechanical loading. These mechanotransductive cytoskeletal components serve as the design components that enabled us to build VSMC with engineered cytoskeletal architecture with desired functions.

1.3   Engineering Vascular Smooth Muscle Form with Mechanical Cues

VSMCs in their native environment experience a variety of mechanical stimuli such as cyclic stretching, cell shape deformations, ECM interactions, substrate stiffness, and surface topography at micro- and nanoscale. Due to the mechanotransductive nature of the cytoskeletal proteins, mechanical stimuli can regulate both cytoskeletal architecture and cellular function and cytoskeletal proteins are tightly regulated spatiotemporally to ensure proper VSMC structure and function in normal physiological settings. When stimuli deviate from the normal range, maladaptive remodeling occurs in the cytoskeletal architecture and leads to diseased function in VSMCs. For example, in the case of vascular aging, wear and tear from cardiac cycling causes fatigue and fracture in the elastic fibers, promoting degeneration of the media layer and vessel stiffening [74]. These changes in the ECM composition and substrate stiffness increase VSMC stiffness by increasing their adhesion molecule expression [75, 76] and drive the system away from healthy conditions and toward cardiovascular diseases.

15

Although maladaptive remodeling in the VSM native environment can cause undesirable outcomes *in vivo*, we can harness the contribution of mechanotransduction on VSMC form and function *in vitro* to our advantage by regulating the assembly of these cytoskeletal proteins to build VSM with engineered cellular architecture. In the following sections, we will review the influence of different mechanical cues on the VSMC cytoskeletal architecture.

1.3.1   Tensile Stress

The pulsatile nature of the vasculature exposes VSMCs to cyclic stretching in their native environment. Using ultrasonography and other methods, direct viewing of the vasculature *in vivo* demonstrated that each cardiac cycle can deform human arteries, arterioles, and veins between 6 and 22%, with more distention experienced by larger, proximal arteries [77-80]. These observations generated interest in the effect of stretching on VSMC behavior *in vitro*. Cyclic stretching on rat VSMCs *in vitro* produces rapid reorganization of stress fibers perpendicular to the stretching direction [4]. Longitudinal stretching of the vascular wall induces actin polymerization [81]. In addition, cyclic stretching in rat VSMCs leads to increased expression level of insoluble focal adhesion contact components [3], paxillin, and vinculin [82], suggesting that cyclic stretching may strengthen the number and size of focal adhesion complexes. These findings indicate that mechanical stimulation in the form of cyclic stretching can remodel the state and organization of actin stress fibers and focal adhesions, which may subsequently feed back to VSMC functional changes.

1.3.2   Cellular Boundary Condition

Recent advances in cellular engineering have enabled reproducible and precise studies on the role of cell shape in mechanotransduction [83-85]. Our group has utilized microcontact printing (μCP) to micropattern ECM proteins on substrate to create user-defined cell-adhesive patterns that produce cells with various shapes [86-89]. More recently, our group engineered VSM tissues of varying widths by constraining the line width of micropatterned fibronectin and lamina proteins [90]. We found that, while the alignment of F-actin stress fibers is similar, the nuclear eccentricities of constituent VSMCs significantly correlates with cell shape with length-to-width aspect ratios (ARs) between 20:1 and 50:1 [90]. To investigate the shape-contractility function more rigorously, we recently engineered single VSMCs on fibronectin islands with ARs from 5:1 to 20:1 and quantified their F-actin alignment by measuring the orientational order parameter (OOP) and nuclear eccentricity (Figure 5). In contrast to VSM tissues, we found that isolated VSMCs with higher ARs have increased OOP and nuclear eccentricity, suggesting elongated cell shape leads to more aligned stress fibers and elongated nuclei [91].
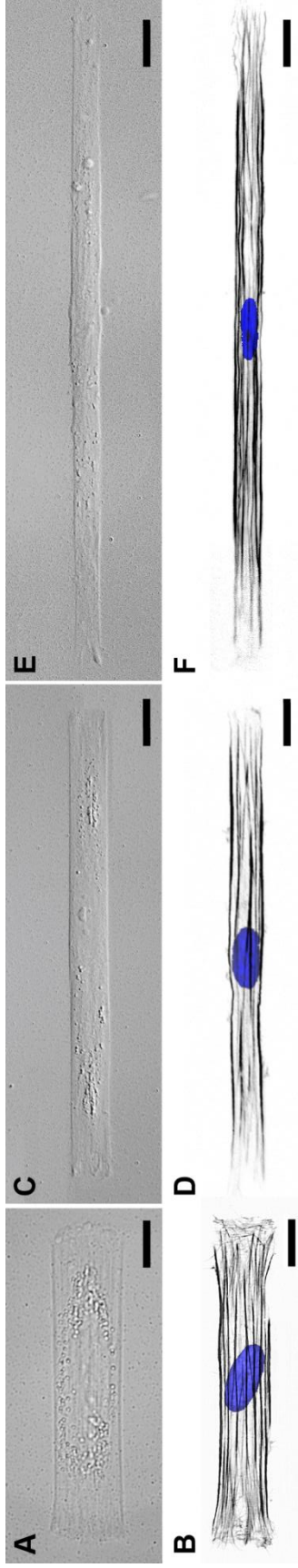
Figure 1-5: Cellular shape directs cytoskeletal architecture. Microfabricated vascular smooth muscle cells with length to width aspect ratios of 5:1 (A-B), 10:1 (C-D), and 20:1 (E-F) self-assemble their cytoskeleton based on the boundaries of the micropatterned fibronectin pattern. (A, C, F) are differential interference contrast images of microfabricated cells. (B, D, F) are stained for F-actin (black) and nuclei (blue). Actin fibers and nuclei became increasingly aligned with the principle axis as cellular aspect ratio increased. Projected nuclear area also decreased as cell became more elongated. The remodeling of cytoskeleton as a result of cell shape re-distributes its mechanotransductive components and can lead to different contractile functions during healthy and diseased environment. (A-F) scale bars = 20 μm.

18

The effect of two- and three-dimensional (3D) VSMC shape on cytoskeletal remodeling has also been described by several other groups. Thakar et al. showed that bovine VSMCs cultured on micropatterned collagen strips with elongated cell shape have decreased expression of actin stress fibers and α-actin on narrower strips [92]. They also reported that elongated cell shape lowers the nuclear shape index of isolated VSMCs while reduced spreading area significantly reduces nuclear volume [93]. When isolated rat VSMCs were cultured on user-defined cell adhesive patterns fabricated by plasma lithography, Goessl and colleagues observed cell shape-dependent actin formation and nuclear shape change [94]. When rat VSMC volume was changed in three dimensions (3D) through hyperosmotic shrinkage or hyposmotic swelling, a dramatic elevation of F-to G-actin ratio was observed [95], suggesting that actin polymerization occurs in response to cell shape changes in 3D. Thus, these reports demonstrated that cellular shape and cytoskeletal architecture direct the location and organization of mechanosensitive components including stress fibers and nucleus, suggesting one potential mechanistic pathway in which cell shape changes in two and three dimensions are translated to functional differences in VSMCs.

1.3.3   Extracellular Matrix Interactions

ECM components influence VSMC phenotype and functions like migration, proliferation, and contraction *in vitro*. Concomitantly, significant changes in cytoskeletal organization and expression have also been reported. One early study reported that isolated rat VSMCs cultured on laminin develop significantly fewer focal adhesions than cells cultured on fibronectin [96]. Another found different amounts of myofilament

expression in rabbit VSMCs cultured on interstitial matrix (collagen I and fibronectin), basal lamina protein (collagen IV and laminin), and the serum adhesion protein vitronectin [97]. In addition, immunofluorescent staining of stress fibers with antibodies against α-actin, myosin heavy chain isoform SM2, and vimentin, revealed that stress fiber expression of VSMC cultured on fibronectin coated substrate over a 5-day culture period gradually reduced with time [98], suggesting that ECM can mediate active remodeling of cytoskeleton. More recently, distinct morphologies of actin organization and focal adhesion formation were found on VSMCs cultured on different ECM components [99]. Specifically, for VSMCs cultured on fibronectin and collagen IV, cytoskeletal stress fibers organize along the long axis of the cell and tight bundles occur along the periphery; whereas this stress fiber organization is less typical for cells cultured on collagen I and laminin. In addition, rounded focal adhesions are induced by fibronectin, while elongated morphology is more common for collagens. Furthermore, a significant decrease in both F-actin and vinculin area occurs only for cells on fibronectin matrix. These studies demonstrated that ECM regulates the assembly and organization of cytoskeleton in VSMCs.

1.3.4   Substrate Stiffness

In a large number of cardiovascular diseases involving VSMCs, such as hypertension, hypertrophy, and atherosclerosis, the stiffness of the diseased blood vessels is dramatically altered [100]. Changes in substrate stiffness in two- and three-dimensional culture systems lead to VSMC cytoskeletal remodeling. Peyton and colleagues have shown that human VSMCs cultured on two-dimensional polyacrylamide gels with a

range of stiffness from 1.0 to 308 kPa display more visible F-actin bundles and punctate

focal adhesion sites on a rigid substrate compared to cells cultured on soft substrates

[101]. In the same study, they also demonstrated that an intermediate stiffness produces

an intermediate amount of fibers and focal adhesions. Extending those findings using a

poly(ethylene glycol)-conjugated fibrinogen based three-dimensional culture system with

compressive modulus between 448 and 5804 Pa, the group observed a higher level of F-

actin bundling on VSMCs on stiff matrices after 14 days in culture [102]. These results

suggest that VSMCs actively adapt to stiffness in the microenvironment by remodeling

stress fiber and focal adhesion organization.

1.3.5   Topography

A wide range of cell types respond to topographical cues such as grooves, ridge,

stops, pores, wells, and nodes in micro- and nano-scale [103-107]. VSMCs in their native

environment also interact with micro- and nano-scaled features such as pores, fibers, and

ridges on the basement membrane [108]. Studies that mimick these micro- and nano-

scale topographies *in vitro* have reported active remodeling of cellular cytoskeleton.

VSMCs seeded on nanopatterned gratings of poly(methyl methacrylate) (PMMA) and

poly(dimethylsiloxane) (PDMS) assume elongated cell and nuclei shapes [109]. VSMCs

cultured in micro-channels with channel widths of 20, 30, 40, 50, and 60 μm display

highly aligned actin filaments and elongated nuclei on narrower micro-channels [110].

More recently, Taneja and colleagues evaluated the effect of 13 μm 316L stainless steel

micro-grooved surface on VSMC phenotypic changes to understand how topography of

endovascular stent contributes to restenosis [111]. They found that micro-grooved

surfaces induce significant cell elongation in addition to significantly higher levels of α-actin expression [111]. These studies suggest that micro- and nano-scaled topographical features can significantly alter the shape of both cell and nucleus and lead to cytoskeletal remodeling.

Altogether, these studies reveal that mechanical properties of the cellular microenvironment can be used as design tools to build VSM with engineered cytoskeletal architecture *in vitro*. The cytoskeleton interacts with multiple signaling pathways by regulating the activation/deactivation state of associated protein complexes [112]. As a consequence of the tight structure-function coupling in VSMC, we would expect that the engineered architecture would influence the VSM functional outcome; thus, there exists a need for a performance metric that will allow researchers to systematically evaluate and optimize the functions of the fabricated VSM tissue.

1.4   Functional Evaluation of Engineered Vascular Smooth Muscle

Although our ability to control the mechanical properties of the cellular microenvironment has become increasingly precise and refined, the ultimate goal for tissue engineers is to harness these mechanical cues to build a functional VSM *in vitro*. This aim will require systematic evaluation and optimization of the VSM tissue design with a standardized performance benchmark or functional metrics. Conventional standard practice evaluates engineered VSM using proteomic assays and cellular morphology; in contrast, we will use evidence from *in vitro* studies to show in the following sections that VSM functions, including proliferation, migration, contraction, and gene expression, are

influenced by cellular architecture and therefore should be included as part of functional evaluation for assessing engineered VSM tissue.

1.4.1 Proliferation

A growing number of studies demonstrate that the proliferation of engineered VSMCs can be influenced by the cytoskeletal architecture *in vitro*. With micropatterned collagen strips of 20, 30, and 50 µm width as well as 30 µm wide micro-grooves on poly-(D,L-lactide-co-glycolide) (PLGA), Thakar and colleagues showed that significantly elongated cell shape and reduced formation of actin stress fiber and α-actin are displayed by VSMCs cultured on 20 and 30 µm-wide collagen strips and micro-grooved PLGA surfaces [92]. Quantification of proliferation with 5-bromo-2'-deoxyuridine (BrdU) showed that these elongated VSMCs have a significantly reduced growth rate. In addition, a study of engineered isolated human VSMCs cultured with micropatterned matrix islands revealed that cells with elongated shape and nuclei have a lower proliferation rate [93]. Aligned and elongated bovine VSMCs engineered on PMMA and PDMS nanopatterned gratings have a reduced proliferation rate [109]. Even in the absence of direct cellular shape manipulation by ECM pattern or topography, isolated porcine VSMCs with a spindle shape also have a significantly lower proliferation rate than rhomboid-shaped cells [113]. These studies provide mounting evidence that cytoskeletal architecture can regulate VSMC proliferation.

Since cells can actively respond to extracellular boundary conditions by remodeling their cytoskeletal organization [85, 114], changes in cell shape could lead to spatially different placement and distribution of mechanosensitive protein complexes,

eventually producing changes in signaling pathway and functions. For example, focal adhesions tend to localize toward the corners of cells [89, 115]. These intramembrane protein complexes transmit mechanical tension from outside of the cell to the cytoskeleton inside the cell [116] and modify activation states of associated signaling proteins [117]. F-actin stress fibers also anchor on the focal adhesions and nuclear lamina, providing a direct physical link for tension to be transmitted to the nucleus [118, 119]. These mechanical connections to the nucleus stabilize intranuclear DNA [73], and cell shape-induced nuclear deformation can lead to chromatin remodeling and DNS synthesis [120]. Collectively, these studies indicate that VSMC proliferation depends on cellular shape and cytoskeletal architecture.

1.4.2   Migration

VSMCs migrate toward the site of vessel injury in response to growth factor gradients. Understanding and regulating VSMC migration has been a focus in treating vascular diseases for preventing post-surgical complications such as thrombogenesis and restenosis. Several studies have demonstrated that VSMC migration depends on VSMC shape and cytoskeletal organization. In one study, maximum migration speed was observed for isolated human VSMCs with the highest ARs [121]. However, a later report showed that cloned human VSMCs under serum-withdrawn conditions and with elongated morphology have a significantly lower migration speed [122]. These contradictory findings may be attributable to differences in cell types, serum conditions, and ECM proteins. A novel isolation method used by Hao et al. to obtain porcine VSMCs with distinct spindle and rhomboid morphologies showed that rhomboid-shaped VSMCs

24

migrate significantly faster than spindle-shaped cells [113]. When cytoskeleton reorganization is inhibited by cytochalasin D, interlukin-6-induced migration of VSMCs is inhibited [123], suggesting that VSMC migration can be regulated by cytoskeleton architecture. More recently, Jiang and colleagues showed that phosphomimetic caldesmon mutant-transfected rat VSMCs with the most robust expression of actin cytoskeleton structure have a significantly lower migration activity compared to VSMCs with normal expression of actin cytoskeleton [124]. Taken together, these studies suggest VSMC migration may be influenced by cellular architecture.

1.4.3   Contraction

The main function of quiescent, fully differentiated VSMCs is to contract or relax the vessel wall in response to pressure and flow changes. In addition to regulating proliferation and migration, which are associated with the synthetic phenotypes of VSMCs, cell shape and cytoskeletal architecture mediate the contractile strength of VSMCs. In desmin-deficient mice, VSMCs isolated from microarteries exhibit lower active and passive tension [125], while isolated VSMCs have higher active force and increased passive compliance [126], indicating the contribution of intermediate filament on VSMC contractility may be cell type-dependent. Pharmacological studies inhibiting actin polymerization with cytochalasin D [43, 45], cytochalasin B [44], and latrunculin B [127] found a complete inhibition of contraction in VSMCs. On the other hand, enhancing actin polymerization with an actin stabilizer, jasplakinolide, increases myogenic tone in rat cerebral VSMCs under intraluminal pressure [47], suggesting that actin organization plays a critical role in VSMC contraction generation. More recently,

Koltsova and colleagues reported that elevation in F- to G-actin ratios in rat VSMCs with hyperosmotic shrinkage and hyposmotic swelling also causes increased contraction [95], suggesting that a contractile response is mediated by actin polymerization. In addition to actin stress fibers, Min and colleagues found regulation of focal adhesion by *Src* modulates differentiated VSMC contractility [29]. By forcing VSMCs into elongated shapes on micropatterned strips of fibronectin and laminin, our group showed an increase in VSMC nuclear eccentricity and a higher degree of cell contraction [90], suggesting that cell shape may modulate VSMC contractility. Taken together, these studies suggest that VSMC contractility is a function of cellular cytoskeletal architecture and cell shape.

1.4.4   Gene Expression

The expression of genes and proteins has been used traditionally to assess the phenotypic state of VSMCs. The activation and deactivation of specific pathways that controls the expression of genes can be mediated by cytoskeletal architecture. For example, rabbit VSMCs in contractile and synthetic states with different organizations of vimentin, actin, and focal adhesion have significantly different expression and distribution of smooth muscle-specific proteins [128]. Inhibiting or enhancing actin polymerization pharmacologically significantly decreases or increases SMC-specific promoter activities, respectively, in rat VSMCs [129], suggesting that actin polymerization regulates SMC-specific gene expression. When a single stretch is applied to rat VSMCs, significant upregulation of smooth muscle-specific contractile proteins is accompanied by an increase in F- to G-actin ratio [81]. However, when the stress fiber network is disrupted pharmacologically, stretch-dependent activation of rat VSMC differentiation markers is abolished [130], indicating that an intact cytoskeleton is

26

required for activation of SMC-specific genes. In addition, Cattaruzza and colleagues reported that zyxin can translocate and accumulate in the nucleus and modulate VSMC-specific gene expression [10], suggesting that cytoskeletal proteins could be directly involved in modulating gene expression. Since the cytoskeleton is mechanosensitive, differences in cytoskeletal architecture can lead to differential activation of genes and proteins, which ultimately provide VSMCs with functional adaptability.

1.5   Conclusions

Vascular smooth muscle functions are highly dependent on the structural organization in multiple spatial scales as a result of the cellular mechanotransduction processes. An engineering algorithm for building functional vascular smooth muscles *in vitro* based on recapitulating the mechanotransduction processes allows us to control for both cellular architecture and function. Importantly, cytoskeleton proteins such as integrin, cadherin, actin, intermediate filaments, and microtubules embedded in the extracellular, intracellular, and intercellular domains are mechanotransductive components that contribute to VSMC form and function. By harnessing the mechanical cues in the cellular microenvironment, such as cyclic tensile stress, cellular shape deformation, ECM interactions, and substrate stiffness and topography, we can build functional VSMCs with engineered cytoskeletal architecture. The performance of these engineered VSMCs should then be evaluated and optimized with functional metrics including proliferation, migration, contraction, and gene expression because of their dependency on cytoskeletal architecture. The development of functional VSM *in vitro* models is particularly relevant for engineering small-diameter vascular grafts, where functional VSM tissue may improve graft patency and long term survival, and replacing

27

expensive animal models in traditional drug discovery research with a cheaper, functional *in vitro* alternative.

With this dissertation, we applied this strategy in the design and assembly of engineered vascular tissues. In chapter 2, we investigated the effect of engineered VSMC shape on its cytoskeletal architecture and contractile strength. In chapter 3, we developed a novel three-dimensional tissue patterning strategy based on folding polymer thin sheet and tested this strategy for building vascularized networks.

2   The Contractile Strength of Vascular Smooth Muscle Myocytes is Shape Dependent

Adapted from Ref. 91 with permission from The Royal Society of Chemistry.

Vascular smooth muscle cells in muscular arteries are more elongated than those in elastic arteries. Previously, we reported changes in the contractility of engineered vascular smooth muscle tissue that appeared to be correlated with the shape of the constituent cells, supporting the commonly held belief that elongated muscle geometry may allow for the better contractile tone modulation required in response to changes in blood flow and pressure. To test this hypothesis more rigorously, we developed an *in vitro* by engineering human vascular smooth muscle cells to take on the same shapes as those seen in elastic and muscular arteries and measured their contraction during stimulation with endothelin-1. We found that in the engineered cells, actin alignment and nuclear eccentricity increased as the shape of the cell elongated. Smooth muscle cells with elongated shapes exhibited lower contractile strength but greater percentage increase in contraction after endothelin-1 stimulation. We analysed the relationship between smooth muscle contractility and subcellular architecture and found that changes in contractility were correlated with actin alignment and nuclear shape. These results suggest that elongated smooth muscle cells facilitate muscular artery tone modulation by increasing its dynamic contractile range.

2.1   Introduction

The contractile function and structure of vascular smooth muscle cells (VSMCs) vary as a function of location in the cardiovascular system [131]. In large diameter elastic

arteries, such as the aorta, VSMCs contract to maintain vessel pressure during cardiac cycle [132]. This is in contrast to mid-sized muscular arteries, such as the external carotid artery of the neck and femoral artery of the thighs, where VSM contracts concentrically to constrict or relax the arterial wall in a process called vascular tone modulation [133]. These functional differences are reflected structurally, where VSMCs exhibit markedly different geometries in these arteries. Although differentiated VSMCs in elastic and muscular arteries have a characteristically spindle shape, the elongated shape of VSMCs in muscular arteries with nearly 15:1 in cell AR, is more pronounced than those found in elastic arteries, which have cell AR about 9:1 [131]. It has been speculated that the VSMC shape may facilitate vascular tone modulation in muscular arteries by providing better dynamic response to blood flow [134, 135] and pressure changes [136]. However, definitive evidence to support this relationship between VSMC shape and contractile function has been limited.

VSMCs undergo significant changes in geometry in physiological and pathological developments. Domenga and colleagues demonstrated rapid VSMC structural changes in postnatal wild-type mice, where VSMCs developed more elongated shape, increased thickness and become circumferentially oriented around the lumen by day 28 compared to immature VSMCs at birth [137]. Genetic deletion of *Notch3*, which is uniquely expressed in arteries but not of veins, led to thin, irregular, rounded shape VSMCs that are poorly orientated around the lumen [137]. In human, *Notch3* mutation leads to a hereditary vascular dementia called cerebral autosomal dominant arteriopathy with subcortical infarcts and leukoencephalopahy (CADASIL), characterized by a cerebral non-atherosclerotic, non-amyloid angiopathy that mainly affects the small

arteries penetrating the white matter. Patients diagnosed with this disease were usually found with more rounded and irregular VSMC shape in small- and middle-sized arteries [138]. During normal vascular repair following injury, VSMCs switch their contractile phenotype to synthetic phenotype and in the process, changing their shape from the elongated spindle morphology to an epithelioid or rhomboid morphology [139]. The epithelioid shaped VSMCs proliferate and produce extracellular matrix to help with the wound healing process [139]. However, the deregulation of this phenotype switching process underlies a number of vascular disorders such as hypertension [140], restenosis [141], and vasospasm [14]. This is supported by pathological studies that observed morphologically distinct VSMC populations between spindle and epithelioid shapes at the site of atherosclerotic intima in the aorta [142-144], carotid artery [145] and coronary artery [146]. Understanding the role of VSMC shape change may elucidate mechanistic insight in the context of cellular physiology and vascular pathology.

In addition to VSMCs, shape change also plays an important role in regulating the physiological and pathological development of other smooth muscle cells and cardiomyocytes. In an early ultrastructural study focusing on the prenatal development of smooth muscle in the human fetal uteri between 12-40 weeks of gestation, Konishi et al. showed immature uterine SMCs changed from a round morphology at week 12-16 to an elongated shape with identifiable dense bodies at week 18 [147]. A clinical and pathological analysis of 26 cases of atypical smooth muscle tumours of the uterus demonstrated that SMC in leiomyoma changed from the typical elongated shape to a rounded, polygonal shape [148]. In cardiac development, cardiac looping is one of the first steps of forming a four chambered-heart that requires bending and twisting of heart

31

tube asymmetrically. It was found that myocardium on the concave side of the heart tube myocardium remains thick and columnar while the convex side flattened and increased in surface area, effectively reducing the AR of the myocardium epithelial tissue [149] and resulting in different contractility on the concave and convex surfaces [150]. In mature adult heart under pathological chronic pressure overload, the heart undergoes concentric hypertrophy, resulting myocytes increase cell width without significant changes in cell length. This, in turn, decreases the normal AR from 7:1 [151-153], as seen for normal ventricular myocytes, to 5:1 [154, 155]. As heart continues to fail, eccentric hypertrophy develops in response to volume overload, which adds sarcomere in series without changing myocytes, cross-section area. This eventually increased the myocytes aspect ratio to 11:1 [152, 153]. Investigating the shape and contractility relationship in myocytes, our group recently reported that myocytes contractility is optimized at AR observed in normal hearts and decreased in cardiomyocytes that resemble AR of failing hearts [88]. In addition, we observed that boundary condition encoded in the extracellular space can regulate myocyte tissue cytoskeletal alignment and function [85, 156, 157]. These studies clearly demonstrated that shape adaptations in smooth and striated muscles can profoundly influence the cellular function.

Recent advances in technologies designed to engineer and probe cell geometries and mechanics has enabled studies demonstrating the relationships between cell shape and architecture and cellular functions such as apoptosis [158], proliferation [120], cytoskeletal and focal adhesion organization [85, 159, 160], and contraction [88, 89, 157]. Utilizing micro-fabrication techniques, our group as well as others have demonstrated at a tissue level that VSM seeded in microgrooves and micropatterned fibronectin (FN)

assumed an elongated morphology [87] as well as oriented remodelling of the underlying matrix [161] and significantly lower cell proliferation rate [93]. Recently, focusing on VSM tissue structure and contractility, we showed that contractile stress of VSMC tissue increased as cell shape elongated within the tissue [90], suggesting that VSM contractility is potentially cell shape dependent. Elsewhere, Wang and colleagues sparsely seeded VSMCs on polyacrylamide (PAA) gel with an isotropic type-I collagen coating and measured an increase in contractile force as cell spreading increased [162]. In another study where VSMC spreading was controlled [93], elongated VSMCs showed reduced proliferation, a cell function commonly associated with cell shape and cytoskeletal tension. While these reports suggest that VSM tissue and cellular structure could influence its function, the role of cell shape in vasomotor tone and contractility was not elucidated. This is important, because controlling cell shape in tissue engineered vascular grafts may be an important strategy for endowing the tissue with a specific drug sensitivity and high fidelity control of the lumen diameter.

We hypothesized that forcing VSMCs to assume increasingly elongated shapes would mimic the VSMC morphology in muscular arteries *in vivo* and induce changes in the intracellular architecture that consequently increase the dynamic contractile range of VSMC in response to contractile stimuli. To test this hypothesis, we engineered VSMCs on micropatterned islands of fibronectin (FN) with ARs of 5:1, 10:1 or 20:1 to mimic VSMC shapes found in elastic and muscular arteries *in vivo*, quantified cytoskeletal and nuclear organization, and directly measured contraction via traction force microscopy (TFM) upon stimulation with a vasoconstrictor endothelin-1 (ET-1). We found cell shape significantly influenced cytoskeletal and nuclear organization and isolated VSMCs of AR

near 20:1 achieved lower basal and stimulated contractile forces but greater percent change in contractile force after stimulation. These results suggest that the elongated shape equips VSMC with a greater dynamic contractile range, facilitating modulation of vascular tone over a broad range by muscular arteries *in vivo*.

2.2   Results

2.2.1   Design of Vascular Smooth Muscle Cell Shape

We engineered the isolated VSMCs by designing three cellular structure parameters: geometry, size and AR. The geometry refers to the number of vertex that the isolated VSMC has. For example, circular or ellipsoidal shaped VSMCs have zero vertices and they belong to the same geometry class. Extending this concept, a spindle-, triangular- and rectangular-shaped VSMC has two, three and four vertices respectively, and they represent three different geometrical classes.

Although healthy, fully differentiated VSMCs usually assume a spindle-like shape *in vivo*, we designed our isolated VSMCs with a rectangular geometry for two reasons. First, isolated VSMC with tapered, spindle-like geometry may be a poor *in vitro* model. Kuo and colleagues demonstrated that airway smooth muscle cells work as a mechanical syncytium by transmitting intercellular force along the principle axis of the cells through mechanically coupled nucleus and aligned F-actin filaments, despite the individual spindle cell shape [72]. They argued when mechanical coupling between neighboring cells are absent, force generation in cells may be distorted, unless the isolated smooth muscle cells are long and the tapered ends are not included in the mechanical measurements. Therefore, by designing our isolated VSMCs in rectangular

geometry, we ascertain the isolated VSMCs are long and without the tapered ends and this allowed us to measure the mechanical output of the entire cell body. The second reason for using a rectangular geometry is a technical one: the longitudinal end-to-end distance is shorter for rectangular geometry than for spindle geometry of the same surface area. This allows us to fit the entire isolated VSMC in one field of view on our microscope when using the 40× objective with a 0.5× optical zoom, up to 20:1 length to width AR. Although grid imaging software can address this issue, it is not preferred in this experimental setup as grid imaging and stitching can introduce error in fluorescent bead location for traction force microscopy and require additional laser exposure cycles, which can be phototoxic to cells for extended live cell imaging. Based on the above two reasons, we designed and engineered our isolated VSMCs to be rectangular in geometry for all studies.

We asked what projected surface area we should use for designing our isolated VSMCs. It is important to have a constant projected surface area for all ARs as smooth muscle cell spreading has been shown to influence cellular function [92]. Since substrate stiffness can lead to changes in cell spreading area [101, 163, 164], we investigated the spreading behavior of VSMCs on both soft (13 kPa) polyacrylamide (PAA) gel [165] and much stiffer glass (73 GPa) substrates. To present identical extracellular matrix (ECM) to the cells, we patterned both substrates with biotinylated-fibronectin isotropically. We induced the contractile phenotype and inhibited cell division by serum starving the VSMCs for 48 hours following an initial 24 hour seeding period with media containing 10% fetal bovine serum (See Materials and Methods). We stained the cell membrane with DiO and the nucleus with DAPI in order to measure the spreading area of single VSMCs.

35

We observed a spectrum of morphology in isolated VSMCs on both PAA gel (Figure 2-1 A-C) and glass (Figure 2-1 D-F) substrates. We categorized the morphology into rhomboid (Figure 2-1 A, D), elongated (Figure 2-1 B, E) and spindle (Figure 2-1 C, F). For some of the spindle-shaped isolated VSMCs, cell length can extend over 300 μm (Figure 2-1 C).
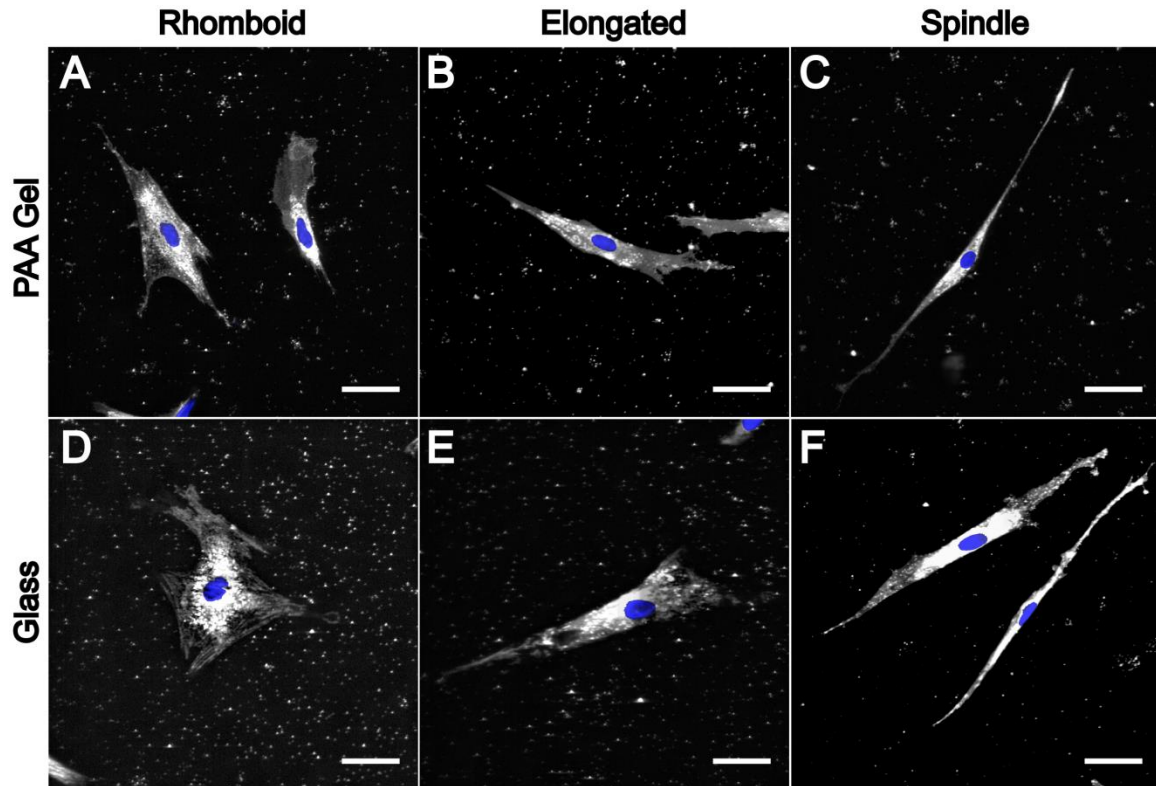
Figure 2-1: Morphology of immunostained isolated vascular smooth muscle cells on soft (13 kPa) polyacrylamide (PAA) gel (A-C) and stiffer (73 GPa) glass (D-F) substrates isotropically patterned with biotinylated-fibronectin. (White: DiO, blue: DAPI). On both substrates, a diverse morphology including rhomboid (A, D), elongated (B, E) and spindle (C, F) were observed. Scale bars = 50 μm.

We measured the projected surface area of single VSMCs by manually tracing the cell borders in ImageJ. We found the projected surface area of single VSMCs on PAA

gel (Figure 2-2 A) and glass (Figure 2-2 B) to be normally distributed with a mean at

4000 μm^2 and 3500 μm^2 respectively. This is consistent with a previous study that found

the spreading area of human aortic SMCs was normally distributed [166]. To provide a

physiologically relevant substrate stiffness, we microfabricated all isolated VSMCs in

subsequent studies with a projected surface area of 4000 μm^2 on PAA gel to minimize the

effect of cell spreading area on cellular function.
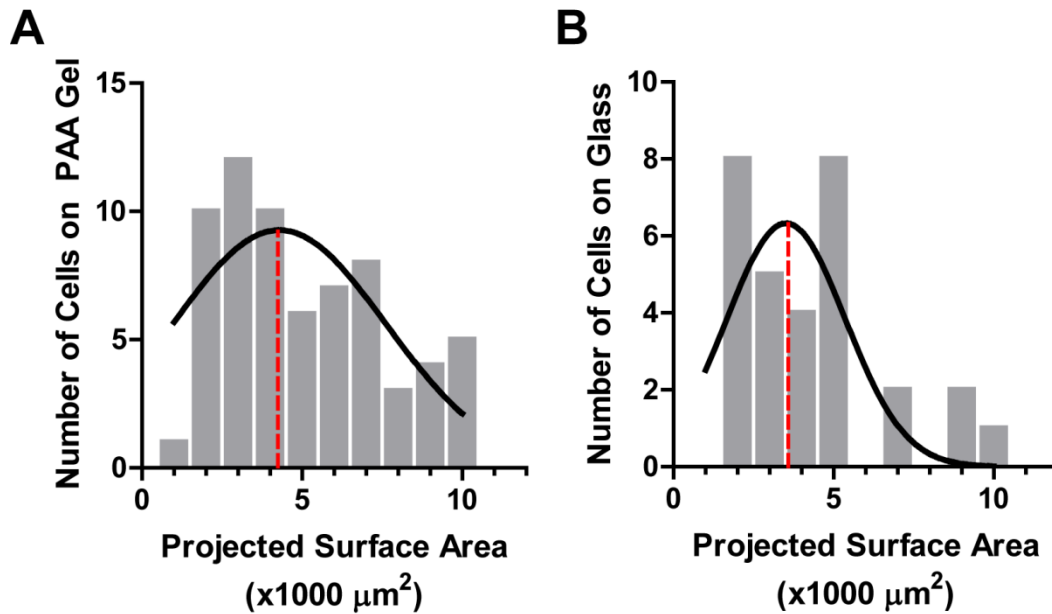
Figure 2-2: Projected surface area of isolated vascular smooth muscle cells is

normally distributed on PAA gel (A) and glass (B) substrate. The mean projected surface

area of VSMCs on PAA gel is higher than those on glass. (Solid line: normal distribution,

red dotted line: mean).

Finally, in order to determine physiologically relevant ARs for designing our

experiment, we surveyed the literature for measurement of AR observed in previous *in

vivo* [131] and *in vitro* [90, 92, 93, 161, 167, 168] studies. A wide spectrum of ARs for

VSMCs was observed ranging from 2 to 50 in studies in the past 3 decades (Figure 2-3).

We selected the 20:1 AR as the upper limit for our study as (1) all studies except one

showed that VSMC ARs did not exceed 20:1 in Figure 2-3 and (2) 20:1 is the upper limit

for a single field of view of the entire cellular body, which reduced cellular phototoxicity

and improved signal to noise ratios during traction force microscopy. We selected 5:1 AR

as the lower limit for our study as (1) it is just below the 8:1 AR observed *in vivo* (Figure

2-3, pink bar) and (2) it permits sufficient cell shape polarization to remain rectangular.

We also selected one intermediate AR of 10:1 to study the transition between the upper

and lower bounds. Taken together, from the selected geometry, size and ARs above, our

finalized design for microfabricated isolated VSMCs were rectangular islands with a

fixed projected surface area of 4000 μm^2 and ARs of 5:1 (141 × 28 µm), 10:1 (200 × 20

µm) and 20:1 (282 × 14 µm).
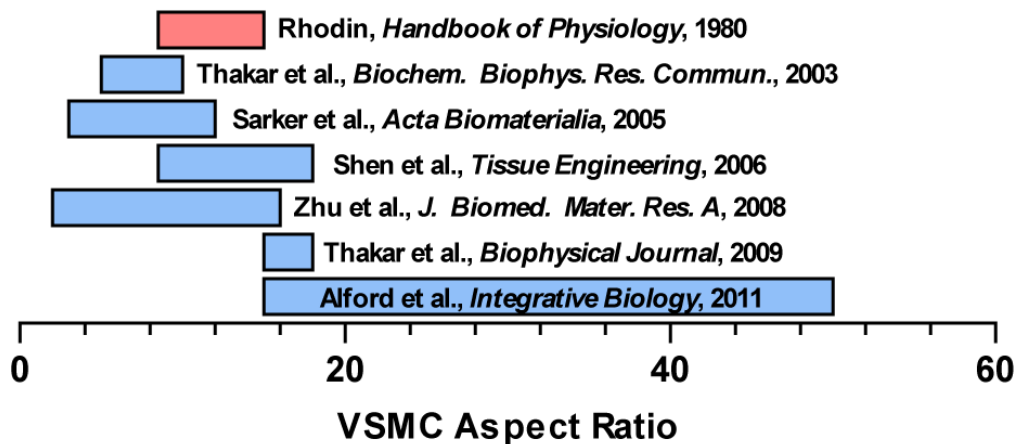
Figure 2-3: Observed aspect ratios of vascular smooth muscle cell from literature.

In vitro (pink) VSMC ARs range between from 10:1 to 15:1 while *in vitro* (blue) VSMC

ARs range between from 2:1 to 50:1.

2.2.2   Microfabricated Isolated Vascular Smooth Muscle Cells

To fabricate isolated VSMCs according to our design parameters, we adopted

methods previously established in our group [88, 89] by culturing VSMCs in defined

media on elastic, 13 kPa PAA gels whose surfaces had been micropatterned with

rectangular FN islands (Figure 2-4). For details, please see Methods and Materials section.
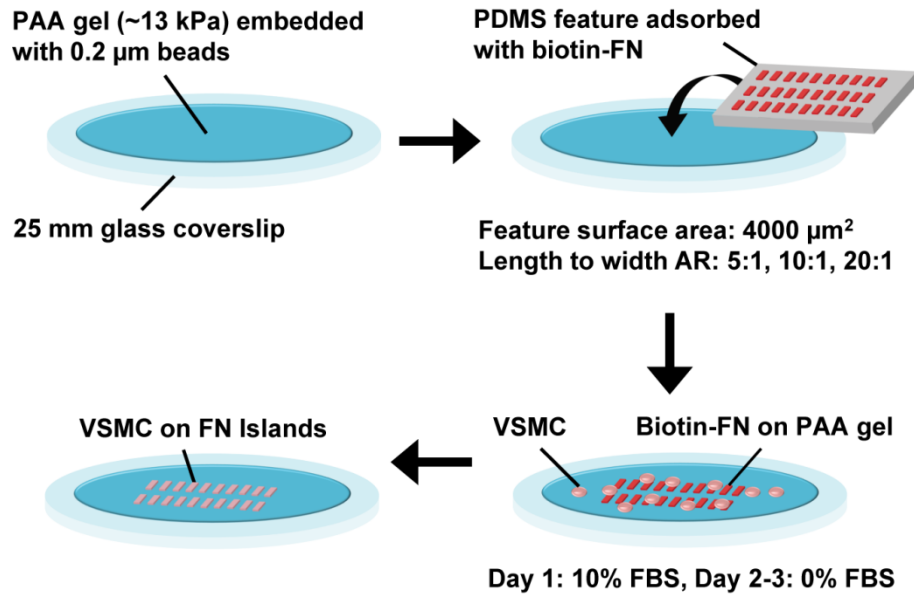
Figure 2-4: Schematic representation of μCP method on polyacrylamide gel to construct isolated vascular smooth muscle cells with different aspect ratios. For details, please see Method and Materials section.

To examine the quality of the micropatterned FN islands, we immunostained the

islands with anti-human FN and found them to be uniform and consistent with high

fidelity (Figure 2-5 A). After 1 day of culture in 10% FBS serum followed by 2 days of

culture in serum-free media on PAA gel with FN islands, seeded VSMCs assumed the

rectangular shape of the patterned FN islands with aspect ratio of 5:1, 10:1 and 20:1

(Figure 2-5 B). By optimizing the initial seeding density, we were able to obtain mostly

island with a single cell present. However, islands occupied with more than one cell were

also occasionally observed (Figure 2-5 B, arrowhead).
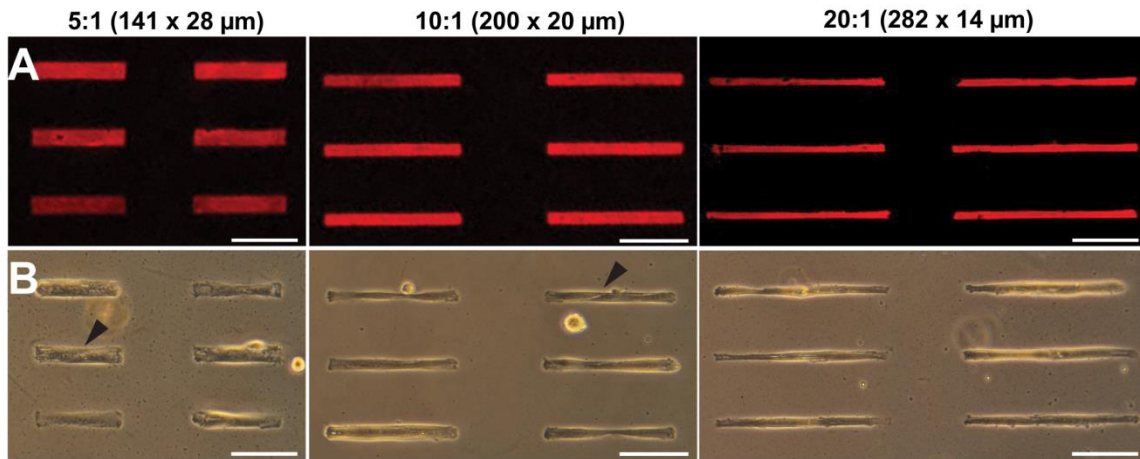
Figure 2-5: Immunostained micropatterned FN islands and microfabricated isolated vascular smooth muscle cells. (A) Anti-human FN staining of patterned biotin-FN on PAA gel. (B) Phase contract images of micropatterned isolated VSMCs with aspect ratio of 5:1, 10:1 and 20:1 and surface area of 4,000 μm^2. Islands occupied by more than one cell had a sinusoidal cell-cell junction (arrow head). (A-B) Scale bars = 100 μm.

We measured the projected surface area, AR and thickness of isolated VSMCs to ascertain the quality and fidelity of the microfabrication process. We immunostained isolated VSMCs of AR 5:1 (Figure 2-6 A), 10:1 (Figure 2-6 B) and 20:1 (Figure 2-6 C) with phalloidin to visualize the cell shape and DAPI to ensure that only single cells were measured. We found that the projected surface areas were similar for all three ARs with mean at 2225 ± 48 μm^2 (Figure 2-6 D). Since VSMCs exert a basal tone at normal resting condition, the reduction in projected surface area is expected as a result of elastic deformation of the soft PAA substrate under cell generated force. The contraction of isolated VSMCs also lead to shape deformation as we found that mean and SEM of ARs of 5:1, 10:1 and 20:1 were 6.8 ± 0.1, 15.3 ± 0.5, 31.3 ± 1.4 respectively. The findings that all three cellular ARs were more elongated than the original design may suggest that

contraction in cell's short axis changed by a greater proportion than the contraction in the long axis.
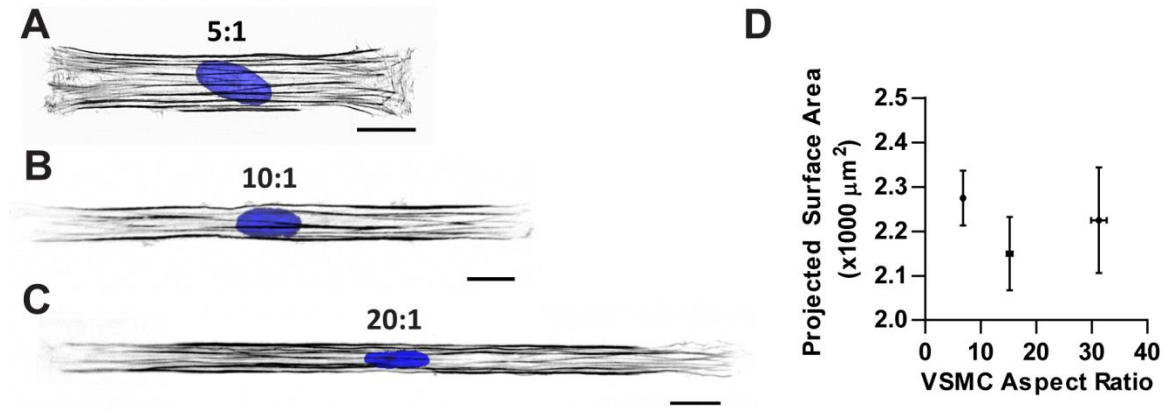
Figure 2-6: Characterization of microfabricated immunostained isolated vascular smooth muscle cells. (A-C) Phalloidin and DAPI stained patterned isolated VSMCs with AR of 5:1 (A), 10:1 (B) and 20:1 (C). (White: F-actin, blue: nuclei). Scale bar = 50 μm. (D) Measured projected surface area and AR of isolated VSMCs. Mean ± SEM. $n = 17$-26 cells from 2-3 coverslips per condition.

To get a sense quantitatively in terms of the magnitude of the contractions in cell's short and long axes, we calculated the shortenings in both directions by assuming the rectangular isolated VSMCs contracted concentrically (Figure 2-7 A). This assumption is based on the observed rectangular shape of contracted isolated VSMCs in Figure 2-5. Since we know the original length (L) and width (W) of the micropatterned FN islands, we can use the following two equations based on the measured projected surface area and cell AR (Fig. 6D) to solve for shortenings in the cell's long (2a) and short axes (2b):

$$Projected\ SA = (L - 2b) \times (W - 2a) \qquad (1)$$

$$Cell\ AR = (L - 2b)/(W - 2a) \qquad\qquad (2)$$

The magnitude (Figure 2-7 B) of shortenings calculated using this simplistic model showed that cell elongation leads to statistically greater shortening in cell's long axis at 20:1 ARs but significantly less shortening in cell's short axis at 10:1 and 20:1 ARs, suggesting that cell shape can influence the magnitude and distribution of contraction. Normalizing the magnitude of shortenings by the original dimensions of the micropatterned FN islands, we found that a significantly lower relative shortening in cell's long axis was achieved by isolated VSMCs with 20:1 ARs while similar relative shortenings in cell's short axis were achieved by all three ARs (Figure 2-7 C). This result suggests that as VSMC becomes elongated, contraction in the cell's long axis becomes weaker. In addition, the relative shortening in the short axis is much higher than the shortening in the long axis, which supports our earlier suggestion that a greater proportion of contraction is achieved in the cell's short axis than the long axis.
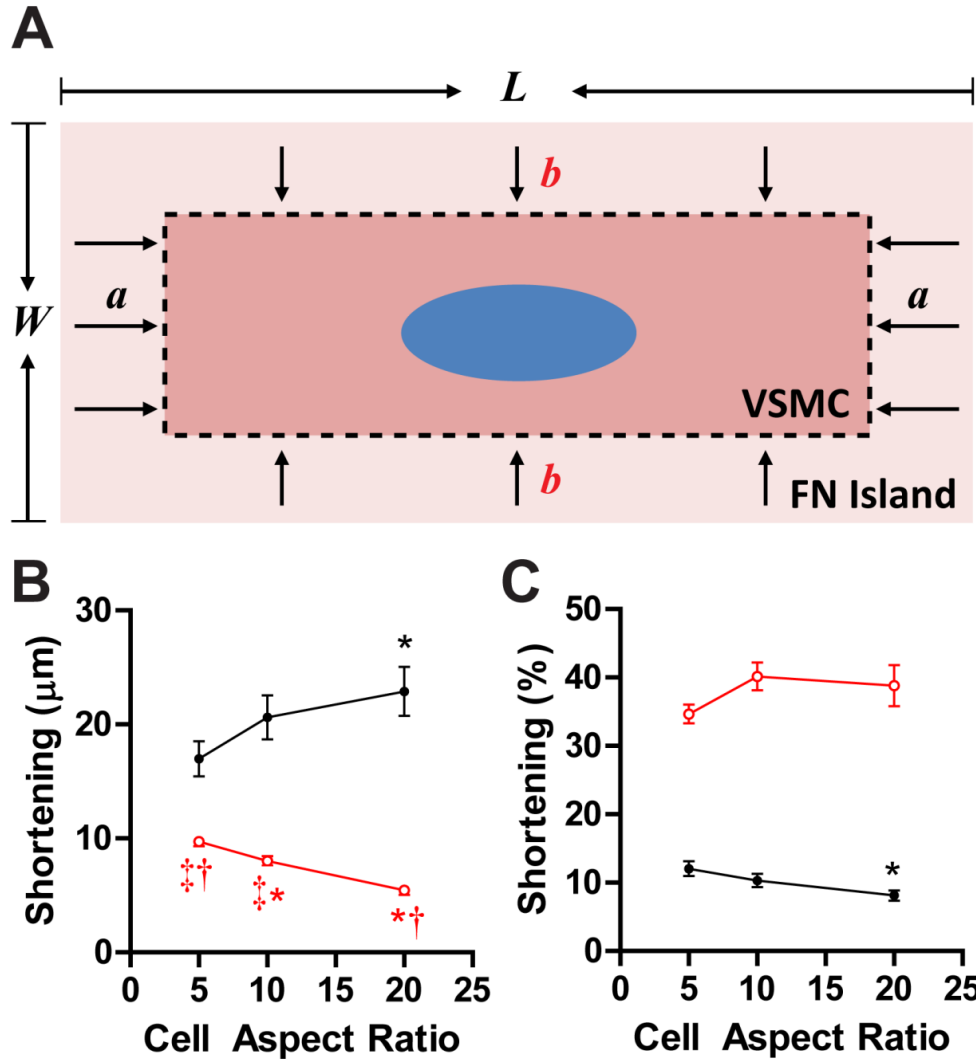
Figure 2-7: Shortening of rectangular isolated vascular smooth muscle cells. (A) Schematic illustration of concentric shortenings in cell's long (*2a*) and short (*2b*) axis. *L* and *W* are the length and width of the micropatterned FN island respectively. (B) Magnitude of shortening in cell's long (black) and short (red) axes. (C) Percent shortening compared to original micropatterned FN island dimensions in cell's long (black) and short (red) axes. (B-C) * = statistically different from 5:1 AR, † = statically different from 10:1 AR, ‡ = statistically different from 20:1 AR. $p < 0.05$. Mean ± SEM. $n = 17$-26 cells from 2-3 coverslips per condition.

We measured cell thickness using deconvolved three-dimensional confocal image stack of phalloidin labeled F-actin fibers of isolated VSMCs (Figure 2-8 A). No statistically significant difference in cell thickness was observed between the three ARs (Figure 2-8 B). Since the measured projected surface areas were similar (Figure 2-6), this result suggested the cell volume was conserved for all three ARs. Taken together this approach enabled us to control the shape of isolated VSMCs with high precision while maintaining cell spreading area, substrate stiffness, growth factor and ECM composition.
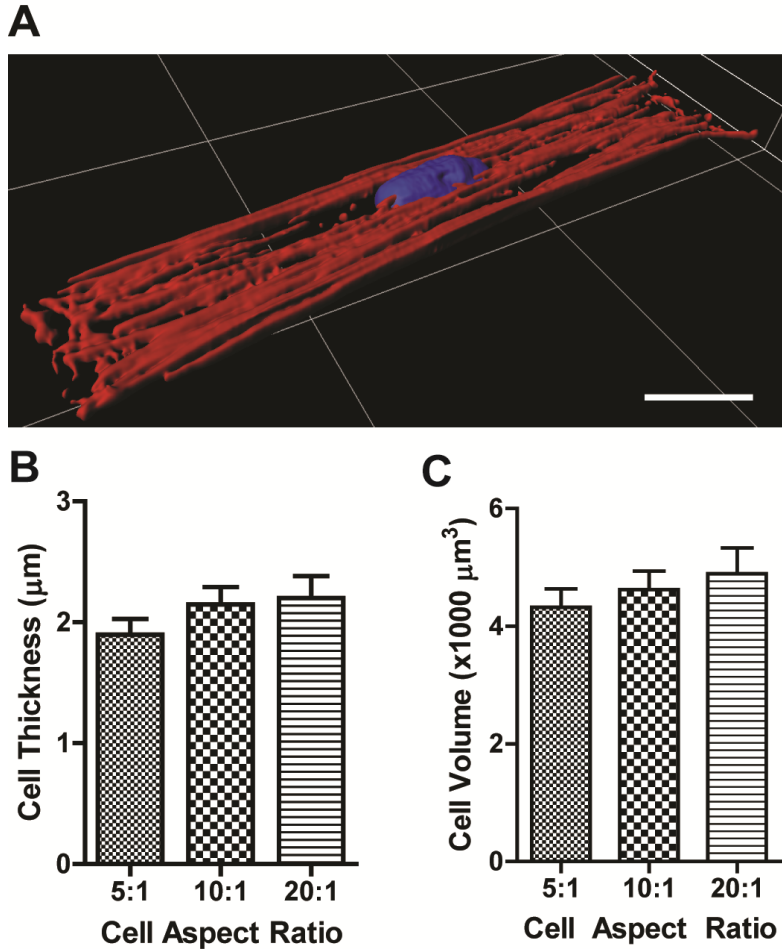
Figure 2-8: Vascular smooth muscle cell thickness and volume are similar for all aspect ratios. (A) Three dimensional rendering of a 5:1 AR VSMC patterned on PAA gel. (Red: F-actin, blue: nucleus). Scale bar = 20 μm. Isolated VSMC thickness (B) and volume (C) as a function of VSMC AR. (B-C) mean ± SEM. n = 7-12 cells per AR.

2.2.3   F-actin Alignment and Organization as a Function of Cell Shape

Previously, we reported variations in cell shape, cytoskeletal alignment, and nuclear shape in engineered vascular tissues assembled on matrix templates with varying geometries [90]. We endeavored to study this cellular remodeling under more controlled conditions. In our engineered cells, we measured the alignment of F-actin (Figure 2-6 A-

C, 5:1, 10:1 and 20:1 respectively) using immunohistochemical staining. The orientation of the F-actin fibers was calculated using a method based on structure tensor method [169] and quantified by calculating the orientational order parameter (OOP), a method borrowed from crystallography and previously reported by our group [170]. We found that F-actin OOP increased significantly as cell AR increased (Figure 2-9), suggesting that as the cell's long axis was extended, the transverse boundary conditions on the cell potentiated the alignment of polymerizing actin with the cell's long axis.
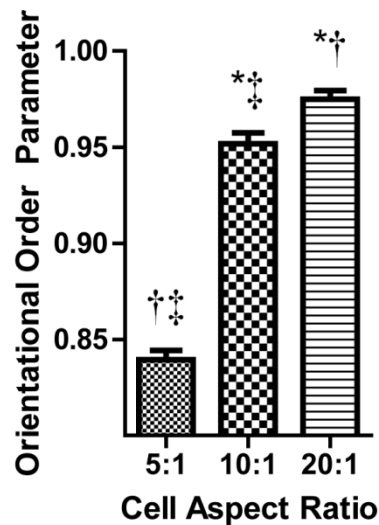
Figure 2-9: Orientational order parameter (OOP) of F-actin fibers of isolated vascular smooth muscle cells. VSMCs with higher ARs had a greater F-actin OOP value, suggesting more aligned F-actin fibers. * = statistically different from 5:1 AR, † = statically different from 10:1 AR, ‡ = statistically different from 20:1 AR. $p < 0.05$. All bars: mean ± SEM. n = 7-12 cells per AR.

2.2.4 Nuclear Deformation as a Function of Cell Shape

The cell nucleus interacts with cytoskeleton [118] and deforms when extracellular stresses were applied [171]. Changes in nuclear shape have been proposed to cause conformational changes in chromatin structure and subsequently influence transcriptional level and cell function [172]. We characterized nuclear shape changes by measuring the changes in nuclear angle offset, projected area and eccentricity (Figure 2-10 A-C, 5:1, 10:1, and 20:1, respectively) by manually outlining the stained nuclei in the plane of the culture surface (Figure 2-10 D). Nuclear angle offset, which measures the difference in orientation between the major axes of the ellipse that best fits the cell body and nucleus (Figure 2-10 A), was significantly lower for cells with 20:1 ARs (Figure 2-10 E). The projected area of the nucleus in these cells was found to decrease significantly for cells with 10:1 and 20:1 ARs (Figure 2-10 F). Consistent with previous findings [90], nuclear eccentricity significantly increased as cell AR increased (Figure 2-10 G).
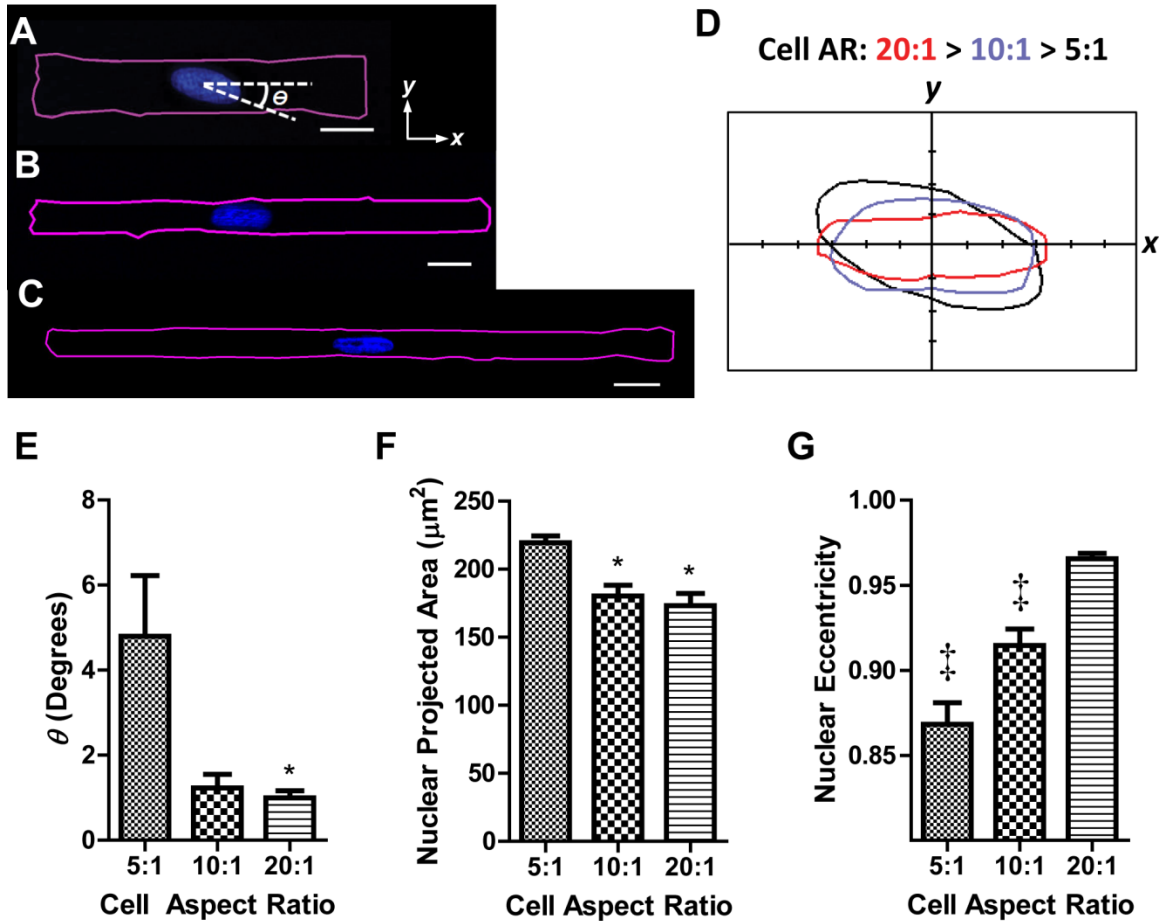
Figure 2-10: Morphological changes in nuclear shape as isolated vascular smooth muscle cell elongates. (A-C) Manual traces of cell border with nuclei of isolated VSMCs. (Magenta: cell border, blue: nuclei). Nuclear orientation offset, θ, is shown between the two dotted white lines in (A), representing the major axes of the ellipses that best fit the cell body and nucleus respectively. Scale bar = 50 µm. (D) Superimposed nuclear outlines from cells in A-C show clearly the difference in nuclear eccentricity, orientation offset and projected area as cell AR increases. (H) F-actin orientational order parameter (black) and nuclear orientation offset (red) as a function of VSMC ARs. (I) Nuclear eccentricity (black) and projected area (red) as a function of VSMC ARs. * = statistically

Figure 2-10 (Continued) different from 5:1 AR, † = statically different from 10:1 AR, ‡ = statistically different from 20:1 AR. $p < 0.05$. (E-G) mean ± SEM. $n = 7\text{-}12$ cells per AR.

We wanted to test whether changes in nuclear morphology could be explained by a decrease in nuclear volume resulting from cell lengthening [120]. Based on three-dimensional rendering of nucleus (Figure 2-11 A), we assumed an ellipsoid morphology for the nucleus (Figure 2-11 B) and quantitatively evaluated the length, width and height of the ellipsoid (Figure 2-11 C). However, we found that nuclear volume and nuclear surface area were conserved at 475 ± 32 μm^3 and 464 ± 21 μm^2, respectively, independent of alterations in AR (Figure 2-11 D). These data suggested that the elongated cell shape leads to higher degree of nuclear deformation, without any change in nuclear volume.

A

B

$$V = \pi\frac{4}{3}abc$$

$$SA \approx 4\pi\left(\frac{a^p b^p + a^p c^p + b^p c^p}{3}\right)^{1/p} \quad p = 1.6075$$

C

D
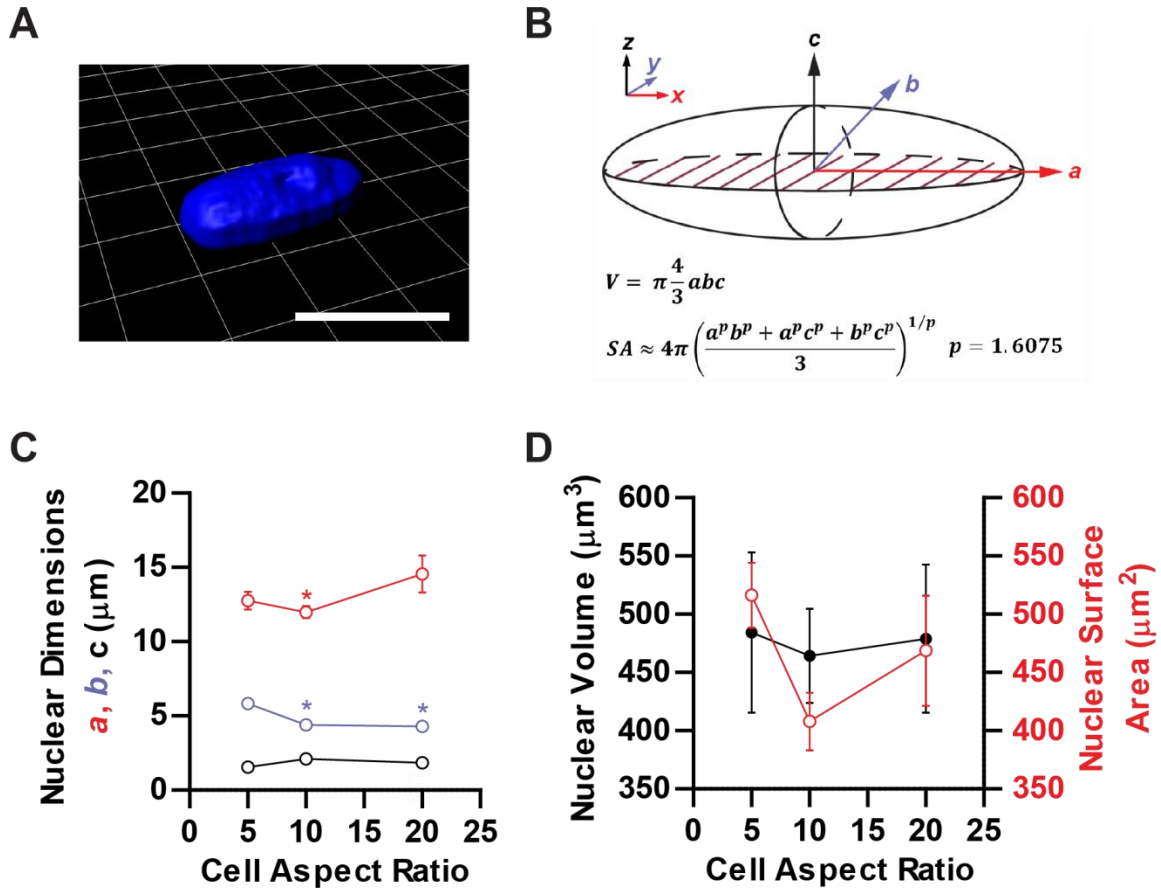
Figure 2-11: Nuclear volume and surface area of isolated vascular smooth muscle cells. (A) A Three-dimensional rendering of 5:1 AR VSMC nucleus. Scale bar = 20 μm. (B) Schematic representation shows the half-length (*a*, red), the half-width (*b*, blue) and half-height (*c*, black) of a nucleus with assumed ellipsoid shape. (C) Measured nuclear dimensions from three-dimensional confocal image stacks as a function of cell AR. * = statistically different from 5:1 AR. (D) Nuclear volume and surface area do not differ significantly between different cell ARs. (C-D) mean ± SEM. *n* = 7-12 cells per AR.

2.2.5   Development of Stimulation Protocol for Studying Cell Contraction

The primary contractile function of elongated VSMCs in muscular arteries is local tone modulation in response to systemic and local signals to contract or relax the

vessel wall [173]. We hypothesized that in our *in vitro* system, the elongated VSMC

shape would improve its dynamic contractile range in response to an external stimulus.

To test this hypothesis, we used traction force microscopy to measure the force generated

by cells on the PAA gel substrate when stimulated with a vasoconstrictor, endothelin-1

(ET-1), to induce cell contraction or rho-associated kinase (ROCK) inhibitor, HA-1077,

to induce cell relaxation. Since VSMCs respond to stimulations on the order of minutes

to hours [90], we first assessed the amount of time needed for VSMC traction to

equilibrate after we dose the drugs. We imaged the cells every 4 minutes and found that

isolated VSMCs produced a constant traction force prior to ET-1 dosing, which is known

as basal tone (Figure 2-12). After ET-1 was added, we observed a small but noticeable

gradual increase in cell traction until it peaked 16 minutes later. In the next 30 minutes,

the traction gradually decreased until it returned to baseline level. We subsequently dosed

HA-1077 to the imaging media and noticed an immediate and dramatic decrease in

traction until 16 minutes later, where it equilibrated near zero. These results suggested

that isolated VSMCs could equilibrate their traction output within 16 minutes after drug

dosing.
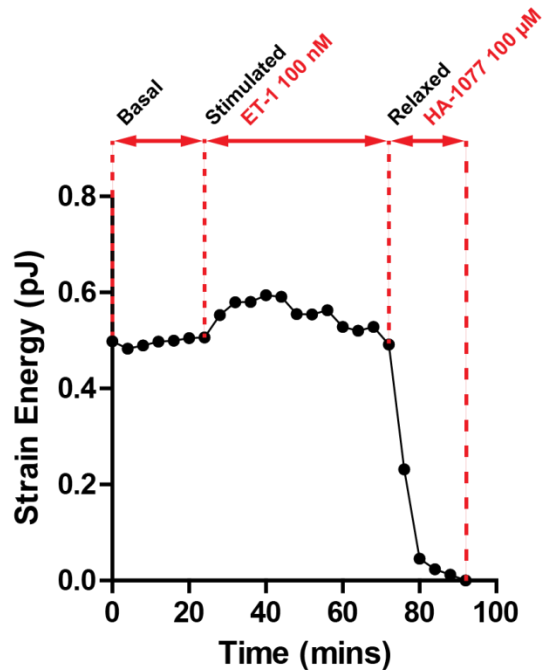
Figure 2-12: A representative traction profile for an isolated vascular smooth muscle cell in response to endothelin-1 and HA-1077 treatment. A constant basal tone was maintained for the first 24 minutes. After ET-1 at 100 nM was added, traction peaked in about 16 minutes but returned gradually to basal level in about 28 minutes. A saturating dose of rho-associated kinase (ROCK) inhibitor HA-1077 at 100 µM caused an immediate and dramatic decrease in traction and eventually diminished close to 0 after 16 minutes.

In order to allow sufficient time for VSMC to equilibrium after drug dosing and to minimize the amount of potential phototoxicity caused by excessive laser exposure, we developed a TFM protocol to measure contractile strength of isolated VSMC with varying ARs exerted on the substrate pre- and post-stimulation with ET-1 (Figure 2-13 A). Prior to stimulation, we imaged the basal tone of isolated VSMCs. At 8 minutes, we stimulated contraction of the isolated VSMCs with a 100 nM dosage of ET-1. At 31 minutes, we treated cells with a 100 µM dosage of HA-1077, to induce relaxation of the

cells. Finally at 60 minutes, we terminated the experiment by trypsinizing the cells from the substrate such that there was no traction on the substrate in order to establish a reference for calculation of bead displacements. For each condition, three consecutive images separated by 4-minute intervals were taken to ensure consistency in VSMC contractile output and to minimize potential phototoxic effect of laser imaging. This protocol allowed us to assess the contractile strength of isolated VSMCs in response to external stimuli while minimizing potential phototoxicity during live imaging.

2.2.6   Quantification of Vascular Smooth Muscle Cell Contractile Strength by Traction Force Microscopy

Prior to stimulation, we ascertained that isolated VSMCs fully occupied the rectangular FN islands by differential interference contrast (DIC) imaging. High fidelity rectangular isolated VSMCs with AR of 5:1 (Figure 2-13 B), 10:1 (Figure 2-13 C) and 20:1 (Figure 2-13 D) were selected for TFM experiment. We defined the AR of an isolated VSMC at its basal state prior to stimulation as the cellular AR. As a convention, we further defined the longitudinal and transverse directions of isolated VSMCs as the *x*- and *y*- axes, respectively (Figure 2-13 B). Prior to ET-1 stimulation, basal traction stresses were observed for isolated VSMCs with AR of 5:1 (Figure 2-13 E), 10:1 (Figure 2-13 F) and 20:1 (Figure 2-13 G). Following ET-1 stimulation, traction stress intensity and area both increased for AR 5:1 (Figure 2-13 H), 10:1 (Figure 2-13 I) and 20:1 (Figure 2-13 J) isolated VSMCs. After HA-1077 treatment, traction stress was significantly reduced for isolated VSMC with AR of 5:1 (Figure 2-13 K) and completely absent for AR of 10:1 (Figure 2-13 L) and 20:1 (Figure 2-13 M). After cells were detached by

53

trypsin, traction stress was completely absent for all ARs (Figure 2-13 N-P, respectively).

For all three ARs, we observed that the basal (Figure 2-13 E-G) and ET-1 stimulated

(Figure 2-13 H-J) traction stresses were localized at the two ends of the cells and pointed

towards the geometric centre of the cell where the nucleus is generally located. This

phenomenon became more pronounced for isolated VSMCs with AR 10:1 (Figure 2-13 F,

I) and AR 20:1 (Figure 2-13 G and J). This result suggests that focal adhesion complexes

formed by isolated VSMCs were localized towards the two ends of the cells.
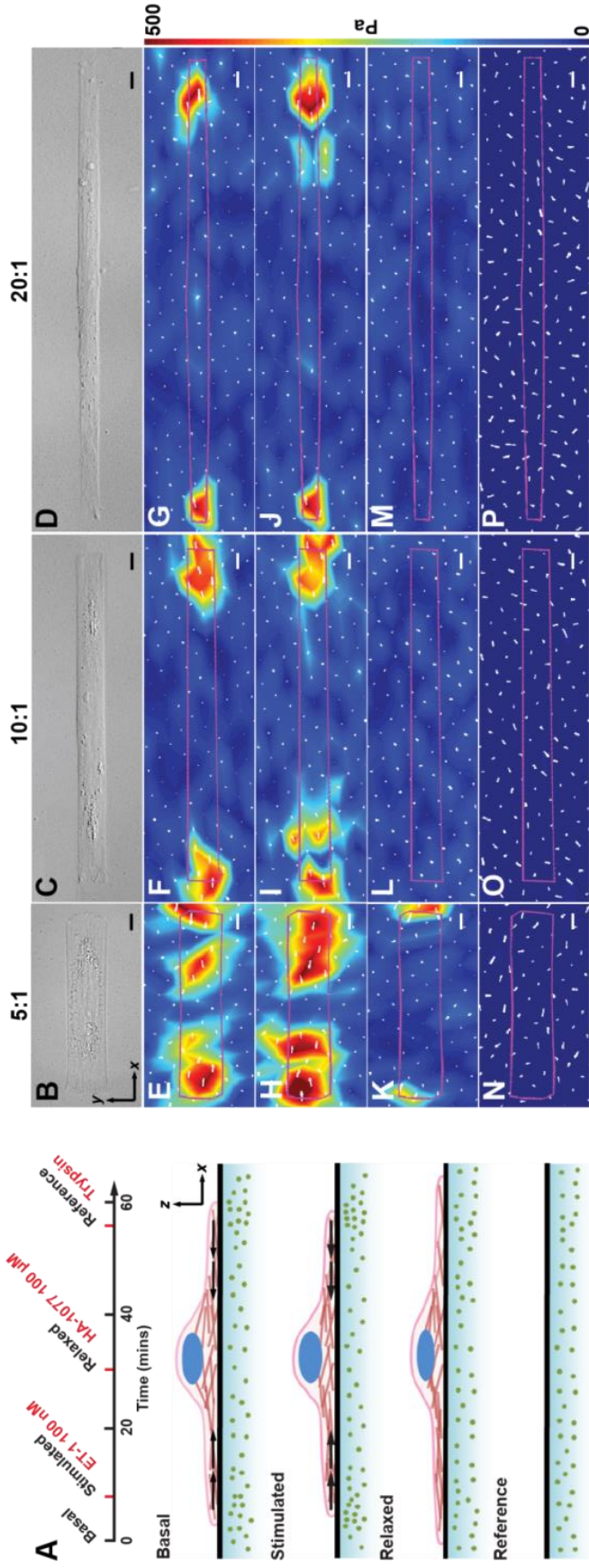
Figure 2-13: Traction force microscopy experimental protocol and representative stress spatial maps of isolated vascular smooth muscle cells. (A) Drug administration timeline of TFM experiment for isolated VSMCs and corresponding schematic representations of cell-substrate interaction at different stages. DIC images of isolated VSMC of AR 5:1 (B), 10:1 (C) and 20:1 (D) and corresponding traction stress maps at basal (E-G), after stimulation with 100 nM endothelial-1 (H-J), after treatment with 100 μM HA-1077 (K-M) and finally detached with 0.5% v/v trypsin (N-P). The longitudinal and transverse directions of the cell are defined in x- and y-axis in (B). E-P has the same color scale to the right side. (B-P) scale bar = 10 um.

We first quantified the contractile strength of isolated VSMCs by computing the strain energy (U) [174] from beads displacements at basal, stimulated, and relaxed conditions with respect to cell-free reference condition. Strain energy is a scalar measurement that integrates tractions exerted in all directions (Figure 2-14 A), which enabled us to measure the overall changes in cell contraction. In response to ET-1 stimulation, the isolated VSMCs further contracted, increasing the measured strain energy from the initial basal tone (U_b) to a higher level, here denoted as U_c (Figure 2-14 B). Both U_b and U_c were relatively constant over the period measured, indicating that equilibrium contractions have been reached. To assess the dynamic contractile range of isolated VSMCs in response to ET-1, we computed the relative contractile increase in strain energy (K_u) by normalizing the increase from basal tone to the ET-1 stimulated tone with the basal tone. These measurements allowed us to quantitatively assess both the absolute magnitude and relative changes in contractile strength of isolated VSMCs in response to external stimuli.

2.2.7 Isolated Vascular Smooth Muscle Cell Contractile Strength Correlated with Cellular Aspect Ratio

To characterize how cell shape affects the contractile strength of isolated VSMCs, we plotted the AR of each isolated VSMC against its measured U_b, U_c and K_U. We found that U_b (Figure 2-14 C) and U_c (Figure 2-14 D) both negatively correlated with cell AR. This suggested that the absolute contractile strength of isolated VSMC weakens as they elongate. However, relative contractile increase (Figure 2-14 E, K_U) significantly increased as cell AR increased, which indicates that elongated VSMCs exhibited a

56

greater percent change in contractile strength in relation to its basal tone after stimulation with ET-1. Taken together, these results suggest that elongation of the cell AR causes a decrease in contractile strength but an increase in overall dynamic contractile range of the cell.
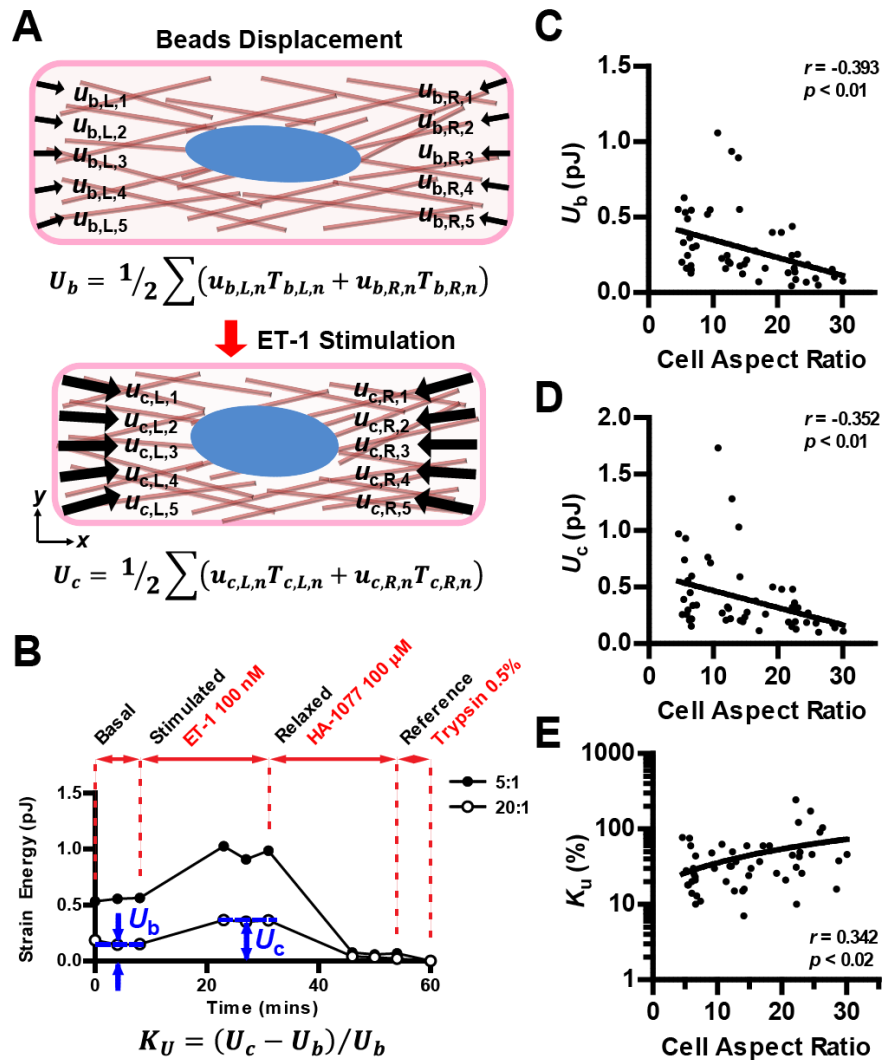
Figure 2-14: Vascular smooth muscle cell aspect ratios correlated with strain energy output. (A) Schematics illustrating calculations for strain energy from beads displacement and traction force of an isolated VSMC at basal (U_b) and after stimulation with ET-1 (U_c). (B) Representative temporal strain energy profiles of isolated VSMCs with AR 5:1 (lower bound) and 20:1 (upper bound) prior and post stimulation. Relative

Figure 2-14 (Continued) contractile increase in strain energy (K_U) is defined as the per cent change in strain energy from basal to ET-1 stimulated. U_b (C), U_c (D) and K_U (E) plotted as a function of isolated VSMC ARs. (C-E) The correlation efficient, r, is determined by linear regression analysis. Reported p values for Pearson correlations are two-tailed, demonstrated that the correlation is significantly different from zero.

To gain further insight into the component breakdown of the contractile strength, we computed the contractile traction force of isolated VSMCs [174] similar to strain energy from beads displacement at basal, stimulated and relaxed conditions in reference to cell-free condition. Since traction force is a vector measurement, we could probe for changes in contractile strength either in the cell's long axis (longitudinal, Figure 2-15 A) or short axis (transverse, Figure 2-16 A). Similar to strain energy, we observed a relative constant contraction force in both longitudinal (T_{bx}, Figure 2-15 B) and transverse (T_{by}, Figure 2-16 B) directions prior to ET-1 stimulation, indicative of the cell basal tone. In response to ET-1 stimulation, the isolated VSMCs contracted, increasing the measured longitudinal traction force from the initial basal tone (T_{bx}) to a higher level, here denoted as T_{cx} (Figure 2-15 B). Similar increases were also observed in transverse traction force (T_{cy}, Figure 2-16 B) suggesting isolated VSMC contracts in all directions. We again computed the relative contractile increase in the longitudinal (K_{Tx}) and transverse (K_{Ty}) directions by normalizing the increase in traction force with the basal tone force. We found in the longitudinal direction that while T_{bx} and T_{cx} are negatively correlated with the cell ARs (Figure 2-15 C-D), K_{Tx} showed a significant positive correlation (Figure 2-15 E), suggesting that as VSMC elongates, its contractile range increased at the expense of lower absolute contractile strength.
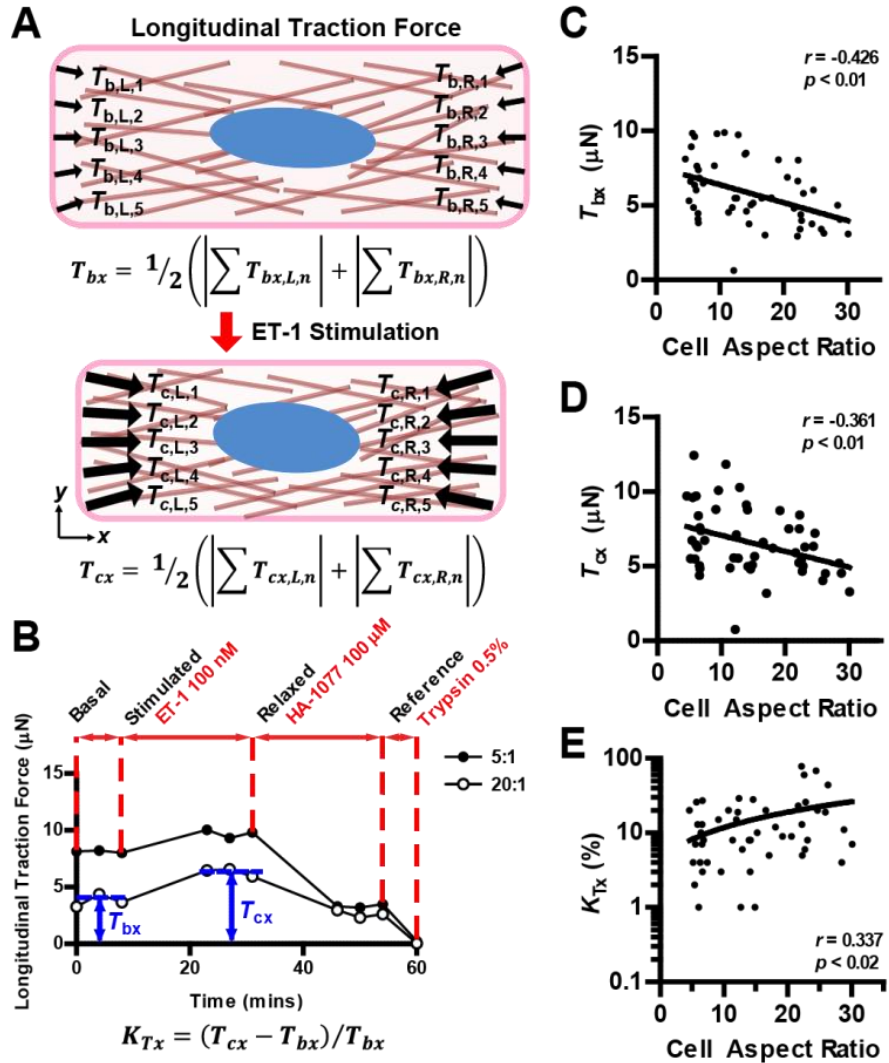
Figure 2-15: Vascular smooth muscle cell aspect ratios correlated with longitudinal traction force. (A) Schematics illustrating calculations for longitudinal traction force of an isolated VSMC at basal (T_{bx}) and after stimulation with ET-1 (T_{cx}). (B) Representative temporal longitudinal traction force profiles of isolated VSMCs with AR 5:1 (lower bound) and 20:1 (upper bound) prior and post stimulation. Relative contractile increase in longitudinal traction force (K_{Tx}) is defined as the per cent change in longitudinal traction force from basal to ET-1 stimulated. T_{bx} (C), T_{cx} (D) and K_{Tx} (E) plotted as a function of isolated VSMC ARs. (C-E) The correlation efficient, r, is determined by linear regression

Figure 2-15 (Continued) analysis. Reported p values for Pearson correlations are two-tailed, demonstrated that the correlation is significantly different from zero.

However, in the transverse direction, no correlation was found between cell AR and T_{by}, T_{cy} and K_{Ty} (Figure 2-16 C-E), suggesting that longitudinal contraction is the main driving factor for observed difference in contractile output as cell elongates. Taken together, our results suggest that cell shape elongation increase the contractile range and decrease the contractile magnitude only in the direction of elongation.
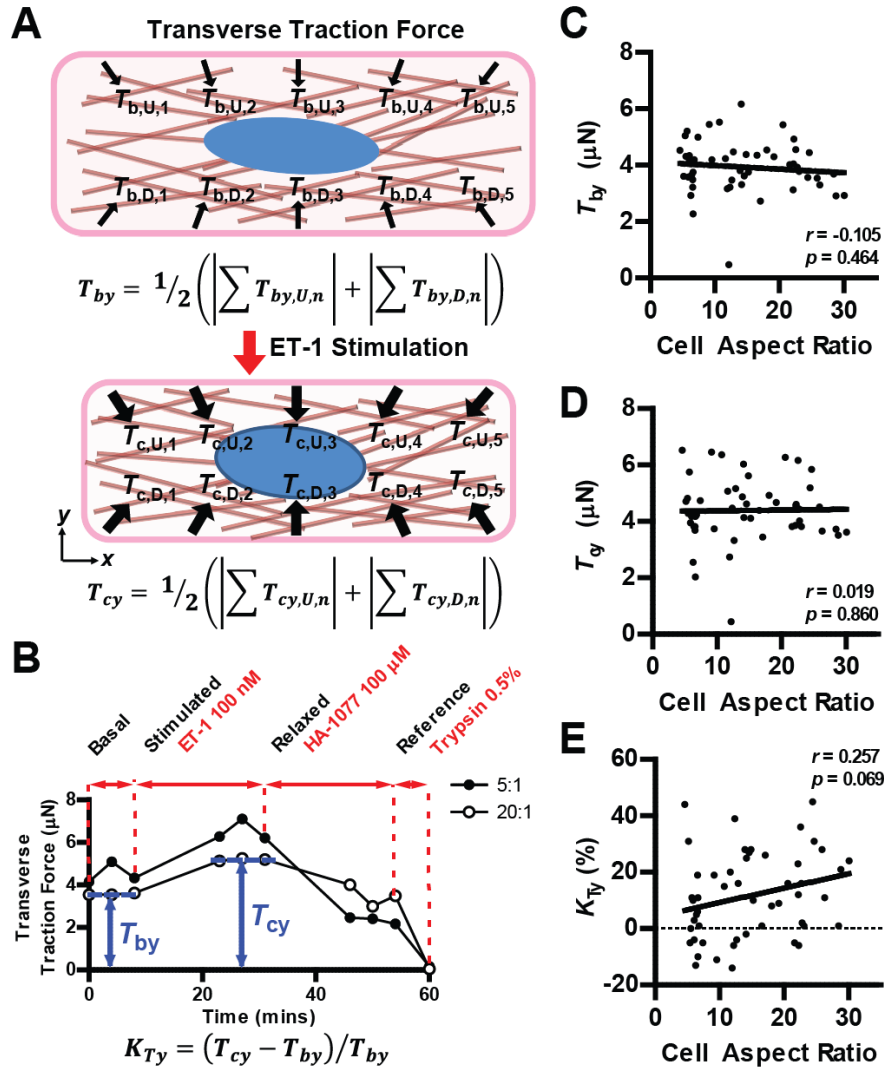
Figure 2-16: Transverse traction force is similar for all cellular aspect ratios. (A) Schematics illustrating calculations for transverse traction force of an isolated VSMC at basal (T_{by}) and after stimulation with ET-1 (T_{cy}). (B) Representative temporal transverse traction force profiles of isolated VSMCs with AR 5:1 (lower bound) and 20:1 (upper bound) prior and post stimulation. Relative contractile increase in transverse traction force (K_{Ty}) is defined as the per cent change in transverse traction force from basal to ET-1 stimulated. T_{by} (C), T_{cy} (D) and K_{Ty} (E) plotted as a function of isolated VSMC ARs. (C-E) The correlation efficient, r, is determined by linear regression analysis. Reported p

Figure 2-16 (Continued) values for Pearson correlations are two-tailed, demonstrated that the correlation is significantly different from zero.

We asked if the increase in relative contractile increase in longitudinal direction (K_{Tx}) is solely caused by the decrease in basal tone force (T_{bx}). To address this question, we computed the ET-1 stimulated contractile force increase for each individual cell and plotted it against its ARs (Figure 2-17). We found that there is a wide distribution in traction force increase induced by ET-1 at all ARs and no statistically significant correlation was found. This suggests that ET-1 induced the same level of contraction in cell's long axis regardless of the cell AR and the decrease in basal tone force (T_{bx}) is play an important role in the decrease of relative contractile increase (K_{Tx}).
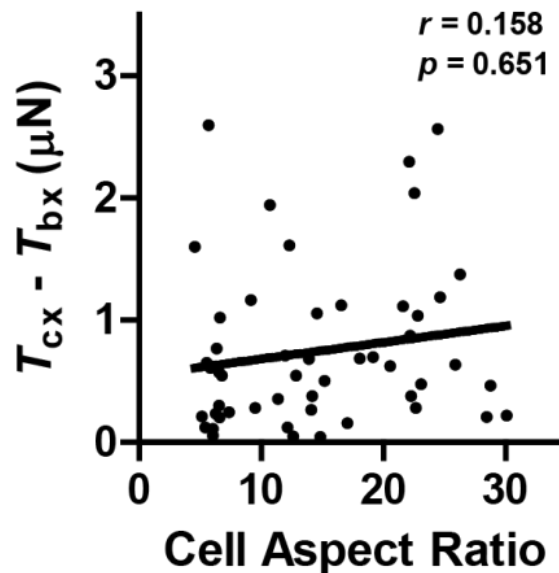
Figure 2-17: Endothelin-1 induced increase in longitudinal traction force is similar for all cell aspect ratios. A wide distribution in the absolute increase of longitudinal traction force was found for all cellular aspect ratios

In cellular tensegrity model, tensile stress, known as prestress, bore by the F-actin filaments are responsible for stabilizing the cytoskeletal network that gives the cell

shape [175]. Assuming that the force transmitted along the F-actin fibers are balanced by the traction force generated at the cell-substrate interface (Figure 2-18 A), cumulative prestress in the F-actin fibers can be obtained by dividing the longitudinal traction force (T_x) over the cross-sectional area (A') of the cell that is perpendicular to the cell's long axis. Since isolated VSMC thickness (Figure 2-8 B) remains constant while cell width (Figure 2-7 B) decreased as cell shape elongates, the cross-sectional area (A'), the product of cell width and cell thickness, must decrease proportionally as cell width is reduced. By dividing the measured longitudinal traction forces T_{bx} (Figure 2-15 C) and T_{cx} (Figure 2-15 D) by the cross-sectional area, we calculated the cumulative prestress at basal state (P_{bx}) and after ET-1 stimulation (P_{cx}) (Figure 2-18 B). We found that P_{bx} (Figure 2-18 C) and P_{cx} (Figure 2-18 D) increased as cell AR increased respectively, suggesting that a higher tensile stress is experienced for F-actin fibers of elongated cells. Similar to strain energy and traction forces, we calculated the relative contractile increase in cumulative prestress (K_{Px}, Figure 2-18 E) by normalizing the increase in prestress (P_{cx} − P_{bx}) to basal prestress (P_{bx}). We found that K_{Px} increased significantly with respect to cell AR, suggesting that the changes in actin fiber prestress increased more in cells with higher cell ARs than those with shorter ARs.
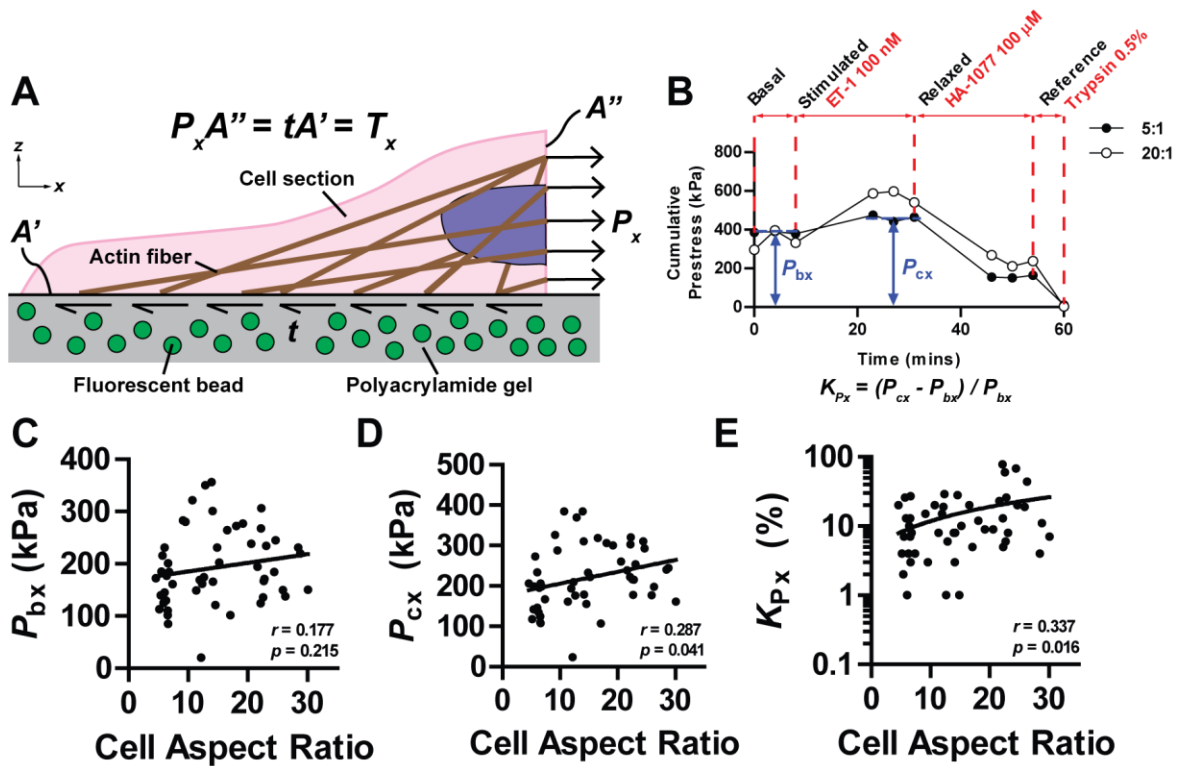
Figure 2-18: Vascular smooth muscle cell aspect ratio correlated with longitudinal cumulative cellular prestress. (A) Schematics showing a free-body diagram of a section of cell. Traction forces at the cell-gel interface (tA') must be balanced by the internal stress in the cell body (P_xA''), mainly by the tension bearing actin fibers. In the force balance, $P_xA'' = tA' = T_x$, where P_x is the cumulative prestress, t is the traction stress, A' is the cell-gel interfacial area, A'' is the cross-sectional area of the cell section, and T_x is the measured longitudinal traction force. (B) Representative temporal longitudinal cumulative prestress profiles of isolated VSMCs with AR 5:1 (lower bound) and 20:1 (upper bound) prior and post stimulation. Relative contractile increase in longitudinal cumulative prestress (K_{Px}) is defined as the per cent change in longitudinal cumulative prestress from basal to ET-1 stimulated. P_{bx} (C), P_{cx} (D) and K_{Px} (E) plotted as a function of isolated VSMC ARs. (C-E) The correlation efficient, r, is determined by linear

Figure 2-18 (Continued) regression analysis. Reported *p* values for Pearson correlations are two-tailed, demonstrated that the correlation is significantly different from zero.

2.2.8   Cell Shortening as a Function of Cell Shape

A previous study demonstrated that more polarized cells have reduced Rho-dependent actomyosin contractile activity [176]. We asked if the reduction in overall force generation is a result of fewer actomyosin cross-bridge cycling activities in VSMCs with more aligned F-actin fibres. Since cross-bridge cycling directly leads to cell shortening [177], we quantified longitudinal cell shortening ($\mathit{\Delta L}$) from the changes in cell length during contraction with respect to basal and relaxed states (Figure 2-19 A). We found that $\mathit{\Delta L}$ increased for VSMC with higher ARs (Figure 2-19 B) and this increase is positively correlated with OOP values (Figure 2-19 C). These results suggested that cross-bridge cycling is unlikely to be the cause for the reduction in overall force generation.
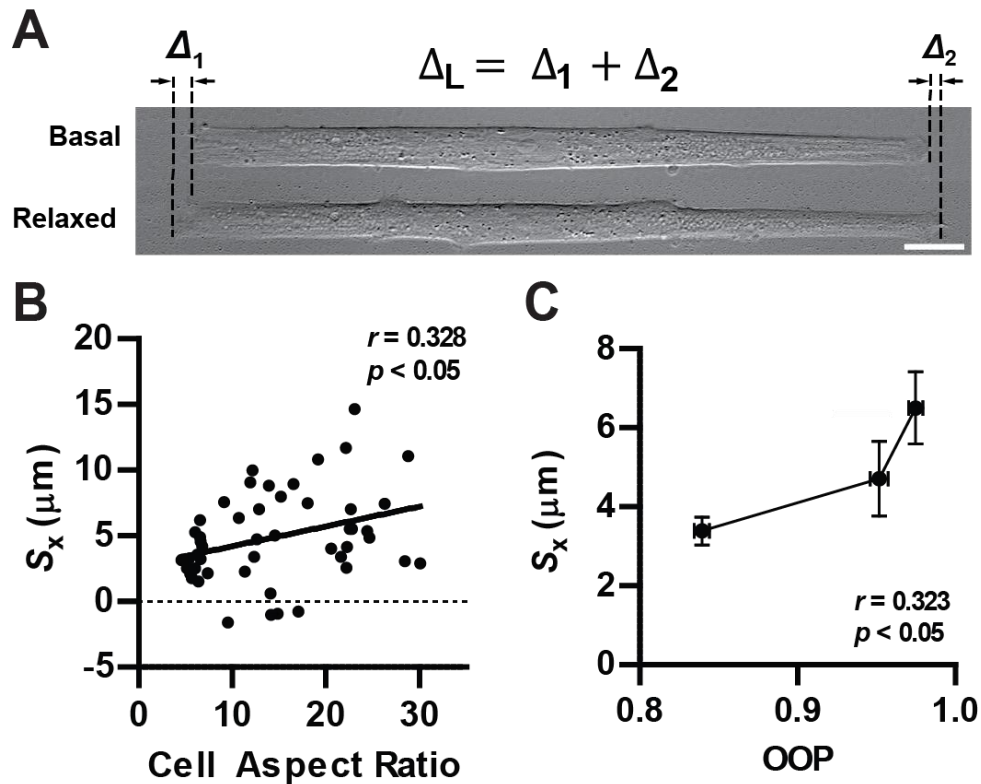
Figure 2-19: Longitudinal cell shortening correlated with cellular aspect ratio and orientational order parameter. (A) DIC images showing longitudinal cell shortening (ΔL) of a 20:1 AR VSMC calculated from cell length difference on both ends of cell body between basal and relaxed conditions. Scale bar = 20 µm. ΔL as a function of cell AR (B) and OOP (C). The correlation coefficient, r, is determined by linear regression analysis. (B-C) Reported p value is two-tailed, demonstrating that the correlations are not significantly different from zero. (B): n = 14-17 cells from 4-6 experiment per AR. (C): n = 13-18 cells per condition. All error bars are mean ± SEM.

2.2.9   Contractility Correlated with Subcellular Organization

We asked whether differences observed in F-actin cytoskeletal organization would reflect the differences in contractility of the cells. To answer this question, we grouped isolated VSMCs into 5:1, 10:1 and 20:1 ARs and compared their actin alignments with initial basal tone (T_{bx}) and relative contractile increase (K_{Tx}). We found that as OOP increased, T_{bx} decreased while K_{Tx} increased (Figure 2-20 A), suggesting that more aligned F-actin fibres enables greater relative increase in force generation along the fibre direction at the expense of weakened overall force output.

Nuclear shape and surface area is influenced by cell morphology [178] and subsequently affects other cellular functions [120]. Our recent work showed that nuclear eccentricity is positively correlated with VSM tissue contractility [90]. We asked if nuclear shape and projected area are also suggestive of the observed differences in isolated VSMC contractility. We grouped isolated VSMCs into 5:1, 10:1 and 20:1 ARs and compared nuclear eccentricity and projected area with T_{bx} and K_{Tx}. Here, we found that as projected nuclear area increased, T_{bx} increased while K_{Tx} decreased significantly (Figure 2-20 B). However, as nuclear eccentricity increased, T_{bx} decreased while K_{Tx} decreased significantly (Figure 2-20 C). These data suggested the morphological changes in VSMC nucleus may be an important metric for assessing the absolute and relative contractile strength of VSMCs in response to external stimuli.
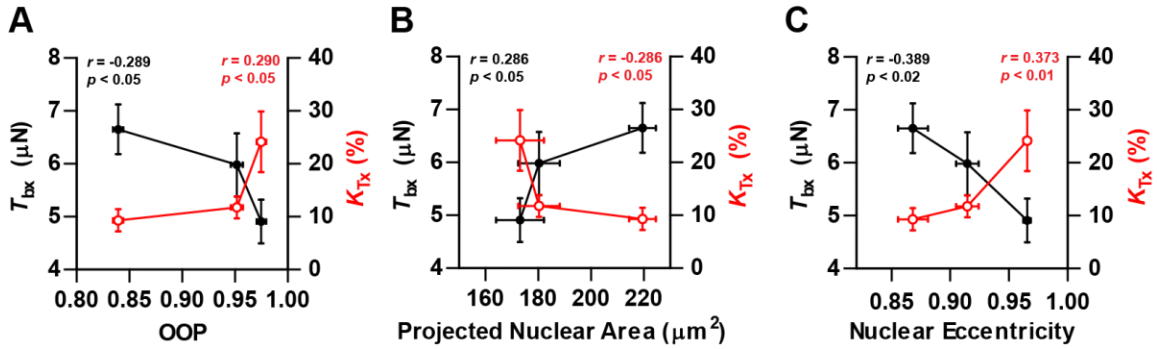
Figure 2-20: Contractile output correlated with cytoskeletal organization and nuclear morphology. Basal longitudinal traction force (T_{bx}, black) and relative contractile increase (K_{Tx}, red) in longitudinal traction force after ET-1 stimulation (K_{Tx}, red) as a function of OOP (A), projected nuclear area (B) and nuclear eccentricity (C). The correlation coefficient, r, is determined by linear regression analysis. Reported p values for Pearson correlations are two-tailed, demonstrated that the correlation is significantly different from zero. All plots: mean ± SEM. $n = 13\text{-}18$ cells per condition.

2.3   Discussion

In this study, we showed that VSMC shape can regulate its contractile function. We found that whereas wider width cells generate a greater force when stimulated with ET-1, but that longer, thinner VSMCS have a greater range of contraction relative to their basal tone. This suggests that where the vasculature requires a higher fidelity in its modulation of blood flow, longer, thinner cells are functionally advantageous. This is particularly relevant to vascular tissue engineering where there is a requirement that vascular grafts are compatible both anatomically and functionally at the graft site [179-181]. In the past two decades, several strategies have been explored to recapitulate the 3D architectural organization in native vessels [182]. Customarily these strategies rely on

seeded cells to migrate and self-assemble into tissues with minimal guidance. While

arterial replacements can be engineered *in vitro*, when engrafted, the compliance

mismatch between the graft and native vessel results in thrombosis and intimal

hyperplasia at the anastomotic site, resulting in low patency rate [183, 184]. Our findings

suggest that, in addition to closely matching the biomechanical aspects of healthy artery,

engineering vascular grafts with VSMC shapes that mimic cellular architecture of the

native, healthy vasculatures could improve functionality and long-term patency.

Morphology has been an important parameter in the definition of smooth muscle

cell phenotypes, especially when protein marker data is not available [139]. Our result

shows that individual VSMCs cultured on soft PAA gel and stiff glass substrates with

isotropically patterned FN both exhibited a wide distribution of morphologies from

rhomboid to spindle-like, suggesting that we may have VSMCs with both synthetic and

contractile phenotypes present despite the effort to differentiate VSMC into contractile

phenotype by serum starvation. A previous study demonstrated that VSMCs cultured on

stiffer substrate composed of dehydrated collagen fibrils led to a more proliferative,

synthetic phenotype compared to the softer hydrated collagen fibrils [185]. However,

even on the much stiffer glass substrate, we still observed spindle-like morphology,

highlighting the need of a combinatorial, multi-pronged approach for regulating VSMC

phenotype that may include biochemical, mechanical, and extracellular matrix factors

present in the cellular microenvironment.

In addition to the variance in morphology, we also observed that individual

VSMC spreading area is normally distributed on both PAA gel and glass substrates. This

is consistent with results reported by Tolic-Norrelykke and colleagues [166] where they

found the projected surface area of human aortic smooth muscle cells is normally distributed. This may be a result of the intrinsic diversity of VSMC in the vessel wall where immunohistochemical staining pattern of contractile VSMC phenotype markers revealed highly heterogeneous staining patterns and intensity between adjacent SMCs. [186, 187] This spectrum of phenotypes expressed in VSMCs has been suggested to be a combinatorial effect of both genetic programing and local environmental factors. [139] Taken together, these studies and our result suggests isotropic ECM signal would lead to a wide distribution of VSMC phenotype *in vitro*, additional structural, biochemical or mechanical cues are needed to homogenize the population phenotype.

We previously reported that engineered VSM with forced elongated spindle shapes exerted greater contractile tensile stress when chemically stimulated [188]. The results reported herein are consistent with the findings by Tolic-Norrelykke and Wang, where they found that cells with wider width contracted with greater force than slimmer cells with a similar projected area [166]. The differences in observed shape-contractility relationship between the current findings and our previous study by Alford and colleagues may be attributed to differences in measured quantities, experimental techniques and cellular micro-environmental conditions. Our previous study utilized the muscular thin film technology [189-191], which measured the contractile strength of the VSM tissue with the component of Cauchy stress along the cell orientation. This measured quantity represented contractile force per tissue cross-sectional area, whereas the current study quantified the contractility of VSMCs via TFM, which measured the contractile force and strain energy exerted by the cell on the substrate. In addition, the engineered VSM tissue tested in Alford et al. was cultured with a higher level of cell-cell

contact, the possibility of off axis alignment of cells, and stiffer abiotic substrates as compared to this single cell study. These differences in micro-environmental conditions will influence VSMC phenotype [102] and functions [36, 37, 192-195]. As a result, measured contractile strength may be reduced as it reflects an average of all cells in the tissue, including weakly or non-contractile cells and cells oriented in off-axis compared to the global orientation of the tissue.

Tension development and generation requires F-actin network to activate myosin ATPase activity and cross-bridge cycling in all forms of muscles, including smooth muscle cells.[2] In isolated smooth muscle cells where intercellular mechanical couplings are absent, actin filaments anchored at focal adhesion complexes must balance intracellular tension by transmitting the force to the substrate. Our findings that reduced F-actin fiber alignment correlated with VSMCs with higher contractile strength suggest that higher contractile forces were bore by the less organized F-actin fibers than the aligned fibers. This is reasonable as an increased cell width permits more sites at the two ends of the cells for the formation of focal adhesion complex, which has been shown to play an important role in the stabilization of tension bearing F-actin fibres [196]. The wider cell also has more degree of freedom laterally for the F-actin fibre orientations, which explains the lower overall alignment. This cell shape mediated cytoskeletal remodelling also corroborated with our findings that decreased F-actin fibre alignment correlated with lower relative contractile increase and less cell shortening: a phenomenon that can explained by the model proposed by Seow, Ford and co-workers [197, 198] as actin filaments rearrange connections from a parallel fashion in shorter cells to a serial

fashion in elongated cells. Taken together, our results suggest that cell shape dependent contractility changes in smooth muscle cells may be mediated by cytoskeletal modelling.

Three possible mechanisms have been put forward to explain the F-actin fiber remodeling process. Gunst et al. have proposed a model that suggest cell shape adaptation is a result of a shift in the connection of actin filaments terminations among the adhesion plaques to which it may attach by modifications in length and number of actin filaments [199]. Seow et al. suggested a second mechanism that attributed the remodeling process as a parallel-to-series transition and cell elongation could lead to rearrangement of crossbridges or addition of thick filament in series [198, 200]. The third mechanism proposed by Solway et al. is a variation of second mechanism that suggested that systematic modulation in actin filament length is responsible for cell shape changes, which means cells with shorter actin filaments may undergo parallel-to-series transition while longer actin filament do not as cell elongates [201]. Although we did not directly measure for change in actin filament length, we found that relative shortening in cell's long axis reduced significantly while it remained comparable in cell's short axis as cell elongated, suggesting that different mechanisms may be governing the shortening process depending on the length of the cell's axis. This is in support of the third mechanism proposed by Solway et al. as shorter actin filaments undergo parallel-to-series remodeling as cell shape elongates [201]. While the increase in F-actin alignment during the cell elongation process could be attributed to the decrease in lateral freedom in the orientations of actin filaments as a result of reduced cell width, a parallel-to-series remodeling in actin filaments may also increase the overall alignment, in support of this

mechanism. However, to definitively test this hypothesis, measurement of individual polymerized F-actin fibers is needed.

Mechanical forces exerted on the exterior of a cell are propagated into the cell via the cell cytoskeleton to the nuclear lamina [118, 119], directly affecting nuclear shape and gene transcription. While cell shape induced nucleus elongation has been well documented, the relative contribution between longitudinal tension and lateral compression imposed by the stress fibres on the nucleus is unknown [72]. Our finding that nuclear eccentricity negatively correlated with longitudinal traction force suggests that lateral compression forces exerted by stress fibres physically deforms the nucleus. This observation agrees with a recent report detailing how lateral compressive forces exerted on the nucleus are responsible for shape deformation, chromatin remodelling and reduced cell proliferation [120]. Others have proposed that compressive physical forces exerted by aligned actin fibres are required to expose transcription binding sites or DNA regulatory motifs, potentiating differences in DNA-associated protein binding and gene transcription [202]. Since nuclear shape deformation is correlated with physiological [90, 120, 203-205] and pathological [206-209] changes in cellular functions, nuclear deformation may be indicative of, and further distinguish, the function and phenotype of vascular smooth muscle.

In this study, we demonstrated that isolated VSMCs with elongated shape exhibited less contractile strength but greater relative contractile increase upon stimulation. This shape-dependent contractile behaviour suggests that the elongated shape of VSMC in muscular arteries may lead to improved dynamic contractile range, a key feature required for effective vascular tone modulation *in vivo*. In addition to providing

73

mechanical insight into the physiological structure-function relationship of VSMCs, our finding is particularly important for obtaining the desired VSMC contractile function from a clinical perspective in the design of a functionally active tissue engineered graft.[210] Our data suggest that providing organizational guidance cues to guide the development and assembly of VSMC into elongated shape may be beneficial in a successful implantation of a small artery graft.

2.4   Experimental Challenges

Completing this section posed many experimental challenges, especially in regards to microfabrication of rectangular isolated VSMCs. Despite the fact that microcontact printing has been widely used in many groups including ours, the micropatterning technique used in this section uses a modified protocol in order to accommodate the soft PAA gel substrate, which requires drying of the PAA gel prior to transferring of the biotinyated FN from the PDMS micro-features. However, if the PAA gel is too dried, the gel will crack and even upon hydration, the substrate is no longer usable for subsequent micropatterning. Therefore, this step requires a careful balancing act that leaves only a narrow window of a few minutes drying time. To complicate this matter further, factors such as humidity, the amount of residue fluid on the PAA gel prior to drying and the thickness of the gel could all influence the optimal drying time, resulting a relative low rate of success in FN micropatterning and a steep learning curve initially. However, with more experience in experimental technique to minimize batch-to-batch variations and careful monitoring during the drying process over time, we were

74

eventually able to master the micropatterning technique and achieve a relatively high success rate.

Another challenge we encountered is to ensure the isolated VSMC stay adhered on the micropatterned islands for immunohistochemical staining. In the early phase of the study, we adopted without modification the cell culturing protocol from a previously published study from our group on VSM tissue of the same cell type [90]. This protocol specifies a 2-day culture post seeding in 10% FBS containing media followed by a 1-day serum free starvation period to induce the contractile phenotype of the VSMC. However, we discovered that this protocol did not work well for our study because: (1) the initial 2-day culture in 10% FBS media led to a significant proliferation of seeded VSMCs which caused most of the islands to be occupied by more than 1 single cell as visible during the DAPI immunohistochemical staining (data not shown) and (2) the 1-day serum starvation period was not long enough to fully induce the contractile phenotype uniformly among the microfabricated isolated VSMCs as initial assessment of micropatterned VSMC projected surface area showed a wide distribution, suggesting that not all cells have reached their equilibrium contracted state. One plausible explanation for this discrepancy maybe that when cell-cell contact is present in the case of VSM tissues in previous study, contractile phenotype is more quickly established [211]. However, in the case of isolated VSMCs, contractile phenotype establishes more slowly as only biochemical cue is present in the cellular microenvironment. We addressed these issues simultaneously by decreasing the post-seeding 10% FBS serum culturing period from 2 days to 1 day and lengthening the subsequent serum starvation from 1 day to 2 days. Following the implementation of this protocol, we obtained a higher percentage of single celled islands

by day 3 with uniform projected surface area for all ARs, suggesting a more uniform phenotype expression.

One major challenge involved with live cell imaging is the possibility of phototoxicity induced by the reactive oxygen species (ROS) generated from ambient and laser light exposures [212]. In order to monitor how isolated VSMC contractility responds to different vasoactive agents, we needed to image the cells for over 1 hour under the confocal microscope for TFM studies. This is much longer than conventional TFM studies for cardiomyocytes commonly done in our group, where a typical imaging cycle lasted only a few seconds. As a result, the repeated laser and ambient light exposures over the course of TFM led to VSMC phototoxicity in the form of cell blebbing, necrosis, and eventual delamination from the substrate. To address this issue, we increased the imaging interval from 1 minute to 4 minutes and also reduced the laser and ambient light power to the minimal level that could still be used for TFM analysis. While we lost temporal resolution for VSMC contractile kinetics, we were still able to measure the equilibrium contractile state achieved when stimulated with different vasoactive agents. With reduced imaging interval and light power greatly, most of the VSMCs imaged no longer present any signs of phototoxicity and the small percentages of VSMCs that did were excluded from subsequent analysis.

2.5 Methods and Materials

2.5.1 Sample Preparation

2.5.1.1 *Photolithography*

Photolithographic chromium mask for microcontact printing were designed in AutoCAD (Autodesk Inc.) and fabricated at the Center for Nanoscale Systems facility with Heidelberg DWL-66 mask writer. The design for traction force microscopy (TFM) studies, consisted of rectangles of approximately 4,000 μm^2 surface area and variable length to width ratios (5:1, 141 μm x 28 μm; 10:1, 200 μm x 20 μm; 20:1, 280 μm x 14 μm). Silicon wafers (Wafer World) spin-coated with SU-8 2002 negative photoresist (MicroChem Corp.) were exposed to ultra-violet (UV) light to cross-link the designed pattern. Uncross-linked regions were dissolved by submerging the wafers in propylene glycol methyl ether acetate.

2.5.1.2 *Microcontact Printing of Polyacrylamide Gels*

ECM protein FN after biotinylation modification was microcontact printed onto the polyacrylamide (PAA) substrate, as previous published.[4] Briefly, FN was cross-linked with biotin using Sulfo-NHS-LC-Biotin (Pierce). 13 kPa PAA gel substrate was fabricated with 5/0.1% acrylamide/bis concentration. Immediately prior to gel polymerization, streptavidin-acrylamide and 200 nm fluorescent beads were added to the gel solution for a final concentration of 1:5 and 1:100, respectively, by volume. 15 μL of gel-bead solution was cured on activated 25 mm coverslips. 200 μg/mL biotinylated fibronectin (biotin-FN) was incubated on a PDMS (Sylgard 184, Dow Corning, Midland, MI) stamp with microscaled raised features for 1 h at room temperature and blown dry gently. The biotin-FN coated PDMS stamp was placed in contact with cured PAA gel, transferring the biotin-FN pattern to the substrate. The patterned PAA gel was stored in

phosphate buffered saline (PBS) until cell seeding. When seeded, cells were constrained to the ECM patterned portion of the substrate after serum starvation.

2.5.2   Human Umbilical Arterial Smooth Muscle Cell Culture

Human umbilical artery smooth muscle cells (Lonza, Walkersville, MD) purchased at passage 3 was cultured in growth medium consisted of M199 culture medium (GIBCO, Invitrogen, Carlsbad, CA) supplemented with 10% fetal bovine serum (FBS, Invitrogen), 10 mM HEPES (GIBCO, Invitrogen, Carlsbad, CA), 3.5 g L^{-1} glucose, 2 mg L^{-1} vitamin B-12, 50 U mL^{-1} penicillin and 50 U mL^{-1} streptomycin (GIBCO). All experiments were performed at passage 6-7.

VSMCs were seeded in growth media at 5,000 cells cm^{-2} and allowed to attach to the isotropically patterned FN on PAA gel or patterned biotin-FN islands on PAA gel for 24 hours before replaced with a growth factor free medium consisted of M199, 10 mM HEPES, 3.5 g L^{-1} glucose, 2 mg L^{-1} vitamin B-12, 50 U mL^{-1} penicillin and 50 U mL^{-1} streptomycin to induce a contractile phenotype for 48 hours prior to cell staining or TFM experiments.

2.5.3   Fluorescent and Immunohistochemical Staining

VSMCs seeded on PAA gel after 3 d of culture were fixed with 4% formaldehyde solution (Thermo Scientific Pierce) for 10 minutes prior to staining. VSMCs seeded on isotropically patterned FN were stained for cell membrane (DiO, Invitrogen) and nucleus (DAPI) while VSMCs seeded on patterned biotin-FN islands were stained for F-actin (phalloidin, Molecular Probes) and nucleus (DAPI). Patterned

78

FN islands were stained with rabbit anti-human fibronectin antibody (1:100 dilution, Sigma-Aldrich, St. Louis, MO) followed by Alexa Fluor 647 conjugated anti-rabbit secondary antibody (1:100 dilution, Abcam). The stained samples were then mounted with ProLong Gold antifade agent (Molecular Probes) and stored in -20°C freezer until imaging.

2.5.4   Cell, F-actin, and Nucleus Image Analysis

The spreading area of single cells on isotropically patterned FN was manually traced in ImageJ (*rsbweb.nih.gov/ij/*) and quantified. Cell AR was calculated by manually tracing the phalloidin stain in ImageJ. F-actin OOP was calculated from phalloidin stain with a coherence threshold of 0.3 using a structure tensor method.[170] Cell thickness was calculated from deconvolved Z-stack images of F-actin from Imaris. Nuclear angle offset (θ) was calculated by manually tracing the outlines of nucleus and cell body in ImageJ and comparing orientation difference between the principle axes. Nuclear eccentricity was evaluated by fitting an ellipse to individually traced nucleus in ImageJ and calculating its eccentricity, defined as:

$$\text{e} = \sqrt{1 - \left(\frac{\text{minor axis length}}{\text{major axis length}}\right)^2} \tag{1}$$

Projected nuclear area was quantified by tracing the outline of the nucleus in ImageJ. Nuclear surface area and volume were evaluated by fitting an ellipsoid with half-length (a), half-width (b) and half-height (c) to each individual nucleus from deconvolved z-stack images in Imaris (Figure 2-11 A) with the following formulas:

$$V = \pi \frac{4}{3} abc \tag{2}$$

$$SA \approx 4\pi \left(\frac{a^p b^p + a^p c^p + b^p c^p}{3} \right)^{1/p}$$
(3)

where $p = 1.6075$. Cell shortening was calculated by summing the differences in cell length from DIC images of cell at basal and relaxed conditions (Figure 2-19 A). OOP, nuclear angle offset, eccentricity, projected area, surface area, and volume were quantified from between 7-12 images of isolated VSMCs for each AR. All results were compared using ANOVA on ranks test, with pairwise comparisons performed using the Tukey's test. All correlations analysis was evaluated using Pearson product moment analysis.

2.5.5 Cell, Patterned Fibronectin Island, F-actin and Nucleus Fluorescent Microscopy

Fixed and stained cells seeded on isotropically patterned FN were imaged on a line-scanning Zeiss LSM 5 LIVE confocal microscope (Carl Zeiss, Oberkochen, GER) with a 20x Plan-Apochromat objective at 1x zoom and laser excitations at 405 nm and 488 nm wavelengths to image the DAPI and DiO staining respectively. With the same microscope, stained micropatterned FN islands on PAA gel were imaged with a 20x Plan-Apochromat objective at 0.5x zoom and laser excitation at 633 nm wavelength. 2D and Z-stack images of phalloidin stained F-actin and DAPI stained nucleus were acquired with the Zeiss LSM 5 LIVE confocal microscopy with a 40x EC-Plan Neofluar lens oil objective with 1x zoom and laser excitations at 561 nm and 405 nm wavelength respectively. Z-stack images were subsequently deconvolved in Imaris (Bitplane Scientific Software).

2.5.6   Traction Force Microscopy Experiment

After 3 d of culture, micropatterned VSMCs on PAA gels were moved to an incubation chamber on a Zeiss LSM 5 LIVE confocal microscope maintained at 37ºC and immersed in Tyrode's solution (1.8 mM $CaCl_2$, 5 mM HEPES, 1 mM $MgCl_2$, 5.4 mM KCl, 135 mM NaCl, 0.33 mM NaH_2PO_4, adjusted to pH 7.4). After allowing the cells to equilibrate for 10 minutes in the incubation chamber, isolated VSMCs were imaged with a 40x EC Plan-Neofluar oil objective at 0.5x zoom on a Zeiss LSM 5 LIVE confocal microscope (Carl Zeiss, Oberkochen, GER) 3 times every 4 minutes with both bright field and 488 nm wavelength laser excitation to obtain images of VSMCs baseline contracting and displacing fluorescent beads in the gel substrate. Subsequently, the VSMCs were imaged 3 times every 4 minutes after stimulation with 100 nM ET-1 for 15 minutes, followed by 100 µM HA-1077 (Sigma-Aldrich, St. Louis, MO) for 15 minutes. During the stimulation, no images were taken to minimize the amount of photo-damage to cells. Immediately prior to cell detachment, cell nuclei were stained with DAPI and imaged to ensure that only single cells were analysed. At last, trypsin was added to detach the cells from the substrate. The experiment was terminated when the cell in the field of vide dissociated from the gel, thus leaving the gel with no surface traction.

2.5.7   Traction Force Microscopy Data Analysis

Displacement and traction stress vectors were calculated from the bead displacement as previously published [174]. Briefly, displacement of gel was determined by comparing the beads images at baseline, stimulated and relaxed states to the bead image when cells were detached from the substrate. The traction stress field was then

calculated from the displacement map using Fourier transform traction cytometry method. Traction stress vectors were discretized to a 10 x 10 μm^2 grid.

To calculate the total strain energy U transferred from the cell to the elastic distortion of the substrate, we applied the following equation as previously published [89]:

$$U = \frac{1}{2}\sum_n A_n(u_{x,n}T_{x,n} + u_{y,n}T_{y,n}) \tag{4}$$

where u_i and T_i represent displacement and traction force vectors in the i-direction; A is the discretized unit surface area of the cell body.

To calculate the total traction force cell T_i applied to the substrate in the i-direction, we summing the magnitudes of all traction force vectors $\vec{T}_{i,n}$ cell exerted on both sides and multiply by one half as previously published [89]:

$$T_i = \frac{1}{2}\sum_n A_n|\vec{T}_{i,n}| \tag{5}$$

assuming that cells exerted about equal magnitude of traction force at each sides.

To calculate the longitudinal cumulative cellular prestress P_x, we divided the total traction force in the longitudinal direction T_x by the averaged cross-sectional area of the cells.

Isolated VSMC AR was calculated in ImageJ by tracing the cell outline from a DIC image taken at baseline. VSMCs that responded to ET-1 stimulation with significantly elevated strain energy were selected for correlation analysis. All correlations analysis was evaluated using Pearson product moment analysis.

3 Engineering Vascularized Network in Folded, Porous Polymer Matrices by Tissue Origami

Organ function relies on hierarchical organization within tissues from single cells (~10 µm) to functional subunit (100 µm – 1 mm). Traditional tissue engineering scaffolds typically use a porous structure made of synthetic or natural polymer, which provide little control in organizing cells into three-dimensional structures. The lack of cellular architecture contributes to suboptimal tissue function. We present a simple and versatile scaffold folding strategy, Tissue Origami, which allows organization of multiple cell populations within three-dimensional, porous, synthetic and natural polymer matrices. We demonstrated that individual layer of porous, sub-millimeter thickness poly(lactic-co-glycolic) acid and collagen films patterned with multiple cell populations can be folded in Miura-ori geometry to produce different three-dimensional cellular organization within the engineered construct. We found patterned cells were healthy and viable in the folded construct and were metabolically active 3 days after seeding. In a proof-of-concept study, we patterned endothelial and smooth muscle cells with different three-dimensional configurations in the folded constructs to build vascularized network and compare them to the traditional bulk, porous polymer matrices. We quantified the number of blood vessels formed within each construct systematically and found that the folded constructs seeded with endothelial cells and vascular smooth muscle cells adjacent to each other laterally in the same folding plane created the densest vascularized network. This technique may enable development of organized vascular tissues that closer mimic native tissues and improve the function of engineered tissues.

3.1   Introduction

Tissue engineered construct is typically assembled through the combination of cells and biomaterials in hope that it would replace damaged or diseased organs. Traditional porous polymer scaffold are designed to support the attachment and proliferation of cells, in order for them to recapitulate lost tissue functions [213]. These cells are influenced not only by autonomous programs but also by their cellular micro-environment, which include interaction with neighboring cells, biochemical factors and physical forces. The collective effect of these factors depends on the hierarchical organization among the tissue construct. However, due to lack of control over cell seeding process in three-dimensional polymer matrices, the resultant tissue engineered construct has little organization to its tissue architecture. In contrast, tissues in native environment consist of highly organized smaller repeating unit on the scale of hundreds of microns (e.g. muscle tissue, islet, nephron) that interacts with neighboring cells and performance specific functions [214]. This difference in microarchitecture leads to suboptimal functions for tissue engineered construct and hindered the advancement of this field in achieving clinically relevant organ replacement products.

Over the last decade, a number of promising techniques have emerged to address the lack of control in cellular organization for tissue engineered constructs. Several of these techniques has demonstrated the ability to produce tissue constructs with cellular organizations including 3D inkjet bioprinting [215, 216], layer-by-layer cell sheet stacking [217, 218], spheroid self-assembly [215] and laser guided direct writing [219]. These techniques largely rely on recent advancement in rapid prototyping technology to assemble miniaturized modular units with different cell types to achieve structure

organization within tissues. Although these techniques successfully patterned cells in 3D to a varying extent, there is some critical drawback associated with them that prohibited wide adoption of these techniques in clinically settings. For example, the 3D inkjet printing technique is restricted to using only hydrogel as cell carrier, tissue spheroid technique requires specialized equipment, and cell sheet stacking and laser guided direct writing have low throughput due to lengthy operations.

We developed a strategy to engineer vascularized networks in three-dimensional, porous, polymer matrices by folding synthetic and natural polymer films with patterned vascular cells. We fabricated poly(lactic-co-glycolic) acid (PLGA) and collagen thin films and folded them into Miura-ori geometry along laser-etched perforated lines. We patterned human endothelial cells (ECs) and vascular smooth muscle cells (VSMCs) on thin films by loading them onto acrylic posts of a stamping system and subsequently inverting the posts to transfer the cell suspensions at pre-defined locations on the films. The patterned cells were viable in the folded polymer matrices 3 days after seeding. We built vascularized networks by patterning ECs and VSMCs in different three-dimensional organizations in the folded polymer matrices and found that organization with patterned ECs and VSMCs on the same folding plane had a significantly higher vessel density compared to the folded configuration that homogenously mixed the two cell types. These findings suggest that three-dimensional organized structure of vascular cells may lead improved vascularization potential in porous polymer matrices.

3.2   Results

3.2.1   Fabrication and Visualization of Thin, Porous PLGA film

We hypothesized that thin and porous films can facilitate the manual folding process and increase nutrient transport for cell survival within the construct. We adapted published solvent casting and porogen leaching methods to fabricate the PLGA film (Figure 3-1 A). Briefly, a glass plate enclosed by 4 glass slides near the edges formed a well for the solvent cast. Since PLGA film adhered strongly to glass (data not shown), we pre-coated our glass plate with 2% w/v alginate solution as a sacrificial layer that facilitates the removal of PLGA film at a later time. Sugar particles that were sieved between 90 to 106 μm served as porogen for creating a porous architecture. The amount of sugar particles was calculated to produce a 90% porous structure after leaching. Immediately after adding the sugar particles to the 5% w/v PLGA in chloroform solution, the mixture was casted into the well coated with alginate to uniformly spread the sugar particle. When the chloroform solution evaporated from the casted mixture, the entire construct was placed in a desiccator overnight to completely remove any residue solvent. The PLGA thin film was obtained by placing the construct in DiH_2O for 4 hours to dissolve the embedded sugar particles and the alginate thin film, allowing the PLGA film to float to the surface.

The dried PLGA film was flexible and uniform, with no structural defect (Figure 3-1 B). Due to the highly porous nature of the film, it appeared to be translucent. The thickness of the PLGA film was 280 ± 20 μm (mean±SD), suggesting that the film contains, 2-3 layers of sugar particles prior to water leaching on average. Scanning electron microscopy (SEM) images showed a highly porous and interconnected micro-structure, with some large pores passing through the entire film (Figure 3-1 C). Higher magnification images demonstrated that in addition to large pores around the size of

86

sugar porogen, pores between 100 nm and 3 µm are also scattered throughout the film structure (Figure 3-1 D-E). Taken together, we created a highly porous, reproducible, flexible PLGA thin film with sub-millimeter thickness.
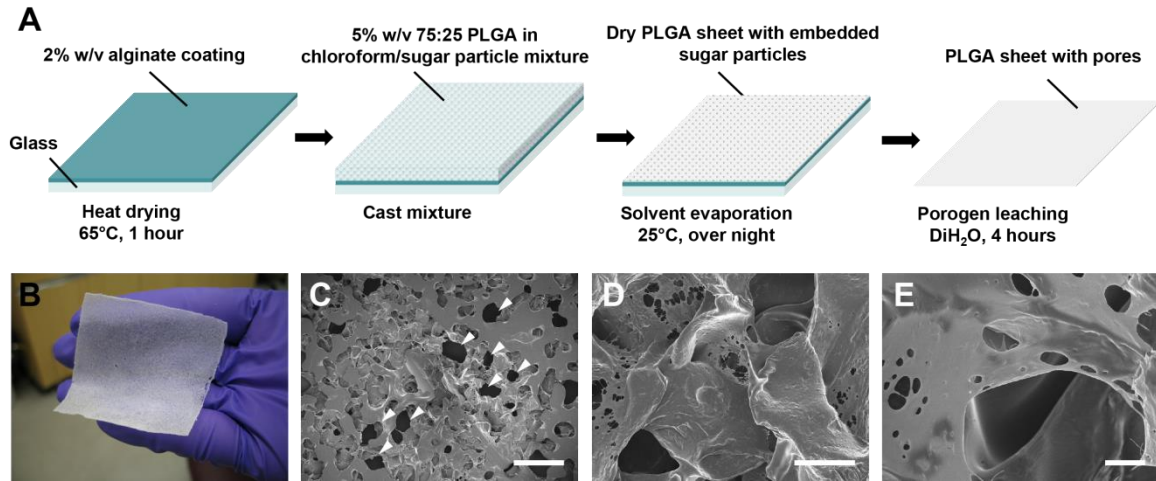
Figure 3-1: PLGA film fabrication and visualization. (A) PLGA (75:25) porous and thin film was fabricated by using solvent casting and porogen leaching method. (B) Flexible, translucent PLGA porous thin film obtained with an average film thickness of 280 ± 20 µm (mean $\pm$ SD). SEM image of porous PLGA thin film viewed under low (C), med (D) and high (E) magnifications. The scale bars in (C-E) are 500, 50 and 5 µm respectively. Some pores penetrated all the way through the scaffold as evident in (C, white arrowheads).

3.2.2   Fabrication and Visualization of Thin, Porous Collagen Film

Since collagen is not dissolvable in organic solvent, we modified the protocol from a published patent and fabricated the collagen thin film through a freeze-drying method (Figure 3-2 A) [220]. Briefly, we dissolved the collagen powder in 0.05 M glacial acetic acid and blended the mixture with a commercial blender to obtain a uniform

mixture of slurry. After deforming the mixture by centrifugation, the collagen slurry was sandwiched between two glass plates enclosed with four Teflon tape spacers and froze in -20°C freezer. After transferring the construct to the -80°C freezer for an additional 24 hours, the construct was lyophilized for 48 hours, leaving only the porous thin film behind. The finished collagen film is flexible and thin, with a white appearance (Figure 3-2 B). We measured the thickness of the film to be 286 ± 14 µm (mean ± SD), suggesting that the inter-batch thickness variation is minimal. We examined the microstructure of the film via SEM and found a highly porous architecture with similarly sized pores (Figure 3-2 C). High magnification images showed no nano-sized pores as seen in the PLGA thin film (Figure 3-2 D-E).
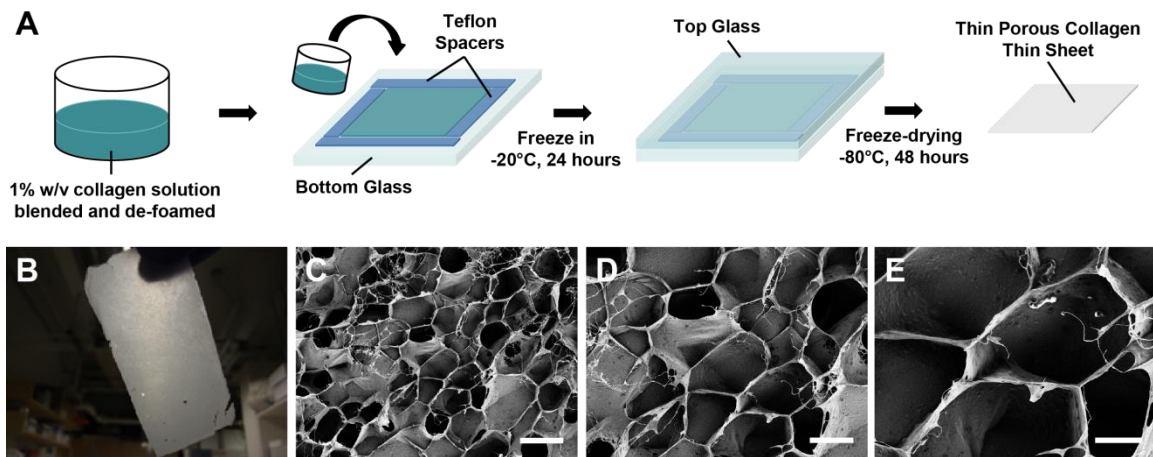
Figure 3-2: Collagen film fabrication and visualization. (A) Porous, thin collagen film was made by freeze-drying blended collagen slurry. (B) Collagen thin film obtained with an average film thickness of 286 ± 14 µm (mean ± SD). SEM image of porous PLGA thin film viewed under low (C), med (D) and high (E) magnifications. The scale bars in (C-E) are 200, 100 and 50 µm respectively.

Since collagen can be degraded by enzymes such as collagenase and pepsin *in vivo*, we characterized the degradation behavior of the fabricated collagen thin film by calculating the weight remained (w_r) in phosphate-buffered saline (PBS) with and without collagenase as a fraction of initial weight (w_0) after specific time periods. We found that in PBS without the collagenase, the weight fraction (w_r/w_0) dropped significantly after 24 hours but remained similar thereafter until the end of the experiment 7 days later (Figure 3-3). However, degradation of collagen thin sheet was significantly faster in PBS containing collagenase at 100 μg/mL. At the end of the experiment 2 hours later, only 40% of the initial weight remained and the weight-time function was approximately linear (Figure 3-3). Taken together, the degradation profile of collagen thin film suggests that long term culture of cells that are capable of degrading collagen may compromise the structural integrity of the thin film and cross-linking of the collagen may be required prior to long term cell culture.
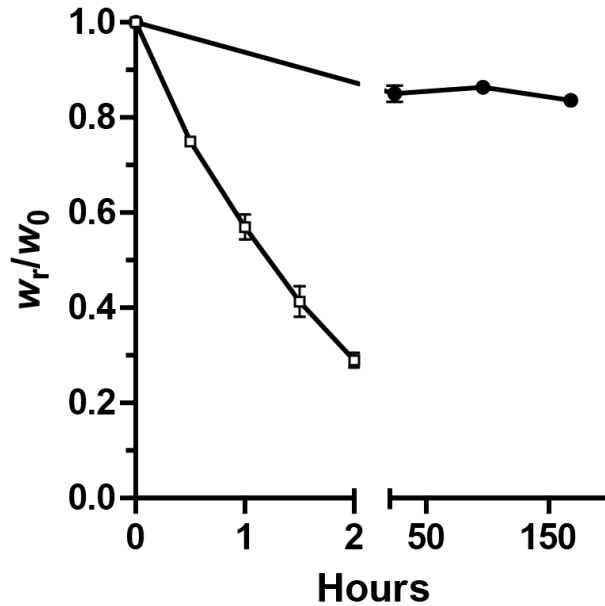
Figure 3-3: Degradation profiles of collagen thin film in PBS and collagenase. The weight fractions were calculated as the ratio between the weight remained (w_r) after immersing in PBS with (—▫—) or without (—•—) collagenase at 100 µg/mL at 37°C to the initial weight of the thin films (w_0). The degradation behavior in collagenase can be approximated linearly with the equation: $w_r/w_0 = -8.33 \times 10^{-5}t + 0.949$ with $R^2 =$ 0.976. Data ± SEM. $n = 3$ for each condition.

3.2.3 Folding Thin Film into Miura-geometry with Laser-etched Perforated Lines

We selected the Miura-geometry invented by Japanese astrophysicists Koryo Miura to fold our thin film construct because this particular geometry allows for packing of the thin sheet into a very compact area with its thickness restricted only by the thickness of the thin sheet itself. To improve the fidelity and reproducibility of manual folding, we designed the folding lines of the Miura-geometry in a computer-aided design

(CAD) program and laser-etched periodical perforations along the design on porous

PLGA (Figure 3-4 A) and collagen (Figure 3-4 B) thin sheet prior to folding. The outer

boundary of the Miura-geometry was produced by using higher laser power to completely

sever the thin film. The etched lines allow for folding of PLGA (Figure 3-4 C) and

collagen (Figure 3-4 D) thin films easily and subsequent retaining of folded geometries

without external constrains. This approach allowed us to fold PLGA and collagen thin

sheet into Miura-geometry manually easily and precisely.
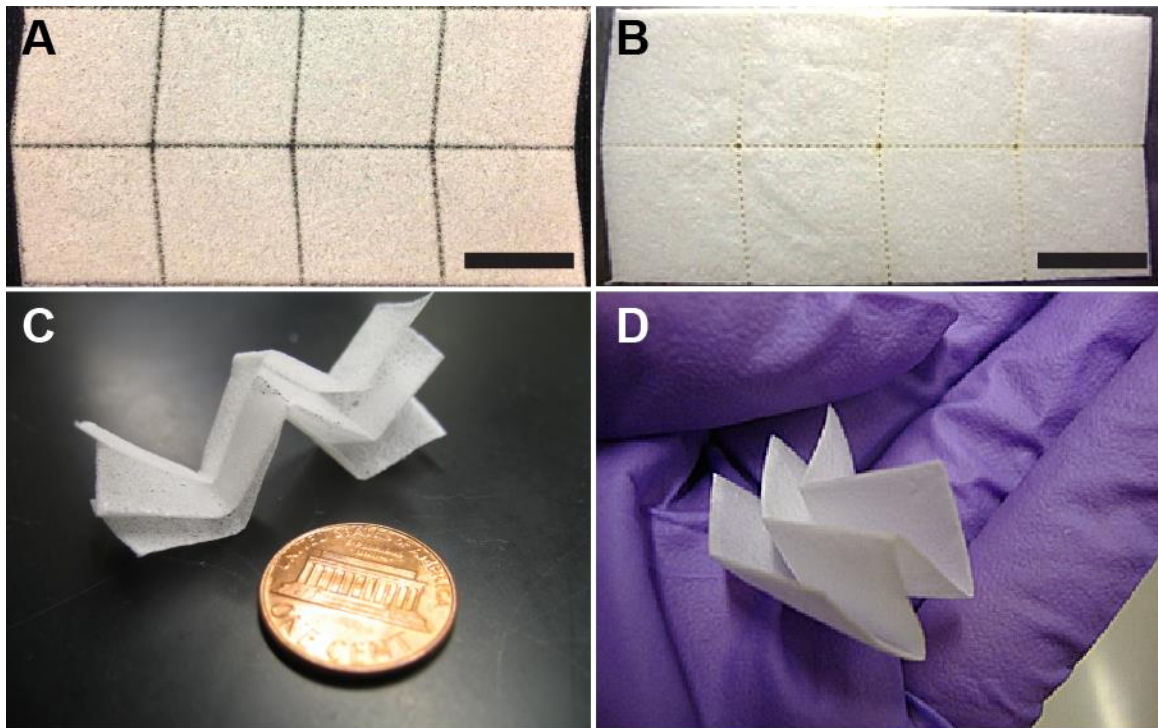
Figure 3-4: Folding of laser-etched PLGA and collagen thin film into the Miura-ori geometry. PLGA (A) and collagen (B) thin films with an 8-facet Miura-geometry. The perforated folding lines were laser-etched from a user-designed CAD drawing. 3D 16-facet PLGA (C) and 8-facet collagen (D) folded constructs were obtained by manually folding along the perforated lines. (A-B) scale bars = 1 cm.

3.2.4   Patterning of Thin Films with Post-stamping System

We developed a two parts post-stamping system to pattern the thin films at user-defined locations with liquid droplets (Figure 3-5 A). Prior to patterning the film, liquid droplets were loaded onto each individual acrylic posts on the stamping system. The posts with liquid droplets were then inverted upside down and pressed gently to allow the liquid droplets to transfer into the thin film.

The top part is made of acrylic plate with small acrylic posts of equal height fixed at various locations (Figure 3-5 B). The acrylic posts were fabricated by cutting out circular holes on a 1/8" thickness acrylic plate with laser at high power. The locations of the acrylic posts were designed in a CAD drawing such that the pattern these posts created on a two-dimensional thin sheet aligns along the z-axis when the film folds into the three-dimensional Miura-ori geometry. Low power laser was used to lightly mark the locations on the acrylic top plate and premade acrylic posts were subsequently glued at these locations.

The bottom part is made of two $^1/_8$" thickness acrylic plates glued together where one plate had the center region shaped of the outer boundary of 2D Miura-geometry completely removed by laser (Figure 3-5 C). This hollowed center region served as the loading location for the thin film that needs to be patterned. Four 1" screws were machined into the four corners of the bottom part with the corresponding screw holes on the top part to fix the xy-plane position during the patterning process. When the top and bottom parts are assembled, four nuts were used to equalize and stabilize the downward pressure exerted on the enclosed thin film by the acrylic posts (Figure 3-5 D).

We stamped green and red liquid food coloring droplets on PLGA thin films to produce the alternating coloring pattern (Figure 3-5 E). We found that the patterned shape of the liquid droplet was not circular of the post and there was liquid bleeding underneath the film (Figure 3-5 F).
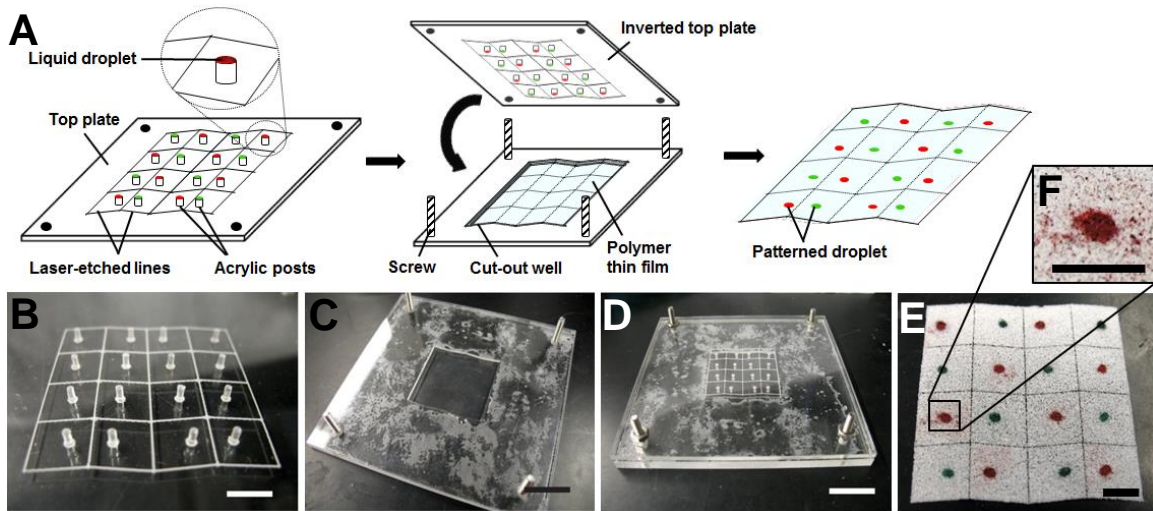
Figure 3-5: Patterning PLGA thin films with post-stamping system. (A) Schematics illustrating the stamping process. (B) The top part is composed of acrylic posts bonded to a base acrylic plate at specific locations in the faces of the Miura-geometry such that the patterned locations aligns vertically in the z-axis of the folded thin film. Scale bar = 1 cm. (C) The base part is created by bonding two acrylic plates together with the center region of one of the plates pre-cut in the shape of the Miura-geometry. The translucent regions were the dried adhesive. Four screws are machined into the bottom part at the four corners. Scale bar = 3 cm. (D) Assembled top and bottom parts with four nuts to secure the stamping system. Scale bar = 3 cm. (E) Two different colored liquid droplets were loaded on the posts to produce the alternating pattern in PLGA thin film. Scale bar = 1 cm. (F) Patterned droplet had a non-circular shape and liquid bleeding underneath the film were visible. Scale bar = 1cm.

93

To address this issue, we controlled the liquid spreading pattern in the thin film by creating circular laser-etched boundaries in the thin film at the stamping locations of liquid droplet (Figure 3-6 A). The boundaries served as a physical barrier preventing the liquid from spreading beyond the etched region into the main body of the thin film. However, when an excessive laser power was used, the etched center region detached from the thin film, leaving a hole behind (Figure 3-6 A, black arrowheads). With different food coloring diluted in DiH_2O, we created circular liquid dots of different sizes simultaneously in the PLGA thin films (Figure 3-6 B). By designing different post and color loading configurations, we created two patterns in the film: alternating colors of same-sized dots along the *z*-axis (Figure 3-6 C) and different-sized dots on the same *xy*-plane (Figure 3-6 D). As a result of the physical boundary, the resolution of circular dots increased to about 1 mm in diameter. Immediately after liquid droplet stamping, the film was folded along the laser-etched perforated lines into the 3D Miura-geometry construct.

We evaluated the efficiency of the post-stamping system in patterning collagen thin films. 3µL of food coloring droplets containing 1% w/v gelatin/DiH_2O were individually dispensed on the posts before brought into contact with the collagen thin film (Figure 3-7 A: top view, Figure 3-7 B: side view). Although most of the liquid dots were constricted within the physical boundaries, in some cases, the droplet was able to wet into the main body of the thin film, leaving a blot extending beyond the physical boundary (Figure 3-7 C). We suspected that this may be due to increased hydrophilicity of collagen.The patterned collagen thin film folded easily into the final 3D Miura-geometry construct (Figure 3-7 D). Taken together, the post-stamping system combined

with the laser-etched boundary allow for simultaneous patterning of different sized liquid

dots on PLGA and collagen thin films at user-defined locations.
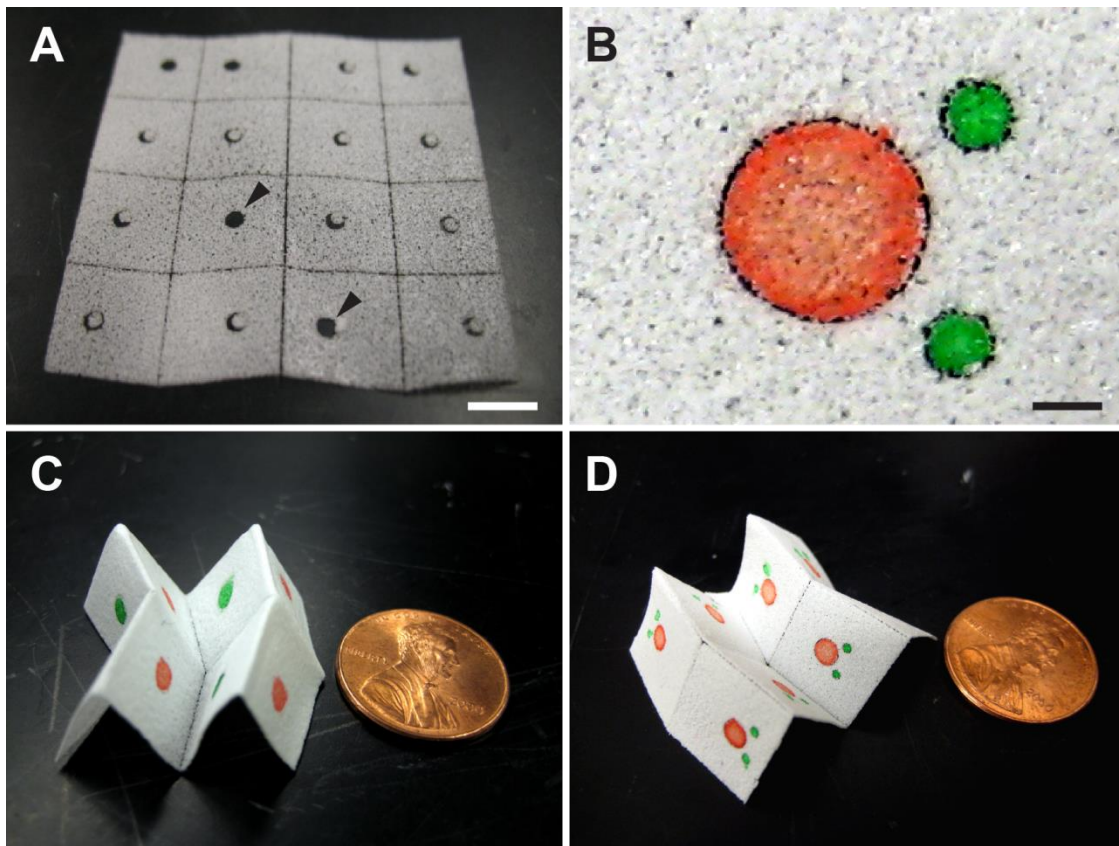
Figure 3-6: Laser-etched circular boundaries improved patterning fidelity and consistency in PLGA thin films. (A) Laser-etched circular boundaries in a PLGA thin film. Excessive laser power could sever the patterned region, leaving only holes on the thin film (black arrowhead). Scale bar = 1 cm. (B) Red and green coloring dots in DiH_2O enclosed with different sizes of laser-etched boundaries. The large dot was created with 3 µL of stamping volume while the smaller dots was created with 1.5 µL. Scale bar = 1 mm. (C) Alternating colors of same sized dots along the *z*-axis of a 8-facet semi-folded Miura-geometry PLGA construct. (D) Different sized dots could be simultaneously stamped on the same *xy*-plane of a 8-facet semi-folded PLGA construct.
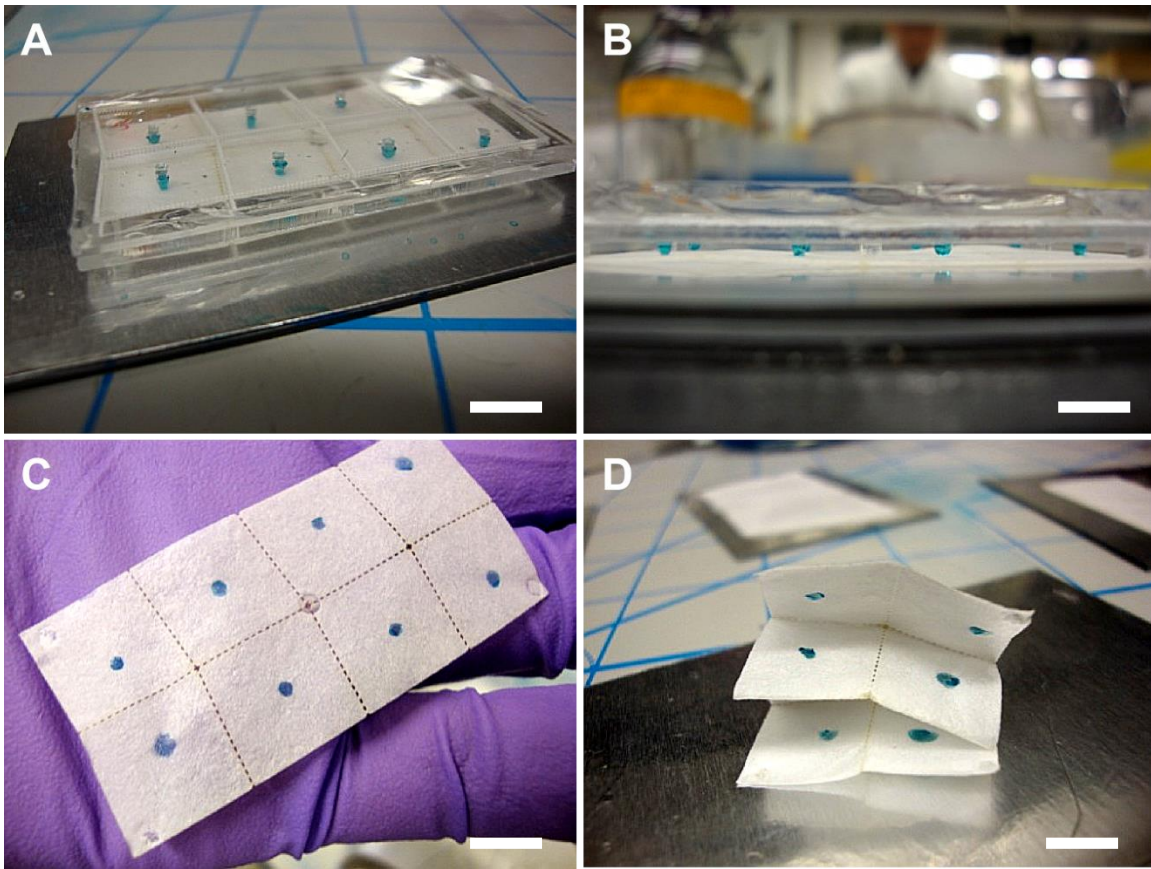
Figure 3-7: Laser-etched boundaries were ineffective for patterning in collagen thin film. Top view (A) and side view (B) of an inverted post-stamping system loaded with blue food coloring droplets in 1% w/v gelatin/DiH$_2$O. (C) Collagen thin film after post-stamping. There was liquid bleeding outside of the laser-etched boundaries, possibly due to hydrophilic wicking effect of collagen. (D) Semi-folded collagen thin film with the patterned area aligning along the *z*-axis. (A-D) Scale bars = 1 cm.

3.2.5 Three-dimensional Cell Patterning in Folded, Porous Polymer Matrices

In order to pattern cells in the thin films, we suspended cell in a mixture of media and Matrigel as previously described [221]. Since Matrigel retains its fluidity at 4°C but polymerize into a gel at 37°C, we prepared the cell mixture with cold media and

Matrigel at 4°C and incubated the patterned cell suspension at 37°C to allow Matrigel to encapsulate the stamped cells at patterned locations. To inspect the fidelity of cell pattern, we stained two cell populations with membrane dyes DiI and DiO that excite at 549 nm and 484 nm respectively. We tested different patterns for PLGA and collagen thin films. For PLGA thin film, we loaded the cell suspensions on 4 posts configured in an equilateral triangle such that the three vertices are stamped with the DiI-stained cells while the centroid of the triangle is stamped with the DiO-stained cells (Figure 3-8 A). For collagen thin film, we loaded cells stained with the same membrane dye on the opposing corners of a square.

We found patterned cell populations retained its circular shape and relative positions to each other 2 hours after the stamping in a 2-facet folded PLGA construct (Figure 3-8 B). Stamping was completed with high fidelity as there was little defect in the shape and DAPI-stained nuclei were presented throughout the stamping area and within the laser-etched boundaries. However, in 2-facet folded collagen construct, the patterned cell populations were not as uniform as the PLGA thin film within the boundaries and there were signs of wicking in between the boundaries (Figure 3-8 C). Taken together, these data demonstrated that patterning of multiple cell populations simultaneously on PLGA and collagen thin films can be achieved using post-stamping system with Matrigel as a cell suspension carrier. However, further improvement need to be made to collagen thin films to achieve higher fidelity.
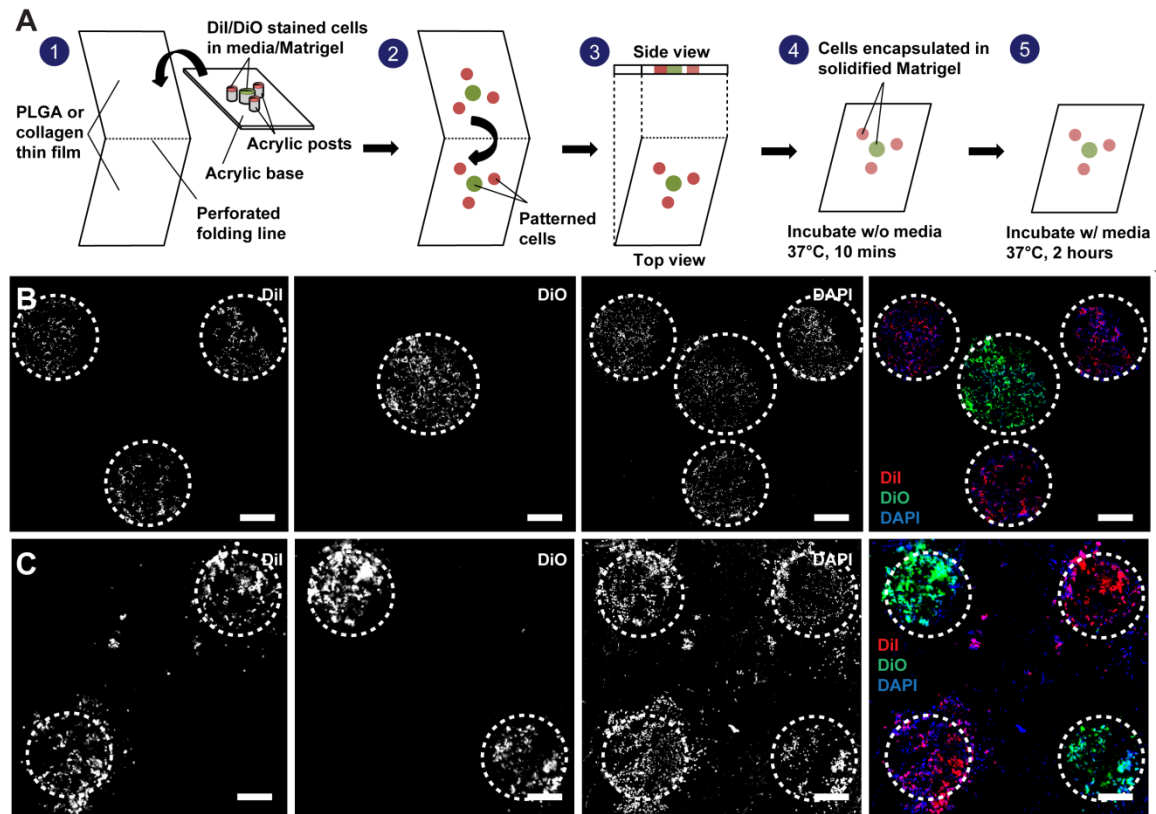
Figure 3-8: Patterning cells in PLGA and collagen thin films using post-stamping system. (A) Human endothelial cells stained with DiI and DiO were suspended in 1:1 v/v media/Matrigel and loaded onto posts before brought into the contact with the thin films. Matrigel was allowed to gel at 37°C to encapsulate the patterned the cells before media was supplied to the folded constructs. (B) Immunofluorescent confocal images of DiI and DiO stained cells with DAPI counterstain near the center of a folded, two-facet folded, porous PLGA matrices 2 hours after stamping. The stamping pattern is an equilateral triangle with its three vertices stamped with cells stained with DiI and its centroid stamped with cells stained with DiO. (C) Immunofluorescent confocal images of DiI and DiO stained cells with DAPI counterstain in a folded, two-facet folded, porous collagen matrices 2 hours after stamping. The stamping pattern is a square with the opposing

Figure 3-8 (Continued) vertices stamped with cells stained with the same membrane dye. (B-C): Dashed lines indicate laser-etched boundaries for stamping. Scale bars = 500 µm.

3.2.6   Patterned Cell Viability in Folded, Porous PLGA Matrices

We asked if the patterned cells are viable in the folded PLGA construct. We qualitatively evaluated the viability of human endothelial cells (EC) 2 hours after patterning with live/dead cell viability assay. We found that most of the cells in the patterned region were live (Figure 3-9 A) with minimal number of dead cells (Figure 3-9 B). There were no cells found in yellow, indicating an absence of active cellular apoptosis (Figure 3-9 C). For longer culture period, we quantitatively evaluated the viability of human ECs and VSMCs in bulk porous PLGA matrices (B_p) and 4-facet folded 3D PLGA constructs (Figure 3-9 D) using alamarBlue assay. The three-dimensional cellular organization of folded construct were divided into three categories: (F_s) folded PLGA matrices patterned with only ECs, VSMCs or a homogenously mixed population of ECs and VSMCs, (F_z) folded PLGA matrices patterned with alternating EC and VSMC populations along the z-axis and (F_{xy}) folded PLGA matrices patterned with both EC and VSMC populations on each facet in the same xy-folding plane arranged as shown (Figure 3-9 D). Each facet of the fold was stamped with 3×10^5 cells for a total of 1.2 million cells per construct. After 3 days of culture, we found that the metabolic activities indicated by the fluorescent readings for all conditions were similar for different three-dimensional cellular organizations (Figure 3-9 E), suggesting a comparable level of live cells for all organizations. Taken together, these results suggest that the cells

patterned in the folded PLGA matrices were able to survive after 3 days of culture *in vitro.*
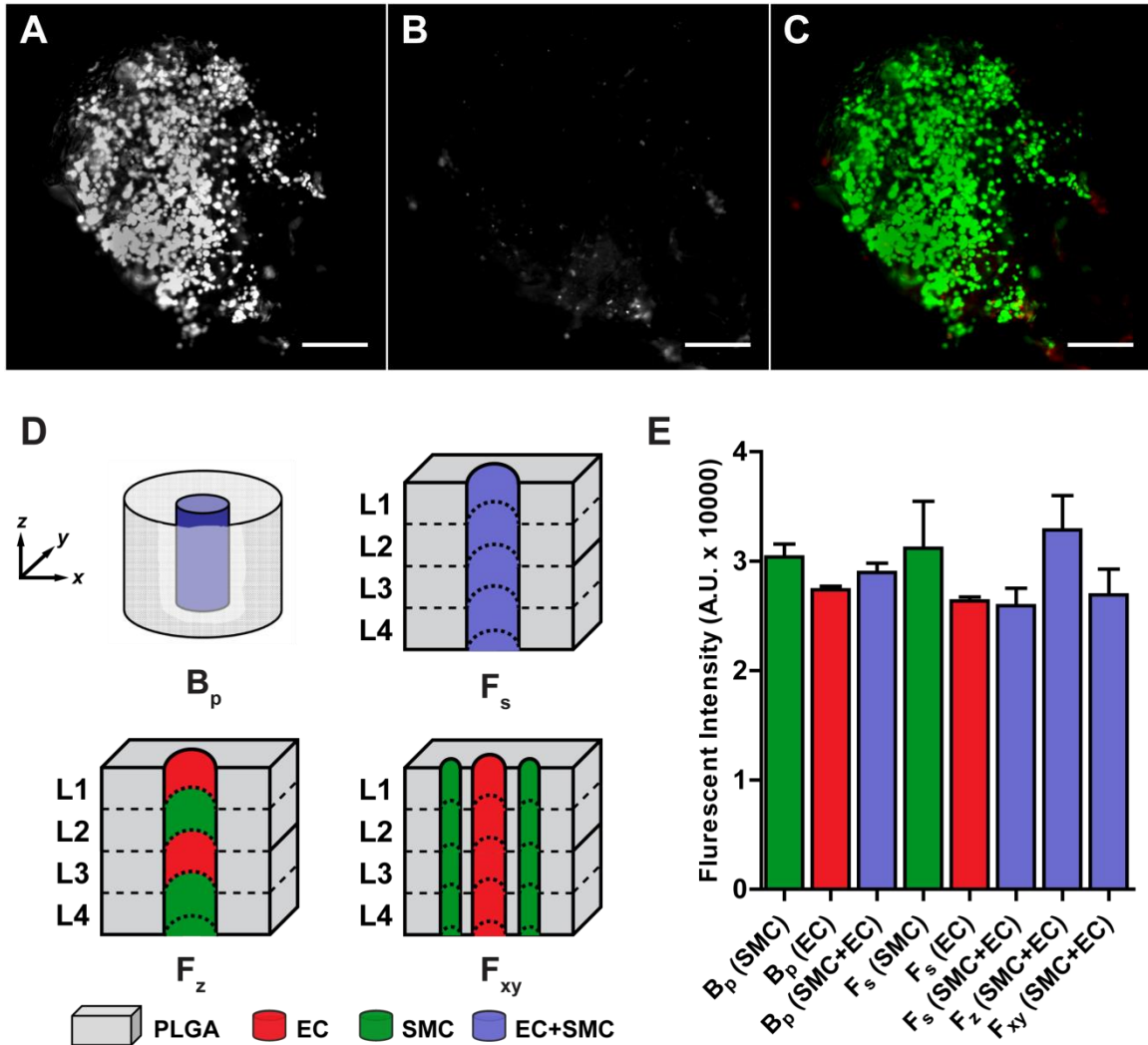
Figure 3-9: Cell viability evaluation in folded and bulk porous PLGA polymer matrices. Fluorescent images of live (A) and dead (B) human endothelial cells stained with calcium AM and ethidium homodimer-1, respectively, in a 4-facet folded PLGA tissue construct. (C) Composite image of live and dead cells in (A) and (B). (A-C) Scale bars = 300 μm. Live: green. Dead: red. (D) Three-dimensional cross-sectional schematic representations of cellular organizations with ECs, VSMCs, or homogeneously mixed population of ECs and VSMCs in bulk, porous PLGA matrices (B_p) and 4-facet folded

Figure 3-9 (Continued) 3D PLGA matrices (F_s, F_z and F_{xy}) for metabolic assay. L1-L4 are folded facet of the polymer matrices. (E) Fluorescent readings as a result of the metabolic activities of seeded and patterned cells in bulk and folded PLGA constructs with background reading subtracted. Data ± SEM. $n = 3$ for each condition.

3.2.7 Organized Three-dimensional Organization Promotes Vascularized Network Formation

Angiogenesis in native environment requires EC and VSMC work in concert spatiotemporally [222-224]. We asked if organized three-dimensional structures of EC and VSMC populations patterned in folded PLGA constructs improve vascularized network formation *in vivo*. To that ends, we subcutaneously implanted EC and SMC organized in porous PLGA matrices with B_p, F_s, F_z and F_{xy} configurations on the dorsal regions of SCID/bg male mice (Figure 3-10 A). After 2 weeks, the constructs were explanted (Figure 3-10 B), imbedded in paraffin, sectioned and immunostained for blood vessels.

We followed a systematic approach in quantifying the vessel density by imaging 36 fields of views for each stained section (Figure 3-10 C). Immunostained blood vessels of various sizes were found in the bulk porous scaffold and folded constructs (Figure 3-10 D) with perfused red blood cells visible in some vessels (Figure 3-10 E). We manually counted the number of human-caldemons positive blood vessels from the images and normalized by the field of view surface area. We found a significantly higher blood vessel density in the folded construct with F_{xy} configuration compared to folded constructs with F_s configuration (Figure 3-10 F), suggesting that organized three-

dimensional structures of ECs and VSMCs in PLGA matrices can improve the formation of mature blood vessels.
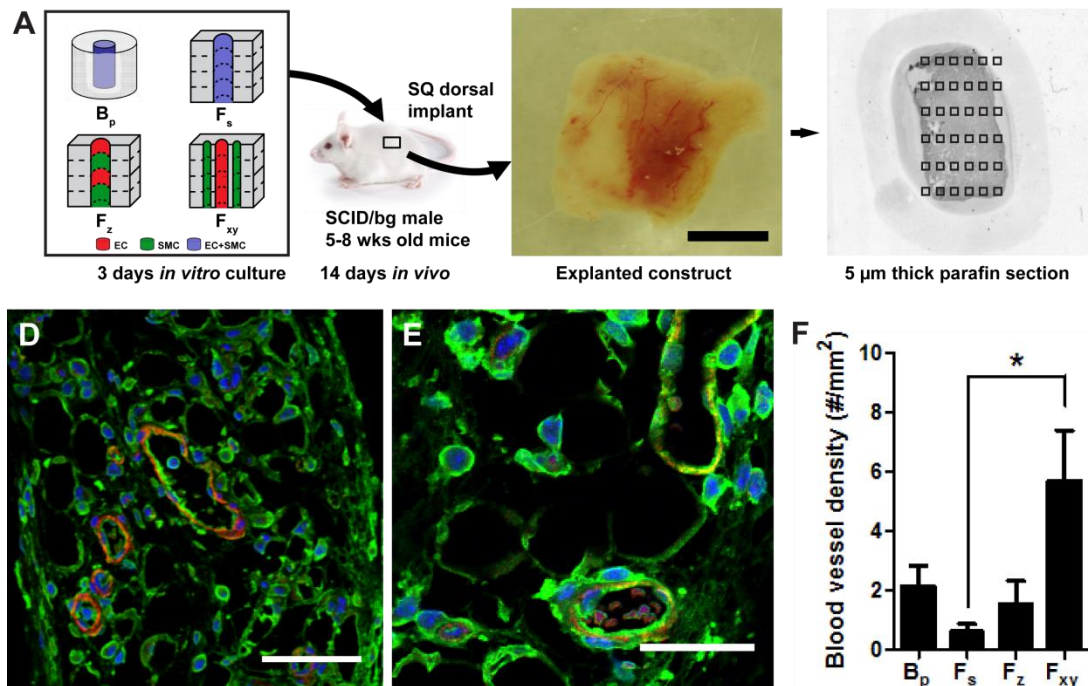
Figure 3-10: Evaluating vascularization network formation in folded and bulk porous PLGA matrices. (A) PLGA bulk porous scaffold (B_p), 4-facet folded construct in Miura geometry with homogenously mixed human EC and SMC populations (F_s), with alternating EC and VSMC populations in the *z*-axis of the construct (F_z), and with both EC and VSMC populations on the same *xy*-plane of each facet of the construct arranged as shown (F_{xy}) were cultured for 3 days *in vitro* prior to subcutaneous dorsal implantation in SCID/bg male mice. (B) An example of explanted folded scaffold after 14 days of *in vivo* implantation. Scale bar = 5 mm. (C) Each sectioned paraffin slide was systematically divided into a grid of 6 x 6 field of views (black squares, not to scale) and imaged. (D) Representative immunohistochemical staining of blood vessels on a sectioned slide. (E) Representative staining of perfused blood vessels with red blood cells. (D-E): (Green: anti-human CD31, Red: anti-human Caldesmon, Blue: DAPI). Scale bars

Figure 3-10 (Continued) = 50 µm. (F) Human Caldesmon positive vessel density found for different three-dimensional organizations. Mean ± SEM. $n = 3$ explants.

3.3 Discussion

In this study, we developed a novel 3D cell patterning method, Tissue Origami, to organize multiple cell populations in 3D synthetic and natural polymer scaffolds by folding cell-laden 2D polymer thin films with Miura-geometry. We found cell populations could be patterned simultaneously with sub-millimeter resolution and maintained metabolically within the constructs. This is particularly relevant to the field of tissue engineering where cell organization in 3D scaffold could lead to improved function of the engineered tissue [225]. Although a number of strategies to address this issue have been reported in the past two decades, a large number of these studies rely on hydrogel as cell carrier and scaffolding material, which exclude a wide range of cell-compatible scaffolding materials such as PLGA and collagen. For strategies that do not use hydrogel, throughput and cost are prohibitive for clinically-relevant applications [226]. Our strategy does not suffer from the shortcomings of the previous techniques and can be adopted for a wide range of tissue engineering applications where specific material properties are required as scaffolds.

Our strategy offers several advantages compared to traditionally stacking or layering strategy to build 3D tissue engineering constructs. For example, Derda and colleagues built a 3D tissue engineered construct by assembling multiple layers of chromatography paper spotted with cell suspension [227]. While the authors

demonstrated the biocompatibility of the paper as a scaffolding material that supported cell survival and growth, the paper itself cannot be degraded as an implantable material and is not FDA approved. While its wide commercial availability is certainly advantageous, it is disadvantageous from a material-processing perspective because it is pre-made, which makes it difficult to modify its material properties such as porosity and mechanical strength. In another study, Shimizu and colleagues stacked multiple layers of cardiomyocytes cultured separately to achieve a 3D tissue engineered construct [218]. Although this strategy also enabled investigators to create user-defined cell patterns in 3D, it significantly adds handling time and operator-variability compared to Tissue Origami strategy where the locations of patterns are mathematically defined in all three axes as a result of pre-determined folding lines specified in Miura-geometry.

Angiogenesis is a complex process involving multiple cell types including ECs and VSMCs. Much of what we known currently about it came from the field of cancer biology where inhibition of this process may slow tumor growth and reduce the chance for metastasis [228]. In contrast, in tissue engineering, the challenge is to promote this process so that seeded cells in engineered scaffold have sufficient nutrients to survive. While it is commonly known that the EC and VSMC interacts with one another through cytokine signaling and physical contact [224], controlling angiogenesis is not a trivial pursuit for tissue engineering application due to the spatiotemporal requirements to regulate the complex process. A number of studies demonstrated a multi-cell type strategies can lead to improved formation of blood vessels in engineered scaffold [229-231]. However, most of these studies did not provide any organizational cues in the scaffold and relied on seeded cells to self-assemble into blood vessels. Our findings that

104

folded 3D constructs with homogeneously mixed populations of ECs and VSMCs showed significantly lower blood vessel formation than patterned EC and VSMC populations stamped on each facet suggest that spatially organizing populations of ECs and VSMCs may lead to higher blood vessel formation in the scaffold.

In summary, we designed a new 3D cell patterning strategy based on folding thin, porous polymer films with Miura-geometry, built PLGA and collagen thin films with perforated folding lines that allows two distinct populations of cells to be simultaneously patterned in 3D and tested this strategy in building vascularized networks with ECs and VSMCs. We found that initial configuration that placed EC and VSMC populations on the same plane of each facet led to the greatest yield in terms of the blood vessel formation. This technique is particularly relevant to the field of tissue engineering where spatial organization of multiple cell populations can lead to improved tissue functions. The wide range of material compatibility, low cost and high-throughput enabled by method can facilitate its adoption in manufacturing of clinically-relevant sized tissue engineered construct.

3.4   Experimental Challenges

There were a number of challenges pertaining to the development of this method. The first challenge was to develop a foldable scaffold that is biocompatible and biodegradable. With solvent-casting method, we were able to obtain nonporous, thin PLGA films that permitted folding. However, we found that due to the elasticity of the film, the folded construct tended to unfold its 3D shape and revert back to an open film over time. In addition, we were concerned about the nutrient diffusion through the

105

nonporous film to support cell survival and growth. To overcome these issues, we introduced an additional porogen-leaching step in the fabrication process and the resulting film became over 90% porous. The reduced density in the film greatly relieved the amount of mechanical stress experienced at the folding lines and the folded construct were able to remain in its folded shape indefinitely. The inter-connected porous structure also facilitates nutrient diffusion into the folded constructs. The folding process was later further improved with the incorporation of laser-etched perforated folding lines, which enhanced the accuracy and reproducibility of the manual folding.

The second major challenge was to develop a method to pattern multiple cell populations on the thin film simultaneously in a high-throughput and low-cost manner. Since PLGA is relatively hydrophobic, our initial attempt to deposit cell suspensions proven to be difficult as the small volume of cell suspension droplet tended to adhere to the hydrophilic surface that is used to transfer the droplet (e.g. pipette tips) rather than the PLGA thin film. To overcome this challenge, we increased the viscosity of the cell suspension droplet by adding Matrigel to the media and constructed the post-stamping stamping system to facilitate the transfer of the droplet to the PLGA thin film. The droplets were pre-loaded onto the acrylic posts of the post-stamping systems, which are also hydrophobic. The droplets adhere to the post initially due to surface tension. However, when inverted and in contact with the PLGA surface, the droplets prefer the PLGA film than the posts and allowed the cell suspension to be stamped on the thin films. Since virtually any post- and cell-loading configurations can be designed in a CAD drawing, it enables any cell patterns to be created simultaneously in the thin films in a high-throughput and low cost manner. The patterning process was further improved with

the assistance of laser-etched boundary to control the spreading of the deposited cell

suspension in the thin film laterally.

3.5   Materials and Methods

3.5.1   Preparation and Fabrication of Thin Films and Bulk Scaffold

3.5.1.1   PLGA Thin Film Fabrication

Soda-lime glass plate (3" x 4" x $^1/_{16}$", Moliterno, Inc., Pepperell, MA) was

rinsed in the order of acetone, propanol, ethanol, and methanol and blow-dried with

nitrogen to clean the surface. Cleaned glass plate was immediately placed in a plasma

generator (PlasmaPrep$_2$, Gala Instrumente, Germany) and treated with ionized oxygen for

30 seconds to render the surface hydrophilic. About 2 ml of 2% w/v alginate solution

(Sigma-Aldrich, St. Louis, MO) was poured onto the center of the treated glass plate and

spin-coated to achieve a uniform alginate thin coating. After drying the coating in an

oven at 60°C for 30 minutes, glass slides (1" x 3") were placed on the four edges of the

alginate-coated glass plate to enclose an open square. The glass slides were clamped

tightly onto the glass plate via 4 pairs of neodymium magnets (SuperMagnetMan,

Birmingham, AL) to secure their formation. 20 µL of 1% w/v gelatin solution (Sigma-

Aldrich, St. Louis, MO) was pipetted uniformly along each of the four edges of the open

square to seal any open gap between the glass slides and the glass plate. The construct

was placed in a fridge at 4°C to solidify the gelatin solution until ready to use.

Sugar (Domino Foods) particles were sieved between 90 to 106 µm. 1.2 g of

sieved sugar particles was added to 1 mL of 10% w/v poly(lactic-co-glycolic) acid

(PLGA, 75:25, Lakeshore Biomaterials, Birmingham, AL) in chloroform solution (Sigma,

St. Louis, MO) to achieve a 9:1 (sugar:PLGA) weight ratio. Prior to casting the mixture, the alginate-coated glass construct was taken out of the fridge and allowed to warm up to room temperature for 15 minutes. After briefly swirling the mixture by hand, it was poured onto the center of the open square area of the glass construct. The mixture was allowed to dry for 30 minutes in the fume hood followed by an overnight desiccation step to fully evaporate any chloroform residue in the sugar/PLGA film. Finally, the entire construct was immersed in 4 L of DiH_2O for 2 hours to leach out the sugar and to detach the film. The wet film was carefully placed on a Teflon net and allowed to dry for 4 hours in a 60°C oven.

3.5.1.2   Collagen Thin Film Fabrication

Glass plate (2" x 3" x $^1/_{16}$", VWR, Atlanta, GA) was rinsed in the order of acetone, propanol, ethanol, and methanol and blow-dried with nitrogen to clean the surface. 4 layers of Parafilm (VWR, Atlanta, GA) were wrapped near the edge of each side along the length of the plate to form a rectangular area with two open sides on the glass plate. The glass/Parafilm constructs was stored until ready to use.

2 g of collagen type I powder from bovine Achilles tendon (Sigma, St. Louis, MO) was added to 200 mL of 0.05 M glacial acetic acid (Sigma-Aldrich, St. Louis, MO) solution for 30 minutes. The mixture was blended in Oster blender at high setting for 8 minutes to achieve an uniformly mixed collagen slurry. The slurry was de-foamed by centrifugation at 2000 RPM for 10 minutes at 4°C. Immediately after de-foaming, 3 g of collagen slurry was spread within the rectangular open area of the glass plate/Parafilm M (VWR, Atlanta, GA) construct and sandwiched with another clean glass plate of the same

dimensions on top. The entire construct was clamped with 2 pairs of neodymium magnets (SuperMagnetMan, Birmingham, AL) to fasten the location of the glass slides and immediately placed horizontally in the freezer at -20°C for 24 hours to freeze the collagen slurry. The frozen collagen slurry construct was then transferred to a -80°C freezer for another 24 hours before finally lyophilized in a freeze-dryer (FTS System, Stone Ridge, NY) for 48 hours to obtain the collagen thin film.

3.5.1.3 Bulk Scaffold Fabrication

Similarly to the PLGA thin film, we fabricated the bulk PLGA scaffolds with a solvent casting and porogen leaching method. The casting volume was eight times higher than the thin film in order to keep the thickness of the bulk scaffold same as a 4-facet folded construct. We sieved sugar (Domino Foods) particles between 90 to 106 μm. 4.8 g of sieved sugar particles were added to 4 mL of 10% w/v PLGA (75:25, Lakeshore Biomaterials, Birmingham, AL) in chloroform (Sigma, St. Louis, MO) solution to achieve a 9:1 weight ratio. The mixture was swirled swiftly to homogenize the sugar particles and immediately casted into an alginate-coated well made from aluminum plate. After allowing the chloroform to evaporate and desiccate the construct overnight, the sugar was leached away in 4 L of DiH_2O for 4 hours. The wet film was placed on a Teflon net and allowed to became fully dry at room temperature.

To cut circular discs from the bulk scaffold sheet, we used the VersaLaser (VersaLaser VLS3.50, Scottsdale, AZ) set to 20% power and 80% speed with HPDFO lens. The diameter of the circular disc was 1 cm and we drew the shape in CorelDraw X5

(Corel, Menlo Park, CA) and imported into the VersaLaser graphic user interface (GUI) software.

3.5.2   Thin Film Characterization

3.5.2.1   Film Thickness

We measured the thickness of PLGA and collagen thin films via a digital caliper. To measure the average film thickness across the entire film, we folded the thin film two times to achieve a four layered construct and sandwiched the construct in-between two glass slides (1" x 3", VWR, Atlanta, GA) before measurement. The glass slides served as spacers to evenly distribute the compressive force exerted by the digital caliper during the measurement. The average single film thickness was obtained by subtracting the thickness of the two glass slide spacers and then dividing by four.

3.5.2.2   Collagen Thin Film Degradation

12 circular pieces of collagen thin film with an approximate diameter of 9 mm were cut using a stopper hole borer (VWR, Atlanta, GA). The mass of each film was measured on a digital atomic scale and placed in a 12-well plate (BD Biosciences). 3 mL of collagenase solution at 0.1 mg/mL in PBS was added to each well and a small metal mesh weight was added on top to fully submerge the samples. At 0.5, 1, 1.5 and 2-hour time points, the enzymatic degradation was stopped by adding 2 mL of 10 mM phosphate-buffered EDTA solution (Invitrogen) to three of the 12 wells followed by DI water rinsing three times. The samples were then desiccated overnight at room

temperature. The final mass of the dried samples were measured on the digital atomic scale to calculate the changes in mass due to degradation.

3.5.3   Laser-etching and Folding of Thin Film

Perforated lines in the shape of Miura-geometry were designed with CorelDraw X5 (Corel, Menlo Park, CA) and imported into VersaLaser GUI software. Laser (VersaLaser VLS3.50, Scottsdale, AZ) set to 10% power with 100% speed and HPDFO lens was sufficient to etch both PLGA and collagen thin sheet. Prior to laser etching, the thin PLGA or collagen sheet was taped at the four corners in the center of a letter-sized plain paper to prevent any accidental movement during the etching process. After the thin PLGA or collagen sheet was etched with the designed Miura-geometry pattern, it was stored in large deep Petri dishes until ready to use.

3.5.4   Post-stamping System Fabrication and Stamping

The post-stamping system is composed of three parts: cylindrical acrylic posts, an acrylic base plate and an acrylic top plate. The dimensions of the acrylic posts were designed in CorelDraw X5 (Corel, Menlo Park, CA) and cut out with VersaLaser (VersaLaser VLS3.50, Scottsdale, AZ) with 90% power, 9% speed and HPDFO lens from an 12" $\times$ 12" $\times$ $^1/_8$" acrylic plate (McMaster-Carr, Robbinsville, NJ). The diameter of the posts is 2 mm. After laser cutting, the posts remained loosely connected to the acrylic plate and could be easily removed by push gently with a pointed object such as a pair of tweezers. The top acrylic plate served as the base for posts attachment. The attachment locations were marked by gentle laser etching (50% power, 90% speed,

111

HPDFO lens) with VersaLaser (VersaLaser VLS3.50, Scottsdale, AZ) such that the corresponding stamping locations align along the *z*-axis of a folded thin film with Miura-geometry. The posts were individually glued to the marked locations with Epoxy (Permatex, Hartford, CT) and allowed to fully cure at room temperature for 4 hours. The bottom acrylic plate was consisted of two identical thin plates with dimensions 12" × 12" × $^1/_8$" (McMaster-Carr, Robbinsville, NJ) glued together. The outer shape of the unfolded 2D Miura-geometry was cut out in the center of one of the plates and served as a receiving base for the thin sheet. Finally, four screws were bored through at the four corners of the bottom plate with matching holes at the top plate to eliminate any movement laterally in the stamping process.

      Initial tests of post-stamping system with PLGA and collagen thin films were carried out with food colorings liquid droplets. For testing with PLGA thin films, we prepared diluted food coloring solutions by adding 5 drops of the concentrate (McCormick, Sparks, MD) to 10 mL of DiH$_2$O. For collagen thin films, the food coloring solution was added to 1% w/v gelatin/DiH$_2$O to increase the viscosity of the solution. The liquid droplets were pipetted onto each post on the top part of the post-stamping system and gently inverted and lowered onto the thin film that sit at the well at bottom part of the post-stamping system. The four nuts were threaded on the screw to prevent any vertical movement. The top part was lifted slowly after 1 minute of contact and inspected for any residue droplet.

3.5.5   Cell Culture

Human umbilical vein endothelial cells (HUVECs) (Lonza, Walkersville, MD) at passage 3 were cultured in EGM-2 media (Lonza, Walkersville, MD) in a water-jacketed 5% CO_2 incubator at 37°C. Following initial seeding, the cells were fed every other day until reaching 80-90% confluence, at which point, the cells were passaged and re-seeded at a density of 5000 cells/cm^2. All experiments were performed at passage 5-6.

Human aortic smooth muscle cells (HASMCs) (Lonza, Walkersville, MD) at passage 3 were cultured in SmGM-2 media (Lonza, Walkersville, MD) in a water-jacketed 5% CO_2 incubator at 37°C. Following initial seeding, the cells were fed every other day until reaching 60-70% confluence, at which point, the cells were passaged and re-seeded at a density of 10000 cells/cm^2. All experiments were performed at passage 5-6.

Whenever a mix population of both HUVECs and HASMCs were co-cultured in the folded or bulk construct, a mixed media consisted of 3 parts SmGM-2 and 1 part EBM-2 were used [232]. The media was changed every day until ready for *in vivo* implantation or *in vitro* assay.

3.5.6   Cell Patterning of Thin Film with Post-stamping System

Top and bottom parts of the post-stamping system were sterilized by spraying thoroughly with 70% v/v ethanol/DiH_2O followed by ultraviolet (UV) sterilization for 30 minutes in the biosafety cabinet. The perforated PLGA and collagen thin films were sterilized by UV sterilization for 1 hour on each side in the biosafety cabinet. Light neodymium magnetic rings (Model: R1013D, SuperMagnetMan, Birmingham, AL) were wrapped with Teflon tape and sterilized with sonication in 70% v/v ethanol/DiH_2O

solution for 15 minutes in a water-bath sonicator. The magnetic rings were air dried for 30 minutes within the biosafety cabinet and stored in a sterile Petri dish prior to cell patterning. All tweezers used for handling the thin film and the scaffold were sterilized in an autoclave.

Matrigel (BD Biosciences) was thawed in 4°C fridge overnight prior to the day of cell patterning. On the day of patterning, HUVECs or HASMCs in tissue culture flask were detached with 2 mL of 0.25% trypsin for 4 minutes at 37°C. The trypsinization reaction was stopped by adding 5 mL of the corresponding culture media and subsequently centrifuged at 2200 RPM for 5 minutes at 4°C. The supernatant was discarded and the cell pellet was suspended in a cold 50% v/v media/Matrigel solution at a density of 1×10^8 cells/mL. The cell suspension was pipetted rapidly to uniformly disperse the cell pellet and kept ice until use. A mixed population of HUVECs and HASMCs was prepared by pipetting equal volumes of cell suspension from each individual cell suspension and mixed thoroughly with a pipette.

Sterilized PLGA or collagen thin film was placed within the receiving base of the bottom part of the post-stamping system. 3 µL cell suspension of interest were deposited onto the posts by pipetting manually to achieve the desired cellular arrangement. Cell suspension was mixed by pipetting every 5 transfers to ensure an even amount of cells deposited on each post. When all posts were loaded with cell suspensions, the posts were inverted and put in contact with the thin film. Four nuts were threaded on the screws to prevent any vertical movement. The top part was lifted slowly after 1 minute of contact and inspected for cell suspension residues. The thin film was removed carefully from the well with sterile tweezers and folded following the creased lines into

the 3D Miura-geometry. The folded construct was clamped with a pair of Teflon tape wrapped magnetic rings to prevent the construct from unfolding and placed in a 12 well plate at 4°C. After completing all folded constructs, the 12-well plate was incubated in a water-jacketed 5% CO_2 incubator at 37°C for 10 minutes without media to polymerize the Matrigel and encapsulate the patterned cells at their stamping locations. Subsequently, 3 mL of 37°C media corresponding to the patterned cell populations was added to each well to fully immerse the construct. Due to the weight of the magnetic rings, the cell-bearing construct stayed immersed within the media. The constructs were cultured until ready for *in vivo* implantation or *in vitro* assay.

3.5.7   Immunohistochemistry

3.5.7.1   Cell Membrane Labeling

To label cell of interest with DiI or DiO membrane dye prior to stamping, cells were suspended at 1×10^6 cells/mL in serum-free culture media (EBM-2 for EC or SmBM basal medium for VSMC, Lonza, Walkersville, MD). 5 µL of cell-labeling solution (Vybrant Multicolor Cell-Labeling Kit, Invitrogen) per mL of cell suspension was added to the cell suspension and mixed by gently pipetting. The cell suspensions was then incubated in the water-jacketed 5% CO_2 incubator at 37°C for 20 minutes followed by centrifuge at 1500 RPM for 5 minutes at room temperature. The supernatant was carefully removed and the cells were then re-suspended at 1×10^6 cells/mL in their corresponding media at 37°C. The cells were washed three times by centrifuging at 1500 RPM for 5 minutes followed by removing the supernatant. The cell suspension was then stored on ice bath until ready to use.

115

3.5.7.2   Immunohistochemistry Paraffin Staining on Sectioned Slides

Paraffin-embedded sectioned slice of explanted scaffold were stained for ECs and VSMCs. The 5 µL sectioned slices were deparaffinized by sequentially immersed in xylene (Sigma, St. Louis, MO, xylene, ethanol, ethanol, 95% ethanol, 95% ethanol, 70% ethanol, 50% ethanol, DiH$_2$O, DiH$_2$O, and Tris-buffered saline (TBS, Cellgro, Radnor, PA) for 2 minutes each. Prior to antibody staining, antigen retrieval is performed by immersing the deparaffinized slides in Tris-EDTA buffer (10 mM Tris, 1 mM EDTA, 0.05% Tween 20 adjusted to pH 9.0) at 95°C for 30 minutes. After allowing the slides to cool down to room temperature, the slides were blocked with 5% goat serum in TBS for 1 hour at room temperature followed by incubation with a rabbit anti-human caldesmon primary antibody (ab45691, 1:100 dilution, Abcam, Cambridge, MA) in 5% goat serum overnight at 4°C. On the following day, the slides were washed for three times in TBS for 5 minutes each and stained with a goat anti-rabbit Texas Red secondary antibody (ab6719, 1:100 dilutions, Abcam, Cambridge, MA) in 5% goat serum for 40 minutes at room temperature. After washing the slides for three times in TBS for 5 minutes each, the slides were blocked with 5% donkey serum in TBS for 1 hour and subsequently incubated overnight with a sheep anti-human CD31 primary antibody (af806, 1:30 dilutions, R&D Systems, Minneapolis, MN) at 4°C in 5% donkey serum. The slides were washed for three times in TBS for 5 minutes each at room temperature on the following day and stained with a donkey anti-sheep FITC secondary antibody (ab97124, 1:100 dilutions, Abcam, Cambridge, MA) in 5% donkey serum for 40 minutes at room temperature. Finally, the slides were rinsed for three times in TBS for 5 minutes each and

mounted on glass slides using Prolong Gold antifade reagent with DAPI (Invitrogen) and stored in -20°C freezer until confocal imaging. All incubations steps were carried out in a humidified chamber to prevent slide from drying out.

3.5.8   Scanning Electron Microscopy

Field emission scanning electron microscopy (FESEM, Zeiss Ultra 55, Thornwood, NY) images of the PLGA and collagen thin films were taken to visualize the porous structure within the film. Prior to SEM, PLGA or collagen samples near the center of the film was cut out and coated with Pt/Pd for 90 seconds at 40 mA with a sputter coater (208HR, Cressington Scientific Instruments, UK). Samples were imaged using SEM at a beam voltage of 5 kV.

3.5.9   Confocal Microscopy

3.5.9.1   *Z-stack Imaging of Whole-mount Folded Construct*

Patterned cells labeled with DiI and DiO in folded Miura-geometry construct were fixed in 4% paraformaldehyde for 15 minutes and stained *in situ* with DAPI nucleus stain for 5 minutes at room temperature. The construct was washed in PBS for three times at 5 minutes each and placed in a glass bottom Petri dish (MatTek Corporation, Ashland, MA) with PBS. Prior to Z-stack confocal imaging, the construct was weighed down with a 22 mm coverslip on top of the construct to prevent any accidental movement and to ensure a good contact with the bottom glass. 20 *z*-stack slices spanning 140 μm were scanned sequentially (Carl Zeiss LSM 510 inverted confocal microscope, Thornwood, NY) with a C-Apochromat 40x/1.2 W lens at 1x zoom and laser wavelengths at 405, 484

and 549 nm for DAPI, DiO and DiI staining, respectively. 3D renderings of cell

distribution were reconstructed using the Zen 2011 software.

3.5.9.2   Grid Imaging of Sectioned Slide from in vivo Explants

36 fields of view consisted of 6 rows labeled 1 to 6 and 6 columns labeled A to

F were imaged systemically for each deparaffinized stained slide using the grid-imaging

tool in Zen 2011 image acquisition software (Carl Zeiss LSM 510 inverted confocal

microscope, Thornwood, NY). For each sectioned construct, the four corners representing

the maximum and minimum coordinates in the *x*- and *y*-axis were set as the four corner

images for the grid (1A, 1F, 6A and 6F). DAPI, FITC and Texas Red stains were

sequentially excited with 405 nm, 488 nm and 633 nm lasers respectively and imaged for

each grid (Carl Zeiss LSM 510 inverted confocal microscope, Thornwood, NY).

3.5.10   Cell Viability and Metabolic Assays

The viability of cells encapsulated in polymerized Matrigel (BD Biosciences) in

folded PLGA construct was examined by a Live/Dead (viability/cytotoxicity) assay for

mammalian cells (Molecular Probes, Eugene, OR). Two hours after initial seeding,

folded construct was washed gently with Dulbecco's phosphate-buffered saline (D-PBS,

Invitrogen) and incubated with 2 μM calcein-AM and 4 μM ethidium homodimer-1

(Molecular Probes, Eugene, OR) for 45 minutes at room temperature before imaged with

a Zeiss Axiovert 200 M fluorescence microscope (Carl Zeiss Micro-Imaging,

Thornwood, NY) with GFP and Texas Red channels.

To quantitatively assess the metabolic activities of seeded cells in folded or bulk PLGA construct after an extended period of culture, alamarBlue cell viability assay (Invitrogen) was used. After 3 days of culture in a 12-well plate with media change every day, folded or bulk construct was washed gently with D-PBS and then replenished with 2 mL of fresh culture media. Prior to adding alamarBlue solution, the constructs were cut into small pieces with sterile surgical scissors within the well to increase the surface area to volume ratio. After 200 µL of alamarBlue solution was added to each well, the plate was gently swirled until the alamarBlue solution became uniformly mixed with the media. The plate was then incubated for 1 hour in a water-jacketed 5% CO_2 incubator. After gently pipetting each well up and down a few times to mix the solution, three 100 µL solution of each condition were added to a 96-well plate and its fluorescence was read using a fluorescence excitation wavelength of 570 nm and emission wavelength of 585 nm (Gemini XPS fluorescence microplate reader, Molecular Devices, Sunnyvale, CA). We used an acellular PLGA scaffold as negative control and subtracted its fluorescent readings as background from other conditions.

3.5.11   *in vivo* Mouse Implantation of Scaffold and Harvest

All animal experiment was approved by the Standing Committee on the Use of Animal in Research and Teaching at the Faculty of Arts and Sciences at Harvard University. Male C.B.-17 SCID/beige mice between 5-8 weeks (Taconic Farms, Germantown, NY) were anesthetized by 2% isofluorane in 98% O_2 via inhalation using a nose cone on a water-heated surgical platform. After shaving the dorsal trunk and preparing the skin for surgery, one 1 cm incision pocket was made on each side of the

dorsum and a subcutaneous pocket was created for scaffold implantation. Each mouse received a combination of a bulk and a Miura-folded scaffold or two pairs of Miura-folded scaffold of different seeding configurations. Incisions was sutured (3-4 sutures per incision) with polypropylene monofilament suture (PROLENE, Ethicon, Somerville, NJ). Subcutaneous injections of buprenorphine (American Regent Inc., Shirley, NY) were given to all mice every 12 hours for 72 hours as analgesia. Up to 4 mice was placed in an individual cage until harvest two weeks later from the initial surgery date.

On day 14 since initial surgery, the mice were euthanized and incisions were made with surgical scissors around the subcutaneous pockets to harvest the implanted construct. Roughly a 1 cm^2 skin section was removed and fixed in 4% paraformaldehyde overnight. On the following day, the fixed tissues were transferred to 70% ethanol solution and shipped to Mass Histology Service (Worcester, MA) for paraffin embedding and sectioning.

3.5.12 Vessel Density Calculation

Blood vessels in confocal images were identified by anti-human CD31 and anti-human Caldesmon immunofluorescent staining. For each sectioned slice of the explanted construct, the number of human Caldesmon positive blood vessels was manually counted from the 36 field of views designated from 1A to 6F. The total blood vessel number were averaged with the two other constructs and divided by the total area of the field of view to obtain the vessel density. All results were compared using ANOVA on rank tests, with pairwise comparison performed using the Tukey's test.

4   Conclusion

Vascular tissue functions are fundamentally linked to its structural organization across multiple spatial scales. At the tissue level, endothelial cells line the inner most layer of the blood vessel to protect the VSM from blood shearing force while VSM wraps around the ECs in helices in order to withstand the expansion force both longitudinally and laterally. At the cellular level, VSMCs assume an elongated spindle-shape and connect with either other cells or the ECM in order to efficiently propagate mechanical forces along the blood vessel wall. At the subcellular level, cytoskeletal architecture can influence a wide array of VSM functions including proliferation, migration and contraction. When this elegant structure-function relationship in vascular tissue is disrupted in pathological conditions, maladaptive remodeling in the tissue structure can lead to diseased functional outcomes *in vitro*. While it is difficult to pinpoint the exact cause that initiated the structure remodeling *in vitro* due to the complex native signal and tissue interactions, a highly controllable artificial cellular microenvironment can be engineered *in vitro* to regulate the tissue structure and in turn, tissue functions. With the integration of increasingly precise microfabrication technologies in tissue engineering, an engineering algorithm based on designing and building vascular architecture to achieve desired functional outcomes has emerged. For example, our group has previously applied this algorithm in a proof-of-concept study and successfully reverse engineered a *Aurelia aurita* jellyfish in a biohybrid life form consisted of synthetic polymer thin film and spatially engineered rat cardiac tissue [233]. With this dissertation, we developed *in vitro* models to understand how cellular shape of VSMC as a structural input can affect its contractile strength and cytoskeletal arrangement and how engineered spatial

121

organizations of ECs and SMCs in a three-dimensional polymer matrices can affect vascularization.

4.1 The Effect of Vascular Smooth Muscle Cell Shape on Cytoskeletal Architecture and Contractile Strength

Although structure and function are closely coupled in the vascular tissues as described above, their relationship can vary depending on the location in which they were found. For example, it has been observed that VSMC shape and function are uniquely defined by the locations in the cardiovascular system. In large diameter elastic arteries, exemplified by the aorta, VSMC has a length to width aspect ratio of about 10:1. However, in mid-sized muscular arteries, such as the external carotid artery of the neck and femoral artery of the thighs, the VSMC AR increased to 15:1. Functionally, VSMC in elastic arteries contract to maintain vessel pressure during the cardiac cycle whereas VSMC in muscular arteries regulate blood flow and pressure by constricting or relaxing the vessel wall. While it has been speculated that the elongated cellular shape for VSMC in elastic arteries may provide better dynamic response to blood pressure and pressure changes, its primary function, there is no definitive evidence to support this structure-function relationship.

In chapter 2, we investigated the how the contractile strength and cytoskeletal architecture of VSMC changes as a function of its cellular shape. We developed an *in vitro* model by engineering human VSMCs to take on the same shapes as those seen in elastic and muscular arteries and measured their contraction during stimulation with endothelin-1. We measured the actin alignment and nuclear eccentricity of engineered

VSMCs and found that they increased as the shape of the cell elongated. Using traction force microscopy, we measured the contractile strength of individual VSMCs and found VSMCs with elongated shapes exhibited lower contractile strength but greater percentage increase in contraction after endothelin-1 stimulation. We analysed the relationship between smooth muscle contractility and subcellular architecture and found that changes in contractility were correlated with actin alignment and nuclear shape. These results suggest that elongated VSMC shape facilitate muscular artery tone modulation by increasing its dynamic contractile range, suggesting that where the vasculature requires a higher fidelity in its modulation of blood flow, longer, thinner cells are functionally advantageous.

This study highlighted the advantage of the design, build and test engineering algorithm for *in vitro* systems where we can precisely design the cellular microenvironment, build the cell or tissue of interest and test exactly how an independent input, the cell shape, can affect a dependent output, the contractile strength. In addition, this result here is particularly relevant for the tissue engineering of small-diameter vessel graft where functional mismatch between host and graft has been a major challenge in the past two decades. Our findings suggest that in addition to mimicking the biomechanical aspect of the healthy artery, providing guidance cues to engineer the VSMCs into the desired shape may improve the functionality and long-term patency of vascular graft.

4.2 Engineering Vascularized Network in Folded, Porous Polymer Matrices by Tissue Origami

At the tissue level, design considerations for engineering vascular tissues broaden to include the spatial interaction and assembly between multiple cell types. However, these factors are often neglected in conventional tissue design dogma where multiple cell types are simply mixed and directly placed on the supporting polymer matrices, without controlling for their three-dimensional structural organization. As a result, the engineered tissue construct often has little organization to its architecture. In contrast, tissues *in vitro* consist of hierarchical smaller repeating unit on the scale of hundreds of microns that interacts with neighboring cells and performance specific functions. This difference in microarchitecture leads to suboptimal functions for tissue engineered construct and hindered the advancement of this field in achieving clinically relevant organ replacement products.

In chapter 3, we developed a novel 3-dimensional cell patterning method based on folding of polymer thin film to spatially organize cellular interactions. We fabricated porous, foldable thin films from synthetic (PLGA) and natural (collagen) polymers and laser-etched perforated lines in them to facilitate the folding process. We built a simple acrylic stamping system that utilizes small posts to deposit liquid cell suspensions at user-defined locations on the 2-dimensional thin film. The 3-dimensional tissue construct with spatially defined cellular interactions was obtained by folding the cell-patterned thin film into a Miura-ori geometry and cultured. We evaluated the viability of cells in folded construct and found they remain alive after 72 hours. We applied this method in a proof-of-concept study to build a vascularized tissue with different EC and VSMC spatial configurations in a subcutaneous immunodeficient mouse *in vitro* model. We found that folded scaffold with EC and SMC patterned laterally on the same plane produced a

significantly higher number of vessels compared to folded configuration where EC and SMC were seeded in a homogeneous mixture.

Prior to the development of this method, organization of spatial cellular interactions in 3-dimensionl synthetic and natural polymer scaffold remains a challenge. The fact that this method is compatible with both synthetic and natural polymers makes it widely applicable to many fields of tissue engineering in which these types of polymers were frequently used as scaffolding materials for cells. In addition, with the field of tissue engineering moving towards co-culture of multiple cell types, the ability to spatially organize their interactions in 3-dimensional scaffold can be a valuable tool. With our proof-of-concept study in building vascularized tissue with patterned ECs and SMCs, our findings suggested that increasing spatially organized interactions between ECs and SMCs may lead to a more efficient vascularization in a porous synthetic scaffold than simply mixing the two cell types homogeneously. This is particularly relevant for engineering thicker or more metabolically demanding tissue replacement where more efficient vascularization may improve overall tissue survival and function.

4.3 Limitations and Future Directions

With this dissertation, we elucidated how structure cues such as cell shape and spatial interactions between multiple cell types can affect the functions of cells and tissues. One of the drawbacks for our study in chapter 2 is the use of isolated VSMCs, which lacks physiological relevance compared to confluent VSMC tissue *in vitro*. In a previous study where we investigated the contractility of patterned VSM tissue, the cellular shapes assume a range of length to width ratios in VSM tissues. Therefore, there

125

is a tradeoff between *in vitro* relevancy and the precision in control over the microenvironment. A possible solution to this challenge may be to grow VSMCs on close-packed micropatterned ECM protein islands such that individual VSMC shapes can be controlled while allowing neighboring VSMCs to communicate with each other. This may lead to more physiologically relevant *in vitro* VSM tissue model and bring us closer to achieving an engineered functional VSM tissue.

One limitation of our 3D cell patterning strategy in chapter 3 is the need for Matrigel for seeding the cells on the polymer thin films. The Matrigel encapsulates the patterned cells on the thin film when polymerized, allowing us to control the spatial cell distribution in 3D. Since Matrigel is a protein mixture secreted by the Engelbreth-Holm-Swarm mouse sarcoma cells, it may contain growth factors or cytokines that signals non-physiological behavior on human cells. This poses significant concern for using this strategy in a clinical setting. Therefore, future studies should test for replacement hydrogel material that allows cell encapsulation, yet do not contain the mixture of cytokines.

4.4　　Dissertation Summary

Collectively, the work in this dissertation provided new insights into the effect of cell shape and tissue spatial organizations on the functions of engineered vascular tissues. In chapter 1, we first presented an engineering algorithm that is broadly applicable for building biological tissues. We used vascular smooth muscle tissue as an example and elucidated how we can engineer a functional VSM *in vitro* by designing the cellular architecture with mechanotransductive cytoskeletal proteins, building it with

engineered mechanical cues in the cellular microenvironment, and finally testing the performance of the engineered cells with a functional metrics. We applied this engineering algorithm in chapter 2 by designing and building human vascular smooth muscle cells to take on the same shapes as those seen in elastic and muscular arteries *in vitro* and subsequently measuring their contraction during stimulation with endothelin-1 with traction force microscopy as a function of cellular shape. We found the actin alignment and nuclear eccentricity of engineered VSMCs increased as the shape of the cell elongated. We found VSMCs with elongated shapes exhibited lower contractile strength but greater percentage increase in contraction after endothelin-1 stimulation, suggesting elongated VSMC shape enables muscular artery to have greater dynamic contractile range. In chapter 3, we developed a 3-dimensional cellular patterning strategy based on folding of polymer thin films and measured the effect of spatial interactions between ECs and SMCs in forming a vascularized network in folded, porous polymer matrices. We folded PLGA and collagen thin films along laser-etched perforated lines and patterned the thin films by stamping cell suspensions on them with a post-stamping system. We evaluated the cell survival in folded construct and found cells were viable after 72 hours post stamping. We used an subcutaneous implantation mouse model to evaluate vascularization efficiency and found that three-dimensional organization that patterned human ECs and SMCs within the same folding facet had significantly higher density of human caldesmon positive blood vessels than folded construct patterned with a homogenously mixed populations of ECs and SMCs, suggesting that increasing spatially organized interactions between EC and SMC may lead to more densely vascularized tissues.

In summary, this dissertation enhanced our understanding for the design and assembly of engineered vascular tissues. We learned that structure and functions are closely coupled in vascular systems across multiple spatial scales and as bioengineers, we can harness this structure-function relationship by engineering cellular and tissue microenvironment to build specific cellular and tissue architecture that give rises to desired functions *in vitro*.

4.5   Funding Sources

5   Bibliography

[1] Osol G. Mechanotransduction by vascular smooth muscle. Journal of vascular research. 1995;32:275-92.

[2] Gunst SJ, Zhang W. Actin cytoskeletal dynamics in smooth muscle: a new paradigm for the regulation of smooth muscle contraction. American Journal of Physiology-Cell Physiology. 2008;295:C576-C87.

[3] Cunningham JJ, Linderman JJ, Mooney DJ. Externally applied cyclic strain regulates localization of focal contact components in cultured smooth muscle cells. Annals of biomedical engineering. 2002;30:927-35.

[4] Hayakawa K, Sato N, Obinata T. Dynamic reorientation of cultured cells and stress fibers under mechanical stress from periodic stretching. Experimental cell research. 2001;268:104-14.

[5] Sparks HV. Effect of quick stretch on isolated vascular smooth muscle. Circulation Research. 1964;15:254-&.

[6] Langton PD. Calcium-channel currents recorded from isolated myocytes of rat basilar artery are stretch sensitive. Journal of Physiology-London. 1993;471:1-11.

[7] Kirber MT, Ordway RW, Clapp LH, Walsh JV, Singer JJ. Both membrane stretch and fatty-acids directly activate large conductance Ca^{2+} activated K^+ channels in vascular smooth muscle cells. Febs Letters. 1992;297:24-8.

[8] Pirola C, Wang H, Strgacich M, Kamyar A, Cercek B, Forrester J, et al. Mechanical stimuli induce vascular parathyroid hormone-related protein gene expression in vivo and in vitro. Endocrinology. 1994;134:2230-6.

[9] Mills I, Letsou G, Rabban J, Sumpio B, Gewirtz H. Mechanosensitive adenylate cyclase activity in coronary vascular smooth muscle cells. Biochemical and biophysical research communications. 1990;171:143-7.

[10] Cattaruzza M, Lattrich C, Hecker M. Focal adhesion protein zyxin is a mechanosensitive modulator of gene expression in vascular smooth muscle cells. Hypertension. 2004;43:726-30.

[11] Kulik TJ, Bialecki RA, Colucci WS, Rothman A, Glennon ET, Underwood RH. Stretch increases inositol trisphosphate and inositol tetrakisphosphate in cultured pulmonary vascular smooth muscle cells. Biochemical and biophysical research communications. 1991;180:982-7.

[12] Davis MJ. Perspective: physiological role (s) of the vascular myogenic response. Microcirculation. 2012;19:99-114.

[13] Mecham RP, Whitehouse LA, Wrenn DS, Parks WC, Griffin GL, Senior RM, et al. Smooth-muscle mediated connective-tissue remodeling in pulmonary-hypertension. Science. 1987;237:423-6.

[14] Yamaguchi-Okada M, Nishizawa S, Koide M, Nonaka Y. Biomechanical and phenotypic changes in the vasospastic canine basilar artery after subarachnoid hemorrhage. Journal of Applied Physiology. 2005;99:2045-52.

[15] Freis ED, Papademetriou V. Current drug treatment and treatment patterns with antihypertensive drugs. Drugs. 1996;52:1-16.

[16] Nardi A, Olesen S-P. BK channel modulators: a comprehensive overview. Current medicinal chemistry. 2008;15:1126-46.

[17] Wiesner S, Legate K, Fässler R. Integrin-actin interactions. Cellular and Molecular Life Sciences CMLS. 2005;62:1081-99.

[18] Philippova M, Bochkov V, Stambolsky D, Tkachuk V, Resink T. T-cadherin and signal-transducing molecules co-localize in caveolin-rich membrane domains of vascular smooth muscle cells. FEBS letters. 1998;429:207-10.

[19] Gimbrone Jr M, Cotran R. Human vascular smooth muscle in culture. Growth and ultrastructure. Laboratory investigation; a journal of technical methods and pathology. 1975;33:16-27.

[20] Glukhova MA, Frid MG, Koteliansky VE. Phenotypic changes of human aortic smooth muscle cells during development and in the adult vessel. American Journal of Physiology-Heart and Circulatory Physiology. 1991;261:78-80.

[21] Moiseeva EP. Adhesion receptors of vascular smooth muscle cells and their functions. Cardiovascular research. 2001;52:372-86.

[22] Wilson E, Sudhir K, Ives HE. Mechanical strain of rat vascular smooth muscle cells is sensed by specific extracellular matrix/integrin interactions. Journal of Clinical Investigation. 1995;96:2364.

[23] Mogford JE, Davis GE, Platts SH, Meininger GA. Vascular smooth muscle $\alpha v \beta 3$ integrin mediates arteriolar vasodilation in response to RGD peptides. Circulation research. 1996;79:821-6.

[24] D'Angelo G, Mogford J, Davis G, Davis M, Meininger G. Integrin-mediated reduction in vascular smooth muscle $[Ca2+]$ i induced by RGD-containing peptide.

American Journal of Physiology-Heart and Circulatory Physiology. 1997;272:H2065-H70.

[25] Martinez-Lemus LA, Crow T, Davis MJ, Meininger GA. αvβ3-and α5β1-integrin blockade inhibits myogenic constriction of skeletal muscle resistance arterioles. American Journal of Physiology-Heart and Circulatory Physiology. 2005;289:H322-H9.

[26] Sun Z, Martinez-Lemus LA, Hill MA, Meininger GA. Extracellular matrix-specific focal adhesions in vascular smooth muscle produce mechanically active adhesion sites. American Journal of Physiology-Cell Physiology. 2008;295:C268-C78.

[27] Balasubramanian L, Lo C-M, Sham JS, Yip K-P. Remanent cell traction force in renal vascular smooth muscle cells induced by integrin-mediated mechanotransduction. American Journal of Physiology-Cell Physiology. 2013;304:C382-C91.

[28] Wu X, Yang Y, Gui P, Sohma Y, Meininger GA, Davis GE, et al. Potentiation of large conductance, Ca2+‐activated K+ (BK) channels by α5β1 integrin activation in arteriolar smooth muscle. The Journal of Physiology. 2008;586:1699-713.

[29] Min J, Reznichenko M, Poythress RH, Gallant CM, Vetterkind S, Li Y, et al. Src modulates contractile vascular smooth muscle function via regulation of focal adhesions. Journal of cellular physiology. 2012;227:3585-92.

[30] Hill MA, Meininger GA, Davis MJ, Laher I. Therapeutic potential of pharmacologically targeting arteriolar myogenic tone. Trends in pharmacological sciences. 2009;30:363-74.

[31] Ganz A, Lambert M, Saez A, Silberzan P, Buguin A, Mège RM, et al. Traction forces exerted through N‐cadherin contacts. Biology of the Cell. 2006;98:721-30.

[32] Desai RA, Gao L, Raghavan S, Liu WF, Chen CS. Cell polarity triggered by cell-cell adhesion via E-cadherin. Journal of cell science. 2009;122:905-11.

[33] Liu Z, Tan JL, Cohen DM, Yang MT, Sniadecki NJ, Ruiz SA, et al. Mechanical tugging force regulates the size of cell–cell junctions. Proceedings of the National Academy of Sciences. 2010;107:9944-9.

[34] Uglow E, Angelini G, George S. Cadherin expression is altered during intimal thickening in humal sapphenous vein. J Submicrosc Cytol Pathol. 2000;32:C113-C9.

[35] Sabatini PJ, Zhang M, Silverman-Gavrila R, Bendeck MP, Langille BL. Homotypic and endothelial cell adhesions via N-cadherin determine polarity and regulate migration of vascular smooth muscle cells. Circulation research. 2008;103:405-12.

[36] Jones M, Sabatini PJ, Lee FS, Bendeck MP, Langille BL. N-cadherin upregulation and function in response of smooth muscle cells to arterial injury. Arteriosclerosis, thrombosis, and vascular biology. 2002;22:1972-7.

[37] Koutsouki E, Beeching CA, Slater SC, Blaschuk OW, Sala-Newby GB, George SJ. N-Cadherin–Dependent Cell–Cell Contacts Promote Human Saphenous Vein Smooth Muscle Cell Survival. Arteriosclerosis, thrombosis, and vascular biology. 2005;25:982-8.

[38] Jackson TY, Sun Z, Martinez-Lemus LA, Hill MA, Meininger GA. N-Cadherin and Integrin Blockade Inhibit Arteriolar Myogenic Reactivity but not Pressure-Induced Increases in Intracellular Ca2+. Frontiers in physiology. 2010;1.

[39] Tkachuk VA, Bochkov VN, Philippova MP, Stambolsky DV, Kuzmenko ES, Sidorova MV, et al. Identification of an atypical lipoprotein-binding protein from human aortic smooth muscle as T-cadherin. FEBS letters. 1998;421:208-12.

[40] Kim HR, Gallant C, Leavis PC, Gunst SJ, Morgan KG. Cytoskeletal remodeling in differentiated vascular smooth muscle is actin isoform dependent and stimulus dependent. American Journal of Physiology-Cell Physiology. 2008;295:C768-C78.

[41] Fatigati V, Murphy R. Actin and tropomyosin variants in smooth muscles. Dependence on tissue type. Journal of Biological Chemistry. 1984;259:14383-8.

[42] Gallant C, Appel S, Graceffa P, Leavis P, Lin JJ-C, Gunning PW, et al. Tropomyosin variants describe distinct functional subcellular domains in differentiated vascular smooth muscle cells. American Journal of Physiology-Cell Physiology. 2011;300:C1356-C65.

[43] Adler KB, Krill J, Alberghini TV, Evans JN. Effect of cytochalasin D on smooth muscle contraction. Cell motility. 1983;3:545-51.

[44] Cipolla MJ, Osol G. Vascular smooth muscle actin cytoskeleton in cerebral artery forced dilatation. Stroke. 1998;29:1223-8.

[45] Saito S, Hori M, Ozaki H, Karaki H. Cytochalasin D inhibits smooth muscle contraction by directly inhibiting contractile apparatus. Journal of smooth muscle research= Nihon Heikatsukin Gakkai kikanshi. 1996;32:51.

[46] Wright G, Hurn E. Cytochalasin inhibition of slow tension increase in rat aortic rings. American Journal of Physiology-Heart and Circulatory Physiology. 1994;267:H1437-H46.

[47] Cipolla MJ, Gokina NI, Osol G. Pressure-induced actin polymerization in vascular smooth muscle as a mechanism underlying myogenic behavior. The FASEB journal. 2002;16:72-6.

[48] Bárány M, Barron JT, Gu L, Bárány K. Exchange of the actin-bound nucleotide in intact arterial smooth muscle. Journal of Biological Chemistry. 2001;276:48398-403.

[49] Flavahan NA, Bailey SR, Flavahan WA, Mitra S, Flavahan S. Imaging remodeling of the actin cytoskeleton in vascular smooth muscle cells after mechanosensitive arteriolar constriction. American Journal of Physiology-Heart and Circulatory Physiology. 2005;288:H660-H9.

[50] Srinivasan R, Forman S, Quinlan RA, Ohanian J, Ohanian V. Regulation of contractility by Hsp27 and Hic-5 in rat mesenteric small arteries. American Journal of Physiology-Heart and Circulatory Physiology. 2008;294:H961-H9.

[51] Kim HR, Leavis PC, Graceffa P, Gallant C, Morgan KG. A new method for direct detection of the sites of actin polymerization in intact cells and its application to differentiated vascular smooth muscle. American Journal of Physiology-Cell Physiology. 2010;299:C988-C93.

[52] Calderwood DA, Shattil SJ, Ginsberg MH. Integrins and actin filaments: reciprocal regulation of cell adhesion and signaling. J Biol Chem. 2000;275:22607-10.

[53] Yamada S, Pokutta S, Drees F, Weis WI, Nelson WJ. Deconstructing the cadherin-catenin-actin complex. Cell. 2005;123:889-901.

[54] Sharif-Naeini R, Folgering JH, Bichet D, Duprat F, Lauritzen I, Arhatte M, et al. Polycystin-1 and-2 dosage regulates pressure sensing. Cell. 2009;139:587-96.

[55] Berner PF, Somlyo AV, Somlyo AP. Hypertrophy-induced increase of intermediate filaments in vascular smooth muscle. The Journal of cell biology. 1981;88:96-100.

[56] Frank ED, Warren L. Aortic smooth muscle cells contain vimentin instead of desmin. Proceedings of the National Academy of Sciences. 1981;78:3020-4.

[57] Gabbiani G, Schmid E, Winter S, Chaponnier C, De Ckhastonay C, Vandekerckhove J, et al. Vascular smooth muscle cells differ from other smooth muscle cells: predominance of vimentin filaments and a specific alpha-type actin. Proceedings of the National Academy of Sciences. 1981;78:298-302.

[58] Johansson B, Eriksson A, Virtanen I, Thornell LE. Intermediate filament proteins in adult human arteries. The Anatomical Record. 1997;247:439-48.

[59] Schiffers P, Henrion D, Boulanger C, Colucci-Guyon E, Langa-Vuves F, Van Essen H, et al. Altered flow–induced arterial remodeling in vimentin-deficient mice. Arteriosclerosis, thrombosis, and vascular biology. 2000;20:611-6.

[60] Loufrani L, Matrougui K, Li Z, Lévy BI, Lacolley P, Paulin D, et al. Selective microvascular dysfunction in mice lacking the gene encoding for desmin. The FASEB Journal. 2002;16:117-9.

[61] Wang R, Li Q, Tang DD. Role of vimentin in smooth muscle force development. American Journal of Physiology-Cell Physiology. 2006;291:C483-C9.

[62] Tang D, Bai Y, Gunst S. Silencing of p21-activated kinase attenuates vimentin phosphorylation on Ser-56 and reorientation of the vimentin network during stimulation of smooth muscle cells by 5-hydroxytryptamine. Biochem J. 2005;388:773-83.

[63] Tang DD. Intermediate filaments in smooth muscle. American Journal of Physiology-Cell Physiology. 2008;294:C869-C78.

[64] Wang N, Butler J, Ingber D. Mechanotransduction across the cell surface and through the cytoskeleton. Science. 1993;260:1124-7.

[65] Yamin R, Morgan KG. Deciphering actin cytoskeletal function in the contractile vascular smooth muscle cell. The Journal of physiology. 2012;590:4145-54.

[66] Platts SH, Martinez-Lemus LA, Meininger GA. Microtubule-dependent regulation of vasomotor tone requires Rho-kinase. Journal of vascular research. 2002;39:173-82.

[67] Paul RJ, Bowman PS, Kolodney MS. Effects of microtubule disruption on force, velocity, stiffness and [Ca2+] i in porcine coronary arteries. American Journal of Physiology-Heart and Circulatory Physiology. 2000;279:H2493-H501.

[68] Wilhelmsen K, Litjens SH, Kuikman I, Tshimbalanga N, Janssen H, van den Bout I, et al. Nesprin-3, a novel outer nuclear membrane protein, associates with the cytoskeletal linker protein plectin. The Journal of cell biology. 2005;171:799-810.

[69] King MC, Drivas TG, Blobel G. A network of nuclear envelope membrane proteins linking centromeres to microtubules. Cell. 2008;134:427-38.

[70] Xiong H, Rivero F, Euteneuer U, Mondal S, Mana‐Capelli S, Larochelle D, et al. Dictyostelium Sun‐1 Connects the Centrosome to Chromatin and Ensures Genome Stability. Traffic. 2008;9:708-24.

[71] Wang N, Tytell JD, Ingber DE. Mechanotransduction at a distance: mechanically coupling the extracellular matrix with the nucleus. Nature reviews Molecular cell biology. 2009;10:75-82.

[72] Kuo K-H, Seow CY. Contractile filament architecture and force transmission in swine airway smooth muscle. Journal of cell science. 2004;117:1503-11.

[73] Nagayama K, Yahiro Y, Matsumoto T. Stress fibers stabilize the position of intranuclear DNA through mechanical connection with the nucleus in vascular smooth muscle cells. FEBS letters. 2011;585:3992-7.

[74] Lee H-Y, Oh B-H. Aging and arterial stiffness. Circulation Journal. 2010;74:2257.

[75] Intengan HD, Schiffrin EL. Structure and mechanical properties of resistance arteries in hypertension role of adhesion molecules and extracellular matrix determinants. Hypertension. 2000;36:312-8.

[76] Qiu H, Zhu Y, Sun Z, Trzeciakowski JP, Gansner M, Depre C, et al. Short Communication: Vascular Smooth Muscle Cell Stiffness As a Mechanism for Increased Aortic Stiffness With AgingNovelty and Significance. Circulation research. 2010;107:615-9.

[77] Alfonso F, Macaya C, Goicolea J, Hernandez R, Segovia J, Zamorano J, et al. Determinants of coronary compliance in patients with coronary artery disease: an intravascular ultrasound study. Journal of the American College of Cardiology. 1994;23:879-84.

[78] Wijnen J, Kuipers H, Kool M, Hoeks A, Van Baak M, HA SB, et al. Vessel wall properties of large arteries in trained and sedentary subjects. Basic research in cardiology. 1990;86:25-9.

[79] Lyon RT, Runyon-Hass A, Davis HR, Glagov S, Zarins CK. Protection from atherosclerotic lesion formation by reduction of artery wall motion. Journal of vascular surgery. 1987;5:59-67.

[80] Laurent S, Arcaro G, Benetos A, Lafleche A, Hoeks A, Safar M. Mechanism of nitrate-induced improvement on arterial compliance depends on vascular territory. Journal of cardiovascular pharmacology. 1992;19:641-9.

[81] Albinsson S, Nordström I, Hellstrand P. Stretch of the vascular wall induces smooth muscle differentiation by promoting actin polymerization. Journal of Biological Chemistry. 2004;279:34849-55.

[82] Na S, Trache A, Trzeciakowski J, Sun Z, Meininger G, Humphrey J. Time-dependent changes in smooth muscle cell stiffness and focal adhesion area in response to cyclic equibiaxial stretch. Annals of biomedical engineering. 2008;36:369-80.

[83] Borenstein JT, Terai H, King KR, Weinberg E, Kaazempur-Mofrad M, Vacanti J. Microfabrication technology for vascularized tissue engineering. Biomedical Microdevices. 2002;4:167-75.

[84] Park TH, Shuler ML. Integration of cell culture and microfabrication technology. Biotechnology Progress. 2003;19:243-53.

[85] Parker KK, Tan J, Chen CS, Tung L. Myofibrillar architecture in engineered cardiac myocytes. Circulation research. 2008;103:340-2.

[86] McCain ML, Sheehy SP, Grosberg A, Goss JA, Parker KK. Recapitulating maladaptive, multiscale remodeling of failing myocardium on a chip. Proceedings of the National Academy of Sciences. 2013;110:9770-5.

[87] Agarwal A, Farouz Y, Nesmith AP, Deravi LF, McCain ML, Parker KK. Micropatterning Alginate Substrates for In Vitro Cardiovascular Muscle on a Chip. Advanced Functional Materials. 2013.

[88] Kuo P-L, Lee H, Bray M-A, Geisse NA, Huang Y-T, Adams WJ, et al. Myocyte Shape Regulates Lateral Registry of Sarcomeres and Contractility. The American journal of pathology. 2012;181:2030-7.

[89] McCain ML, Lee H, Aratyn-Schaus Y, Kléber AG, Parker KK. Cooperative coupling of cell-matrix and cell–cell adhesions in cardiac muscle. Proceedings of the National Academy of Sciences. 2012;109:9881-6.

[90] Alford PW, Nesmith AP, Seywerd JN, Grosberg A, Parker KK. Vascular smooth muscle contractility depends on cell shape. Integrative Biology. 2011;3:1063-70.

[91] Ye GJC, Aratyn-Schaus Y, Nesmith AP, Pasqualini FS, Alford PW, Parker KK (2013) The contractile strength of vascular smooth muscle myocytes is shape dependent. Integrative Biology DOI: 10.1039/C3IB40230D

[92] Thakar RG, Ho F, Huang NF, Liepmann D, Li S. Regulation of vascular smooth muscle cells by micropatterning. Biochemical and Biophysical Research Communications. 2003;307:883-90.

[93] Thakar RG, Cheng Q, Patel S, Chu J, Nasir M, Liepmann D, et al. Cell-shape regulation of smooth muscle cell proliferation. Biophysical journal. 2009;96:3423-32.

[94] Goessl A, Bowen‐Pope DF, Hoffman AS. Control of shape and size of vascular smooth muscle cells in vitro by plasma lithography. Journal of biomedical materials research. 2001;57:15-24.

[95] Koltsova SV, Gusakova SV, Anfinogenova YJ, Baskakov MB, Orlov SN. Vascular smooth muscle contraction evoked by cell volume modulation: role of the cytoskeleton network. Cellular Physiology and Biochemistry. 2008;21:029-36.

[96] Hedin U, Thyberg J, Roy J, Dumitrescu A, Tran PK. Role of Tyrosine Kinases in Extracellular Matrix–Mediated Modulation of Arterial Smooth Muscle Cell Phenotype. Arteriosclerosis, thrombosis, and vascular biology. 1997;17:1977-84.

[97] Hayward I, Bridle K, Campbell G, Underwood P, Campbell J. Effect of extracellular matrix proteins on vascular smooth muscle cell phenotype. Cell biology international. 1995;19:727-34.

[98] Qin H, Ishiwata T, Wang R, Kudo M, Yokoyama M, Naito Z, et al. Effects of Extracellular Matrix on Phenotype Modulation and MAPK Transduction of Rat Aortic Smooth Muscle Cells< i> in Vitro</i>. Experimental and molecular pathology. 2000;69:79-90.

[99] Lim S-M, Kreipe BA, Trzeciakowski J, Dangott L, Trache A. Extracellular matrix effect on RhoA signaling modulation in vascular smooth muscle cells. Experimental cell research. 2010;316:2833-48.

[100] Niklason L, Gao J, Abbott W, Hirschi K, Houser S, Marini R, et al. Functional arteries grown in vitro. Science. 1999;284:489-93.

[101] Peyton SR, Putnam AJ. Extracellular matrix rigidity governs smooth muscle cell motility in a biphasic fashion. Journal of cellular physiology. 2005;204:198-209.

[102] Peyton SR, Kim PD, Ghajar CM, Seliktar D, Putnam AJ. The effects of matrix stiffness and RhoA on the phenotypic plasticity of smooth muscle cells in a 3-D biosynthetic hydrogel system. Biomaterials. 2008;29:2597-607.

[103] Dalby MJ, Gadegaard N, Riehle MO, Wilkinson CD, Curtis AS. Investigating filopodia sensing using arrays of defined nano-pits down to 35 nm diameter in size. The international journal of biochemistry & cell biology. 2004;36:2005-15.

[104] Dalby MJ, Riehle MO, Yarwood SJ, Wilkinson CD, Curtis AS. Nucleus alignment and cell signaling in fibroblasts: response to a micro-grooved topography. Experimental cell research. 2003;284:272-80.

[105] Corey JM, Feldman EL. Substrate patterning: an emerging technology for the study of neuronal behavior. Experimental neurology. 2003;184:89-96.

[106] Wójciak-Stothard B, Curtis A, Monaghan W, Macdonald K, Wilkinson C. Guidance and activation of murine macrophages by nanometric scale topography. Experimental cell research. 1996;223:426-35.

[107] Dalby M, Riehle M, Johnstone H, Affrossman S, Curtis A. In vitro reaction of endothelial cells to polymer demixed nanotopography. Biomaterials. 2002;23:2945-54.

[108] Abrams G, Goodman S, Nealey P, Franco M, Murphy C. Nanoscale topography of the basement membrane underlying the corneal epithelium of the rhesus macaque. Cell and tissue research. 2000;299:39-46.

[109] Yim EK, Reano RM, Pang SW, Yee AF, Chen CS, Leong KW. Nanopattern-induced changes in morphology and motility of smooth muscle cells. Biomaterials. 2005;26:5405-13.

[110] Glawe JD, Hill JB, Mills DK, McShane MJ. Influence of channel width on alignment of smooth muscle cells by high‐aspect‐ratio microfabricated elastomeric cell culture scaffolds. Journal of Biomedical Materials Research Part A. 2005;75:106-14.

[111] Taneja V, Vertegel A, Langan III EM, LaBerge M. Influence of Topography of an Endovascular Stent Material on Smooth Muscle Cell Response. Annals of Vascular Surgery. 2011;25:675-85.

[112] Barth AI, Näthke IS, Nelson WJ. Cadherins, catenins and APC protein: interplay between cytoskeletal complexes and signaling pathways. Current opinion in cell biology. 1997;9:683-90.

[113] Hao H, Ropraz P, Verin V, Camenzind E, Geinoz A, Pepper MS, et al. Heterogeneity of smooth muscle cell populations cultured from pig coronary artery. Arteriosclerosis, thrombosis, and vascular biology. 2002;22:1093-9.

[114] Chen CS, Alonso JL, Ostuni E, Whitesides GM, Ingber DE. Cell shape provides global control of focal adhesion assembly. Biochemical and biophysical research communications. 2003;307:355-61.

[115] Parker KK, Brock AL, Brangwynne C, Mannix RJ, Wang N, Ostuni E, et al. Directional control of lamellipodia extension by constraining cell shape and orienting cell tractional forces. The FASEB Journal. 2002;16:1195-204.

[116] Schwartz MA. Integrins and extracellular matrix in mechanotransduction. Cold Spring Harbor perspectives in biology. 2010;2.

[117] Li C, Xu Q. Mechanical stress-initiated signal transduction in vascular smooth muscle cells *in vitro* and *in vivo*. Cellular signalling. 2007;19:881-91.

[118] Maniotis AJ, Chen CS, Ingber DE. Demonstration of mechanical connections between integrins, cytoskeletal filaments, and nucleoplasm that stabilize nuclear structure. Proceedings of the National Academy of Sciences. 1997;94:849-54.

[119] Bagby R. Organization of contractile/cytoskeletal elements. Biochemistry of smooth muscle. 1983;1:1-84.

[120] Versaevel M, Grevesse T, Gabriele S. Spatial coordination between cell and nuclear shape within micropatterned endothelial cells. Nature communications. 2012;3:671.

[121] DiMilla PA, Stone JA, Quinn JA, Albelda SM, Lauffenburger DA. Maximal migration of human smooth muscle cells on fibronectin and type IV collagen occurs at an intermediate attachment strength. The Journal of cell biology. 1993;122:729-37.

[122] Li S, Sims S, Jiao Y, Chow LH, Pickering JG. Evidence from a novel human cell clone that adult vascular smooth muscle cells can convert reversibly between noncontractile and contractile phenotypes. Circulation research. 1999;85:338-48.

[123] Wang Z, Newman WH. Smooth muscle cell migration stimulated by interleukin 6 is associated with cytoskeletal reorganization. Journal of Surgical Research. 2003;111:261-6.

[124] Jiang Q, Huang R, Cai S, Wang C-LA. Caldesmon regulates the motility of vascular smooth muscle cells by modulating the actin cytoskeleton stability. Journal of biomedical science. 2010;17:6.

[125] Wede OK, Löfgren M, Li Z, Paulin D, Arner A. Mechanical function of intermediate filaments in arteries of different size examined using desmin deficient mice. The Journal of physiology. 2002;540:941-9.

[126] Sjuve R, Arner A, Li Z, Mies B, Paulin D, Schmittner M, et al. Mechanical alterations in smooth muscle from mice lacking desmin. Journal of Muscle Research & Cell Motility. 1998;19:415-29.

[127] Shaw L, Ahmed S, Austin C, Taggart MJ. Inhibitors of actin filament polymerisation attenuate force but not global intracellular calcium in isolated pressurised resistance arteries. Journal of vascular research. 2003;40:1-10.

[128] Worth NF, Rolfe BE, Song J, Campbell GR. Vascular smooth muscle cell phenotypic modulation in culture is associated with reorganisation of contractile and cytoskeletal proteins. Cell motility and the cytoskeleton. 2001;49:130-45.

[129] Mack CP, Somlyo AV, Hautmann M, Somlyo AP, Owens GK. Smooth muscle differentiation marker gene expression is regulated by RhoA-mediated actin polymerization. Journal of Biological Chemistry. 2001;276:341-7.

[130] Zeidan A, Nordström I, Albinsson S, Malmqvist U, Swärd K, Hellstrand P. Stretch-induced contractile differentiation of vascular smooth muscle: sensitivity to actin polymerization inhibitors. American Journal of Physiology-Cell Physiology. 2003;284:C1387-C96.

[131] Rhodin JA. Architecture of the vessel wall. Comprehensive Physiology. 2011.

[132] Dillon PF, Aksoy MO, Driska SP, Murphy RA. Myosin phosphorylation and the cross-bridge cycle in arterial smooth muscle. Science. 1981;211:495-7.

[133] Bohr DF, Webb R. Vascular smooth muscle function and its changes in hypertension. The American journal of medicine. 1984;77:3.

[134] Davies PF. Flow-mediated endothelial mechanotransduction. Physiological reviews. 1995;75:519.

[135] Tarbell JM, Weinbaum S, Kamm RD. Cellular fluid mechanics and mechanotransduction. Annals of biomedical engineering. 2005;33:1719-23.

[136] Davis MJ, Hill MA. Signaling mechanisms underlying the vascular myogenic response. Physiological Reviews. 1999;79:387-423.

[137] Domenga V, Fardoux P, Lacombe P, Monet M, Maciazek J, Krebs LT, et al. Notch3 is required for arterial identity and maturation of vascular smooth muscle cells. Genes & development. 2004;18:2730-5.

[138] Ruchoux MM, Guerouaou D, Vandenhaute B, Pruvo J-P, Vermersch P, Leys D. Systemic vascular smooth muscle cell impairment in cerebral autosomal dominant arteriopathy with subcortical infarcts and leukoencephalopathy. Acta neuropathologica. 1995;89:500-12.

[139] Rensen S, Doevendans P, Van Eys G. Regulation and characteristics of vascular smooth muscle cell phenotypic diversity. Netherlands Heart Journal. 2007;15:100-8.

[140] Crouch EC, Stenmark KR, Voelkel NF. Smooth muscle-mediated connective tissue remodeling in pulmonary hypertension. Am J Med Genet. 1986;23:445.

[141] Libby P, Tanaka H. The molecular bases of restenosis. Progress in cardiovascular diseases. 1997;40:97-106.

[142] Orekhov A, Karpova I, Tertov V, Rudchenko S, Andreeva E, Krushinsky A, et al. Cellular composition of atherosclerotic and uninvolved human aortic subendothelial intima. Light-microscopic study of dissociated aortic cells. The American journal of pathology. 1984;115:17.

[143] Orekhov A, Andreeva E, Krushinsky A, Novikov I, Tertov V, Nestaiko G, et al. Intimal cells and atherosclerosis. Relationship between the number of intimal cells and major manifestations of atherosclerosis in the human aorta. The American journal of pathology. 1986;125:402.

[144] Orekhov AN, Krushinsky AV, Andreeva ER, Repin VS, Smirnov VN. Adult human aortic cells in primary culture: heterogeneity in shape. Heart and vessels. 1986;2:193-201.

[145] Bonin LR, Madden K, Shera K, Ihle J, Matthews C, Aziz S, et al. Generation and characterization of human smooth muscle cell lines derived from atherosclerotic plaque. Arteriosclerosis, thrombosis, and vascular biology. 1999;19:575-87.

[146] Martínez‑González J, Berrozpe M, Varela O, Badimon L. Heterogeneity of smooth muscle cells in advanced human atherosclerotic plaques: intimal smooth muscle cells expressing a fibroblast surface protein are highly activated by platelet‑released products. European journal of clinical investigation. 2001;31:939-49.

[147] Konishi I, Fujii S, Okamura H, Mori T. Development of smooth muscle in the human fetal uterus: an ultrastructural study. Journal of anatomy. 1984;139:239.

[148] Kurman RJ, Norris HJ. Mesenchymal tumors of the uterus VI. Epithelioid smooth muscle tumors including leiomyoblastoma and clear‑cell leiomyoma. A clinical and pathologic analysis of 26 cases. Cancer. 1976;37:1853-65.

[149] Manasek FJ, Burnside MB, Waterman RE. Myocardial cell shape change as a mechanism of embryonic heart looping. Developmental biology. 1972;29:349-71.

[150] Alford PW, Taber LA. Computational study of growth and remodelling in the aortic arch. Computer methods in biomechanics and biomedical engineering. 2008;11:525-38.

[151] Gerdes AM. Cardiac myocyte remodeling in hypertrophy and progression to failure. Journal of cardiac failure. 2002;8:S264-S8.

[152] Gerdes AM, Capasso JM. Structural remodeling and mechanical dysfunction of cardiac myocytes in heart failure. Journal of molecular and cellular cardiology. 1995;27:849-56.

[153] Gerdes AM, Kellerman SE, Moore JA, Muffly KE, Clark LC, Reaves PY, et al. Structural remodeling of cardiac myocytes in patients with ischemic cardiomyopathy. Circulation. 1992;86:426-30.

[154] McCrossan ZA, Billeter R, White E. Transmural changes in size, contractile and electrical properties of SHR left ventricular myocytes during compensated hypertrophy. Cardiovascular research. 2004;63:283-92.

[155] Sawada K-i, Kawamura K. Architecture of myocardial cells in human cardiac ventricles with concentric and eccentric hypertrophy as demonstrated by quantitative scanning electron microscopy. Heart and vessels. 1991;6:129-42.

[156] Feinberg AW, Alford PW, Jin H, Ripplinger CM, Werdich AA, Sheehy SP, et al. Controlling the contractile strength of engineered cardiac muscle by hierarchal tissue architecture. Biomaterials. 2012;33:5732-41.

[157] Grosberg A, Kuo P-L, Guo C-L, Geisse NA, Bray M-A, Adams WJ, et al. Self-organization of muscle cell structure and function. PLoS computational biology. 2011;7:e1001088.

[158] Chen CS, Mrksich M, Huang S, Whitesides GM, Ingber DE. Geometric control of cell life and death. Science. 1997;276:1425-8.

[159] Nelson CM, Jean RP, Tan JL, Liu WF, Sniadecki NJ, Spector AA, et al. From the Cover: Emergent patterns of growth controlled by multicellular form and mechanics. Science Signaling. 2005;102:11594.

[160] Bray MA, Sheehy SP, Parker KK. Sarcomere alignment is regulated by myocyte shape. Cell motility and the cytoskeleton. 2008;65:641-51.

[161] Sarkar S, Dadhania M, Rourke P, Desai TA, Wong JY. Vascular tissue engineering: microtextured scaffold templates to control organization of vascular smooth muscle cells and extracellular matrix. Acta Biomaterialia. 2005;1:93-100.

[162] Tolić-Nørrelykke IM, Wang N. Traction in smooth muscle cells varies with cell spreading. Journal of biomechanics. 2005;38:1405-12.

[163] Discher DE, Janmey P, Wang Y-l. Tissue cells feel and respond to the stiffness of their substrate. Science. 2005;310:1139-43.

[164] Yeung T, Georges PC, Flanagan LA, Marg B, Ortiz M, Funaki M, et al. Effects of substrate stiffness on cell morphology, cytoskeletal structure, and adhesion. Cell motility and the cytoskeleton. 2005;60:24-34.

[165] Engler AJ, Carag-Krieger C, Johnson CP, Raab M, Tang H-Y, Speicher DW, et al. Embryonic cardiomyocytes beat best on a matrix with heart-like elasticity: scar-like rigidity inhibits beating. Journal of cell science. 2008;121:3794-802.

[166] Tolic-Norrelykke IM, Wang N. Traction in smooth muscle cells varies with cell spreading. Journal of Biomechanics. 2005;38:1405-12.

[167] Shen JY, Chan-Park MB, Zhu AP, Zhu X, Beuerman RW, Yang EB, et al. Three-dimensional microchannels in biodegradable polymeric films for control orientation and phenotype of vascular smooth muscle cells. Tissue Engineering. 2006;12:2229-40.

[168] Zhu AP, Zhao F, Fang N. Regulation of vascular smooth muscle cells on poly(ethylene terephthalate) film by O-carboxymethylchitosan surface immobilization. Journal of Biomedical Materials Research Part A. 2008;86A:467-76.

[169] Rezakhaniha R, Agianniotis A, Schrauwen JTC, Griffa A, Sage D, Bouten C, et al. Experimental investigation of collagen waviness and orientation in the arterial adventitia using confocal laser scanning microscopy. Biomechanics and modeling in mechanobiology. 2012;11:461-73.

[170] Volfson D, Cookson S, Hasty J, Tsimring LS. Biomechanical ordering of dense cell populations. Proceedings of the National Academy of Sciences. 2008;105:15346-51.

[171] Sims JR, Karp S, Ingber DE. Altering the cellular mechanical force balance results in integrated changes in cell, cytoskeletal and nuclear shape. Journal of Cell Science. 1992;103:1215-22.

[172] Dahl KN, Ribeiro AJ, Lammerding J. Nuclear shape, mechanics, and mechanotransduction. Circulation research. 2008;102:1307-18.

[173] Sherwood L. Human physiology: from cells to systems: Thomson Brooks/Cole; 2012.
[174] Butler JP, Tolić-Nørrelykke IM, Fabry B, Fredberg JJ. Traction fields, moments, and strain energy that cells exert on their surroundings. American Journal of Physiology-Cell Physiology. 2002;282:C595-C605.

[175] Wang N, Tolić-Nørrelykke IM, Chen J, Mijailovich SM, Butler JP, Fredberg JJ, et al. Cell prestress. I. Stiffness and prestress are closely associated in adherent contractile cells. American Journal of Physiology-Cell Physiology. 2002;282:C606-C16.

[176] Omelchenko T, Vasiliev J, Gelfand I, Feder H, Bonder E. Mechanisms of polarization of the shape of fibroblasts and epitheliocytes: Separation of the roles of microtubules and Rho-dependent actin–myosin contractility. Proceedings of the National Academy of Sciences. 2002;99:10452-7.

[177] Webb RC. Smooth muscle contraction and relaxation. Advances in physiology education. 2003;27:201-6.

[178] Bray M-AP, Adams WJ, Geisse NA, Feinberg AW, Sheehy SP, Parker KK. Nuclear morphology and deformation in engineered cardiac myocytes and tissues. Biomaterials. 2010;31:5143-50.

[179] Seifu DG, Purnama A, Mequanint K, Mantovani D. Small-diameter vascular tissue engineering. Nature Reviews Cardiology. 2013.

[180] Naito Y, Shinoka T, Duncan D, Hibino N, Solomon D, Cleary M, et al. Vascular tissue engineering: towards the next generation vascular grafts. Advanced drug delivery reviews. 2011;63:312-23.

[181] Kumar VA, Brewster LP, Caves JM, Chaikof EL. Tissue engineering of blood vessels: functional requirements, progress, and future challenges. Cardiovascular engineering and technology. 2011;2:137-48.

[182] Peck M, Gebhart D, Dusserre N, McAllister TN, L'Heureux N. The evolution of vascular tissue engineering and current state of the art. Cells Tissues Organs. 2011;195:144-58.

[183] Kannan RY, Salacinski HJ, Butler PE, Hamilton G, Seifalian AM. Current status of prosthetic bypass grafts: a review. Journal of Biomedical Materials Research Part B: Applied Biomaterials. 2005;74:570-81.

[184] E McBane J, Sharifpoor S, S Labow R, Ruel M, J Suuronen E, Paul Santerre J. Tissue engineering a small diameter vessel substitute: engineering constructs with select biomaterials and cells. Current Vascular Pharmacology. 2012;10:347-60.

[185] McDaniel DP, Shaw GA, Elliott JT, Bhadriraju K, Meuse C, Chung K-H, et al. The stiffness of collagen fibrils influences vascular smooth muscle cell phenotype. Biophysical journal. 2007;92:1759-69.

[186] Christen T, Bochaton-Piallat M-L, Neuville P, Rensen S, Redard M, Van Eys G, et al. Cultured Porcine Coronary Artery Smooth Muscle Cells A New Model With Advanced Differentiation. Circulation research. 1999;85:99-107.

[187] Frid MG, Moiseeva EP, Stenmark KR. Multiple phenotypically distinct smooth muscle cell populations exist in the adult and developing bovine pulmonary arterial media in vivo. Circulation research. 1994;75:669-81.

[188] Alford PW, Dabiri BE, Goss JA, Hemphill MA, Brigham MD, Parker KK. Blast-induced phenotypic switching in cerebral vasospasm. Proceedings of the National Academy of Sciences. 2011;108:12705-10.

[189] Böl M, Reese S, Parker KK, Kuhl E. Computational modeling of muscular thin films for cardiac repair. Computational Mechanics. 2009;43:535-44.

[190] Alford PW, Feinberg AW, Sheehy SP, Parker KK. Biohybrid thin films for measuring contractility in engineered cardiovascular muscle. Biomaterials. 2010;31:3613-21.

[191] Feinberg AW, Feigel A, Shevkoplyas SS, Sheehy S, Whitesides GM, Parker KK. Muscular thin films for building actuators and powering devices. Science. 2007;317:1366-70.

[192] Uglow EB, Slater S, Sala-Newby GB, Aguilera-Garcia CM, Angelini GD, Newby AC, et al. Dismantling of cadherin-mediated cell-cell contacts modulates smooth muscle cell proliferation. Circulation research. 2003;92:1314-21.

[193] Brown XQ, Bartolak‐Suki E, Williams C, Walker ML, Weaver VM, Wong JY. Effect of substrate stiffness and PDGF on the behavior of vascular smooth muscle cells: implications for atherosclerosis. Journal of cellular physiology. 2010;225:115-22.

[194] Koutsouki E, Aguilera-Garcia C, Sala-Newby G, Newby A, George S. Cell-cell contact by cadherins provides an essential survival signal to migrating smooth muscle cells. Eur Heart J. 2003;24:1838.

[195] Isenberg BC, DiMilla PA, Walker M, Kim S, Wong JY. Vascular smooth muscle cell durotaxis depends on substrate stiffness gradient strength. Biophysical journal. 2009;97:1313-22.

[196] Humphries JD, Wang P, Streuli C, Geiger B, Humphries MJ, Ballestrem C. Vinculin controls focal adhesion formation by direct interactions with talin and actin. The Journal of cell biology. 2007;179:1043-57.

[197] Kuo K-H, Herrera AM, Wang L, Paré PD, Ford LE, Stephens NL, et al. Structure-function correlation in airway smooth muscle adapted to different lengths. American Journal of Physiology-Cell Physiology. 2003;285:C384-C90.

[198] Seow CY, Pratusevich VR, Ford LE. Series-to-parallel transition in the filament lattice of airway smooth muscle. Journal of Applied Physiology. 2000;89:869-76.

[199] Gunst SJ, Meiss RA, Wu M-F, Rowe M. Mechanisms for the mechanical plasticity of tracheal smooth muscle. American Journal of Physiology-Cell Physiology. 1995;268:C1267-C76.

[200] Lambert RK, Pare PD, Seow CY. Mathematical description of geometric and kinematic aspects of smooth muscle plasticity and some related morphometrics. Journal of Applied Physiology. 2004;96:469-76.

[201] Solway J, Bellam S, Dowell M, Camoretti-Mercado B, Dulin N, Fernandes D, et al. Actin DynamicsA Potential Integrator of Smooth Muscle (Dys-) Function and Contractile Apparatus Gene Expression In Asthma. CHEST Journal. 2003;123:392S-8S.

[202] Liu WF. Mechanical regulation of cellular phenotype: implications for vascular tissue regeneration. Cardiovascular research. 2012;95:215-22.

[203] Thomas CH, Collier JH, Sfeir CS, Healy KE. Engineering gene expression and protein synthesis by modulation of nuclear shape. Proceedings of the National Academy of Sciences. 2002;99:1972-7.

[204] Lelièvre SA, Weaver VM, Nickerson JA, Larabell CA, Bhaumik A, Petersen OW, et al. Tissue phenotype depends on reciprocal interactions between the extracellular matrix and the structural organization of the nucleus. Proceedings of the National Academy of Sciences. 1998;95:14711-6.

[205] Guilak F. Compression-induced changes in the shape and volume of the chondrocyte nucleus. Journal of biomechanics. 1995;28:1529-41.

[206] Zink D, Fischer AH, Nickerson JA. Nuclear structure in cancer cells. Nature reviews cancer. 2004;4:677-87.

[207] Capell BC, Collins FS. Human laminopathies: nuclei gone genetically awry. Nature Reviews Genetics. 2006;7:940-52.

[208] Webster M, Witkin KL, Cohen-Fix O. Sizing up the nucleus: nuclear shape, size and nuclear-envelope assembly. Journal of cell science. 2009;122:1477-86.

[209] Chow K-H, Factor RE, Ullman KS. The nuclear envelope environment and its cancer connections. Nature Reviews Cancer. 2012;12:196-209.

[210] Conte MS. The ideal small arterial substitute: a search for the Holy Grail? The FASEB journal. 1998;12:43-5.

[211] Kato S, Shanley JR, Fox JC. Serum stimulation, cell-cell interactions, and extracellular matrix independently influence smooth muscle cell phenotype in vitro. The American journal of pathology. 1996;149:687.

[212] Hoebe R, Van Oven C, Gadella TW, Dhonukshe P, Van Noorden C, Manders E. Controlled light-exposure microscopy reduces photobleaching and phototoxicity in fluorescence live-cell imaging. Nature biotechnology. 2007;25:249-53.

[213] Langer R, Vacanti JP. Tissue engineering. Science. 1993;260:920-6.

[214] Bhatia SN, Chen CS. Tissue engineering at the micro-scale. Biomedical Microdevices. 1999;2:131-44.

[215] Mironov V, Visconti RP, Kasyanov V, Forgacs G, Drake CJ, Markwald RR. Organ printing: Tissue spheroids as building blocks. Biomaterials. 2009;30:2164-74.

[216] Boland T, Mironov V, Gutowska A, Roth EA, Markwald RR. Cell and organ printing 2: Fusion of cell aggregates in three-dimensional gels. Anatomical Record Part a-Discoveries in Molecular Cellular and Evolutionary Biology. 2003;272A:497-502.

[217] Tsuda Y, Shimizu T, Yarnato M, Kikuchi A, Sasagawa T, Sekiya S, et al. Cellular control of tissue architectures using a three-dimensional tissue fabrication technique. Biomaterials. 2007;28:4939-46.

[218] Shimizu T, Yamato M, Kikuchi A, Okano T. Cell sheet engineering for myocardial tissue reconstruction. Biomaterials. 2003;24:2309-16.

[219] Nahmias Y, Schwartz RE, Verfaillie CM, Odde DJ. Laser-guided direct writing for three-dimensional tissue engineering. Biotechnology and Bioengineering. 2005;92:129-36.

[220] Fujii T. Method for solubilizing insoluble collagen fibers. Google Patents; 1967.
[221] Levenberg S, Huang NF, Lavik E, Rogers AB, Itskovitz-Eldor J, Langer R. Differentiation of human embryonic stem cells on three-dimensional polymer scaffolds. Proceedings of the National Academy of Sciences. 2003;100:12741-6.

146

[222] Gerhardt H, Betsholtz C. Endothelial-pericyte interactions in angiogenesis. Cell and tissue research. 2003;314:15-23.

[223] Armulik A, Abramsson A, Betsholtz C. Endothelial/pericyte interactions. Circulation research. 2005;97:512-23.

[224] Carmeliet P. Mechanisms of angiogenesis and arteriogenesis. Nature medicine. 2000;6:389-95.

[225] Albrecht DR, Underhill GH, Wassermann TB, Sah RL, Bhatia SN. Probing the role of multicellular organization in three-dimensional microenvironments. Nature methods. 2006;3:369-75.

[226] Nahmias Y, Schwartz RE, Verfaillie CM, Odde DJ. Laser‐guided direct writing for three‐dimensional tissue engineering. Biotechnology and bioengineering. 2005;92:129-36.

[227] Derda R, Laromaine A, Mammoto A, Tang SK, Mammoto T, Ingber DE, et al. Paper-supported 3D cell culture for tissue-based bioassays. Proceedings of the National Academy of Sciences. 2009;106:18457-62.

[228] Carmeliet P, Jain RK. Angiogenesis in cancer and other diseases. Nature. 2000;407:249-57.

[229] Levenberg S, Rouwkema J, Macdonald M, Garfein ES, Kohane DS, Darland DC, et al. Engineering vascularized skeletal muscle tissue. Nature biotechnology. 2005;23:879-84.

[230] Kaufman-Francis K, Koffler J, Weinberg N, Dor Y, Levenberg S. Engineered vascular beds provide key signals to pancreatic hormone-producing cells. PloS one. 2012;7:e40741.

[231] Melero-Martin JM, De Obaldia ME, Kang S-Y, Khan ZA, Yuan L, Oettgen P, et al. Engineering robust and functional vascular networks in vivo with human adult and cord blood–derived progenitor cells. Circulation research. 2008;103:194-202.

[232] Yang J, Motlagh D, Webb AR, Ameer GA. Novel biphasic elastomeric scaffold for small-diameter blood vessel tissue engineering. Tissue engineering. 2005;11:1876-86.

[233] Nawroth JC, Lee H, Feinberg AW, Ripplinger CM, McCain ML, Grosberg A, et al. A tissue-engineered jellyfish with biomimetic propulsion. Nature biotechnology. 2012;30:792-7.

6   Appendices

6.1   Appendix A: List of Publications

1. Ye GJC, Aratyn-Schaus Y, Nesmith, AP, Pasqualini FS, Alford PW, Parker KK.
    The contractile strength of vascular smooth muscle myocytes is shape
    dependent. *Integrative Biology.* DOI: 10.1039/C3IB40230D

6.2   Appendix B: MATLAB code for analyzing cellular forces in traction force microscopy studies

```matlab
function DBG_force_calculation(pathname)

cd(pathname);


imgfile = ('Full_stack_aligned.tif');

tif_info = imfinfo(imgfile);

tif_size = size(tif_info,1);

file_name = ['Full_stack_aligned_ROI_1_1_512_512_1_' num2str(tif_size)
'_Mat.mat'];

load (file_name);

load ('ROI_1_1_512_512_Cell_boundary.mat');

frame_count = length(TFM_results);


I = imread('Cell.tif');

c = xrub;

r = yrub;

BW = roipoly(I,c,r);

scaled_mask=imresize(BW,1/16,'nearest');

sum_force = zeros(10,2);

for frame_number = 1:frame_count


%for the first frame, get the principle and normal axis of the cell
```

```matlab
    if frame_number == 1

    figure, imshow('Cell.tif');

    h = imline;

    position = wait(h);

    principle_axis = [position(2,1)-position(1,1), position(2,2)-position(1,2)];

    % get unit vector

    principle_axis = principle_axis / norm(principle_axis);

    normal_axis = [-(position(2,2)-position(1,2)), position(2,1)-position(1,1)];

    normal_axis = normal_axis / norm(normal_axis);

    close all

    end



    %getting the principle axis traction force

    tract_parallel = zeros(length(TFM_results(1,1).traction(:,:)),1);

    for i = 1:length(TFM_results(1,frame_number).traction(:,:))

        tract_parallel(i) =
abs(dot(principle_axis,TFM_results(1,frame_number).traction(i,:)));

    end



    %convert to a 32 x 32 grid

    tract_parallel_array = zeros(32);

    count = 1;
```

```matlab
    for i = 1:32

        for k = 1:32

            tract_parallel_array(k,i) = tract_parallel(count);

            count=count+1;

        end

    end


    tract_parallel_array_mask = tract_parallel_array.*scaled_mask;

    sum_force_principle = sum(sum(tract_parallel_array_mask));


    %getting the perpendicular axis traction force

    tract_perpendicular = zeros(length(TFM_results(1,1).traction(:,:)),1);

    for i = 1:length(TFM_results(1,frame_number).traction(:,:))

        tract_perpendicular(i) =

abs(dot(normal_axis,TFM_results(1,frame_number).traction(i,:)));

    end


    %convert to a 32 x 32 grid

    tract_perpendicular_array = zeros(32);

    count = 1;

    for i = 1:32

        for k = 1:32

            tract_perpendicular_array(k,i) = tract_perpendicular(count);
```

```matlab
        count=count+1;

    end

end


tract_perpendicular_array_mask = tract_perpendicular_array.*scaled_mask;

sum_force_perpendicular = sum(sum(tract_perpendicular_array_mask));


%convert from Pa to uN by multiplying 100um^2 lattice area and then divide

%by 2 since two ends

sum_force(frame_number,:) = [sum_force_principle
sum_force_perpendicular]/10000/2;

end

%save the file

[nrows,ncols]= size(sum_force);

filename = 'sum_force.txt';

fid = fopen(filename, 'w');

for row=1:nrows

    fprintf(fid, '%6.4f %6.4f\r\n', sum_force(row,:));

end

fclose(fid);

load sum_force.txt;

xlswrite('sum_force.xls', sum_force);
```

```matlab
function [initial, ET_1, HA, ref] = DBG_calculate_average_X(pathname)

cd(pathname);


imgfile = ('Full_stack_aligned.tif');

tif_info = imfinfo(imgfile);

tif_size = size(tif_info,1);


num = xlsread('sum_force.xls');


if (tif_size < 11)

    initial = 0;

    ET_1 = 0;

    HA = 0;

    ref = 0;

else

    initial = mean(num(1:3,1));

    ET_1 = mean(num(4:6,1));

    HA = mean(num(7:9,1));

    ref = num(10,1);

end

end


function [initial, ET_1, HA, ref] = DBG_calculate_average_Y(pathname)
```

```matlab
cd(pathname);

imgfile = ('Full_stack_aligned.tif');

tif_info = imfinfo(imgfile);

tif_size = size(tif_info,1);

num = xlsread('sum_force.xls');

if (tif_size < 11)

    initial = 0;

    ET_1 = 0;

    HA = 0;

    ref = 0;

else

    initial = mean(num(1:3,2));

    ET_1 = mean(num(4:6,2));

    HA = mean(num(7:9,2));

    ref = num(10,2);

end

end
```